

NASA CONTRACTOR
REPORT



NASA CR-1396

NASA CR-1396

CASE FILE
COPY

DESIGN OF STRAPDOWN GYROSCOPES FOR A DYNAMIC ENVIRONMENT

Interim Scientific Report II

by Arthur A. Sutherland, Jr., and William S. Beebe

Prepared by
THE ANALYTIC SCIENCES CORPORATION
Reading, Mass.
for Electronics Research Center

NATIONAL AERONAUTICS AND SPACE ADMINISTRATION • WASHINGTON, D. C. • AUGUST 1969

DESIGN OF STRAPDOWN GYROSCOPES FOR
A DYNAMIC ENVIRONMENT

Interim Scientific Report II

By Arthur A. Sutherland, Jr., and William S. Beebee

Distribution of this report is provided in the interest of information exchange. Responsibility for the contents resides in the author or organization that prepared it.

Issued by Originator as Report No. TR-101-4

Prepared under Contract No. NAS 12-508 by
THE ANALYTIC SCIENCES CORPORATION
Reading, Mass.

for Electronics Research Center

NATIONAL AERONAUTICS AND SPACE ADMINISTRATION

For sale by the Clearinghouse for Federal Scientific and Technical Information
Springfield, Virginia 22151 - CFSTI price \$3.00

**Dr. Herbert Weinstock
Technical Monitor
NAS 12-508
Electronics Research Center
575 Technology Square
Cambridge, Massachusetts 02139**

ABSTRACT

This report is addressed to some aspects of the analysis of vibration-induced attitude errors in strapdown inertial navigators. Three common pulse torquing techniques for strapdown gyros are described. The important considerations in choosing a rebalance scheme are reviewed and relative advantages of the three approaches are discussed. Binary and ternary pulse rebalanced gyros are analyzed using describing functions. Closed loop sinusoidal transfer characteristics are obtained analytically and compared with the results of detailed gyro simulations. The effects of compliance between the gyro wheel and gimbal are also illustrated by analysis and simulation.

Compensation of limit cycling binary torqued gyros is treated with the goal of providing a better closed loop response. A discussion of the dithered binary gyro is presented, illustrating limit cycle determination and closed loop characteristics. A brief discussion of plans for a comprehensive gyro and system error simulation is provided. The appendices provide details in support of the report body and also treat diverse subjects such as dynamic errors in single-degree-of-freedom pendulous accelerometers, gyro misalignment caused by angular rates about the output axis and the recovery of angular rate information from pulse torqued gyros. The research discussed in this report includes work presented in TASC report TR-101-3 and constitutes an extension of that effort.

TABLE OF CONTENTS

	<u>Page No.</u>
ABSTRACT	v
List of Figures	xi
1. INTRODUCTION	1
1.1 Vibration-Induced Attitude Errors in Strapdown Inertial Systems	1
1.2 Summary	2
2. DESCRIPTION OF PULSE TORQUING SCHEMES	5
Summary	5
2.1 Pulse Rebalanced Gyros	5
2.2 Aspects of Pulse Torquing Gyro Errors	15
2.3 Comparison of Pulse Torquing Techniques	20
3. STRAPDOWN SYSTEM ATTITUDE ERRORS ARISING FROM VIBRATIONAL MOTION	25
Summary	25
3.1 Description of Gyro and Vibration Characteristics	25
3.2 Drift Rate Contributions	28
3.2.1 Spin-Input Crosscoupling	28
3.2.2 Spin-Output Crosscoupling	29
3.2.3 Anisoinertia	30
3.2.4 Torquer Scale Factor Asymmetry	31
3.2.5 Pseudo-Coning	32
3.2.6 Undetected System Coning Motion	32
3.2.7 Linear Vibration Errors	33
3.3 System Drift Rate	33

TABLE OF CONTENTS (Continued)

	<u>Page No.</u>
4. BINARY PULSE REBALANCED GYRO	37
Summary	37
4.1 Analysis of the Limit Cycling Binary Gyro	41
4.1.1 Simple Gyro Dynamics	41
4.1.2 Gyro Dynamics with Rotor Bearing Compliance	46
4.2 Simulation of the Limit Cycling Binary Gyro	52
4.2.1 Simple Gyro Dynamics	52
4.2.2 Gyro Dynamics with Rotor Bearing Compliance	60
4.3 Compensation for the Limit Cycling Binary Gyro	62
4.4 Linear Analysis of the Dithered Binary Gyro	71
5. TERNARY PULSE REBALANCED GYRO	77
Summary	77
5.1 Analysis of the Frequency Response Characteristics of the Ternary Gyro	79
5.2 Simulation of the Ternary Gyro	88
5.2.1 Simple Gyro Dynamics	88
5.2.2 Gyro Dynamics with Rotor-to-Gimbal Compliance	93
5.3 Effect of Random Signal at the Nonlinearity Input	95
6. GYRO AND SYSTEM ERROR SIMULATION	101
Summary	101
6.1 Motivation for a Simulation	101
6.2 Program for the Digital Portion	105
7. CONCLUSION	109
7.1 Conclusions	109
7.2 Continuation of Effort	111

TABLE OF CONTENTS (Continued)

	<u>Page No.</u>
APPENDICES	
Appendix A Gimbal Misalignments Caused by Output Axis Angular Motion	113
Appendix B Motion Induced Errors in the Single-Degree- of-Freedom Pendulous Accelerometer	121
Appendix C Accuracy of the Small Signal Approximation to the Two-Sinusoid-Input Describing Function for the Binary Nonlinearity	127
Appendix D Limit Cycle Quenching in the Binary Gyro Loop	131
Appendix E Derivation of the Ellipses Used in Determining the Frequency Response of the Ternary Gyro Loop	139
Appendix F Simulation of Gyros with a Simple Representation of Dynamics	143
Appendix G Simulation of Gyros with Rotor-to-Gimbal Compliance	149
Appendix H The Fourier Analyzer	155
Appendix I Derivation of Transfer Functions Representing Rotor-to-Gimbal Compliance Effects	161
Appendix J Recovering Angular Rate Information from the Outputs of Pulse Torqued Gyros	167
REFERENCES	175

LIST OF FIGURES

<u>Figure No.</u>		<u>Page No.</u>
2.1-1	Single-Degree-of-Freedom Gyro	6
2.1-2	Rebalanced Gyro Schematic	8
2.1-3	Two Level Logic	10
2.1-4	Representative Torque Output from Delta Modulated Pulse Rebalance Technique	10
2.1-5	Three Level Logic	11
2.1-6	Time Modulated Torquing	12
2.1-7	Torque Waveform for Time Modulated Torquing	13
2.2-1	Drift Rates Resulting from Incorrect Torque Pulse Weights	16
2.2-2	Torque Pulse Variation when the Torquer Lag is a Significant Fraction of the Pulse Period	17
3.1-1	Orientation of Gyro and System Axes	27
4.1-1	Binary-Torqued Gyro Loop with Second Order Gyro Dynamics	41
4.1-2	Closed Loop Frequency Response as a Function of Float Time Constant	43
4.1-3	Closed Loop Frequency Response Showing the Effect of Sampling	45
4.1-4	Binary-Torqued Gyro Loop when Rotor Bearing Compliance is Considered	46
4.1-5	Potential Frequency Responses of System with Two Stable Limit Cycles	51
4.1-6	Effect of Sampling Rate on Gyro Frequency Response: Significant Rotor Bearing Compliance	53

LIST OF FIGURES (Continued)

<u>Figure No.</u>		<u>Page No.</u>
4.2-1	Simulation Records for Limit-Cycling Binary Gyro	54
4.2-2	Binary Gyro Simulation: 20 Hz Input	56
4.2-3	Binary Gyro Simulation: 165 Hz Input	57
4.2-4	Frequency Response of a Limit Cycling Binary Gyro: Comparison of Analytic and Simulation Results	58
4.2-5	Frequency Response of a Limit Cycling Binary Gyro: Comparison of Analytic and Simulation Results	59
4.2-6	Frequency Response of a Binary Gyro with Rotor Bearing Compliance: Comparison of Analytic and Simulation Results	61
4.3-1	Open Loop Gain-Phase Plot for Uncompensated Binary Gyro	65
4.3-2	Position of Binary Gyro Loop Compensation	66
4.3-3	Closed Loop Gain for Limit Cycling Binary Gyro: Effect of Loop Compensation	68
4.3-4	Block Diagram for Integral-Bypass Compensation	69
4.3-5	Nichols Chart Showing the Effect of Integral Bypass Compensation on Open Loop Response	70
4.4-1	Dithered Binary Gyro	73
4.4-2	Describing Function for the Limiter	73
4.4-3	Frequency Response Characteristics for Binary Rebalance Loop	75
5.1-1	Gyro Pulse Rebalance Loop with a Ternary Nonlinearity	79
5.1-2	Pulse Rebalance Loop Divided into Linear and Nonlinear Parts	82
5.1-3	Ellipses Resulting from Analysis of the Linear Portion of the Loop	82

LIST OF FIGURES (Continued)

<u>Figure No.</u>		<u>Page No.</u>
5.1-4	Output vs Input Computed from the SIDF Gain for the Nonlinearity	83
5.1-5	Superposition of Figs. 5.1-3 and 5.1-4 Showing Intersection Points	84
5.1-6	Ternary Gyro Closed Loop Gain	85
5.1-7	Effect of Input Amplitude on Closed Loop Gain of a Representative Ternary Gyro Loop	86
5.2-1	Ternary Gyro Simulation Records: 20 Hz Input	89
5.2-2	Ternary Gyro Simulation Records: 150 Hz Input	90
5.2-3	Frequency Response of a Ternary Gyro: Comparison of Analytic and Simulation Results	91
5.2-4	Ternary Gyro Simulation Record Illustrating Jump Resonance	92
5.2-5	Frequency Response of a Ternary Gyro: Comparison of Analytic and Simulation Results when Rotor Bearing Compliance is Considered	94
5.3-1	Effect of a Random Input on the Sinusoid Transmission Characteristics of a Ternary Nonlinearity	96
5.3-2	Ellipse Intersection Points Caused by Random Nonlinearity Input	97
5.3-3	Closed Loop Response for a Ternary Gyro with a Certain Random Nonlinearity Input	99
5.3-4	The Effect of σ_r on the Closed Loop Gain	100
6.1-1	Hybrid Simulation of Gyros and Calculation of System Attitude Error	104
6.2-1	Flow Chart for the Digital Part of the Hybrid Simulation	107

LIST OF FIGURES (Continued)

<u>Figure No.</u>		<u>Page No.</u>
A-1	Model for Gyro Case and Float Dynamics	113
A-2	Float Misalignment Time Constant as a Function of Suspension Stiffness K and Damping Constant C_i	117
A-3	Normalized Misalignment Angle Response to a Step Angular Rate About the Gyro Output Axis	118
A-4	Normalized Misalignment for Values of Suspension Stiffness	119
B-1	Exploded View of Single-Degree-of-Freedom Pendulous Accelerometer Showing Small Misalignment Angle, α	122
C-1	Error in the Approximation to the TSIDF	129
D-1	Binary Loop Viewed at the Point where the Signal Quenches the Limit Cycle	133
D-2	Limit Cycle Quenching and Its Effect on Frequency Response (Second Order Gyro Dynamics)	135
D-3	Limit Cycle Quenching and Its Effect on Frequency Response (Rotor Bearing Compliance Considered)	136
D-4	Binary Gyro Simulation Record Showing Limit Cycle Quenching	137
E-1	A Loop Containing One Nonlinear Element	140
E-2	Nonlinearity Input-Output Relation Derived from Analysis of the Linear Portion of the Loop Shown in Fig. E-1	141
F. 1-1	Signal Flow Representation of Gyro Loop Simulation	144
F. 1-2	Mechanization of the Linear Portion of the Gyro Loop	145
F. 1-3	Binary Nonlinearity Mechanization	146

LIST OF FIGURES (Continued)

<u>Figure No.</u>		<u>Page No.</u>
F. 2-1	Ternary Nonlinearity Mechanization	148
G. 1-1	Mechanization Diagram for Eq. (G. 1-1)	151
G. 1-2	Mechanization of Eq. (G. 1-2)	152
G. 1-3	Computer Scaling Used in Simulation of Gyros with Rotor-to-Gimbal Compliance	153
H. 1-1	Conceptual Operation of the Fourier Analyzer	158
H. 2-1	Analog Computer Mechanization of the Fourier Analyzer	159
I-1	Rotor-to-Gimbal Compliance	162
I-2	Signal Flow Diagram of Gyro Loop Including Compliance Effects	165
I-3	Signal Flow Diagram Including Compliance Effects (Compact Form)	165
J. 1-1	Gain Characteristics for Integrating Gyro and Rate Recovery Techniques Expressed in Eq. (J. 1-1)	169
J. 3-1	Angular Rate Estimation Errors: Optimal Linear Filter for Quantized Measurements	174

1.1 VIBRATION-INDUCED ATTITUDE ERRORS IN STRAPDOWN INERTIAL SYSTEMS

The single-degree-of-freedom gyro, originally perfected for use in platform inertial guidance systems, can exhibit large errors when adapted to the strapdown application. The major sources of these new errors are related to the angular motion environment experienced by the gyro when it is rigidly attached to a vehicle. For example, the physical inertias of several components combine with angular motion to generate torques on the float which are erroneously interpreted as angular motion about the sensor input axis. Also, the torquing device used to keep the gyro pickoff angle small is prone to certain inaccuracies and can create significant instrument errors, some of which depend on the angular motion environment.

In the presence of linear or angular vibrations about several gyro axes many of the motion-induced gyro errors can combine to produce constant torques on the float. These are interpreted as a constant angular rate about the gyro input axis and ultimately as a drift rate about the corresponding strapdown system axis. Other error torques generated by angular and linear vibrations do not create constant errors in gyro output. However, as a consequence of the manner in which gyro data is processed in a strapdown system many of these effects can cause large attitude drift rates in the navigator. Prior work, reported in Refs. 1 and 2, indicates that many of the individual motion-induced gyro errors can create strapdown system drift rates well in excess of those commonly quoted for platform inertial navigators.

To permit employment of single-degree-of-freedom gyros in strapdown navigators it is essential that the vibration-induced system errors be analyzed. A more ambitious goal is the ability to synthesize or select the best gyroscope for a given mission-related environment. Presently, however, neither analysis nor synthesis can be performed with confidence because necessary details concerning the behavior of strapdown gyros are difficult to describe mathematically. In particular, the transmission characteristics relating motion-induced error torques to errors in the sensor output are complex because the typical inertial grade strapdown gyro is coupled with a sampled, nonlinear rebalance device. Accurate analysis of vibration-induced strapdown system errors must await development of mathematical descriptions of strapdown gyro transmission characteristics that are simple and accurate over the frequency range of interest.

In Refs. 1 and 2 an attempt was made to analyze the performance of a limit cycling binary gyro. This report extends that approach to cover gyros using ternary and time modulation rebalance techniques. The analyses of the binary and ternary gyros were verified by simulation and several comparisons are presented in Sections 4 and 5. It is concluded that the analytic approach provides a good means of predicting gyro loop transmission characteristics for sinusoidal inputs over most frequencies of interest. Subsequent work will treat gyros employing time modulation torquing and the transmission of random inputs through strapdown gyro loops.

1.2 SUMMARY

References 1 and 2 treat motion-induced gyro error torques, and provide some approximate calculations relating the vibration environment to strapdown system errors. In these two documents an effort was

made to describe analytically the transmission characteristics of a binary, limit cycling gyro loop. The work discussed in this report continues that analysis. Three basic pulse rebalance techniques are described in Section 2. Important considerations in selecting a torquing scheme are discussed and the relative merits of the three approaches are reviewed. A brief discussion treating the propagation of vibration-induced errors through a linear gyro loop is presented in Section 3.

The linear response of a limit cycling binary gyro is shown in Section 4 to depend on the presence of the unforced oscillation in the loop. When inputs of a size and frequency large enough to extinguish the limit cycle occur, the binary gyro loop also exhibits a nonlinear response. However, the conditions under which this occurs are unlikely and can be predicted analytically. The uncompensated binary gyro loop exhibits a highly peaked gain at frequencies below that of the limit cycle. It is demonstrated that dynamic compensation in the gyro loop can reduce the resonant response or cause it to occur at much higher frequencies. In Section 5 the ternary gyro is shown to have a nonlinear closed loop response, particularly to inputs of high frequency. Both binary and ternary gyro loops were shown to suffer a significant deterioration in transfer characteristics if sufficient stiffness is not provided in the rotor bearings. This effect is of less consequence to the ternary gyro because its nonlinear nature would probably preclude use in measuring inputs in the frequency range affected.

Motivation is presented in Section 6 for the construction of a comprehensive strapdown gyro simulation which evaluates system attitude errors. The appendices provide details related to describing function analysis and the gyro simulations used, as well as gimbal suspension design, dynamic errors in pendulous accelerometers and recovery of angular rate information from pulse torqued gyros.

Each major section opens with a summary of the research performed, a synopsis of the results obtained and a brief discussion relating these results to strapdown gyro design.

2.

DESCRIPTION OF PULSE TORQUING SCHEMES

SUMMARY

Three commonly-used nonlinear rebalance techniques for strapdown gyros are treated - binary and ternary delta modulation and time modulation. Important characteristics of pulse rebalance schemes are discussed and the relative disadvantages of each technique are summarized in tabular form. It is concluded that the time modulation approach provides better resolution than either delta modulation scheme while exhibiting no important disadvantages.

2.1 PULSE REBALANCED GYROS

The single-degree-of-freedom gyro consists of a spinning mass supported by a gimbal structure which is free to rotate with respect to the instrument case about one axis. The basic elements of this device are illustrated in Fig. 2.1-1. The axis of gimbal rotation is usually called the output axis and a device is included to measure the output angle, α_0 . In most high quality gyros the wheel and gimbal are enclosed in and attached to a cylindrical structure, or float, and a fluid is inserted between the float and case. The fluid serves two purposes: it provides a buoyant force to unload the gimbal bearings and it damps angular motion between the gyro case and float. In addition to the output axis, two other directions are specified with respect to the instrument case. They are the nominal direction of the rotor spin axis (rotor angular momentum) and the third axis required to define an orthogonal coordinate system. The latter is

usually called the gyro input axis. Angular motion about the input axis creates a gyroscopic torque on the rotor and gimbal assembly, in the direction of the output axis. Specifically, a positive angular rate about the input axis shown in Fig. 2.1-1 generates a negative torque about the output axis. If damping between the case and float is linear and no other torques occur, the output angle is proportional to the integral of angular rate about a direction normal to the output and rotor spin axes.

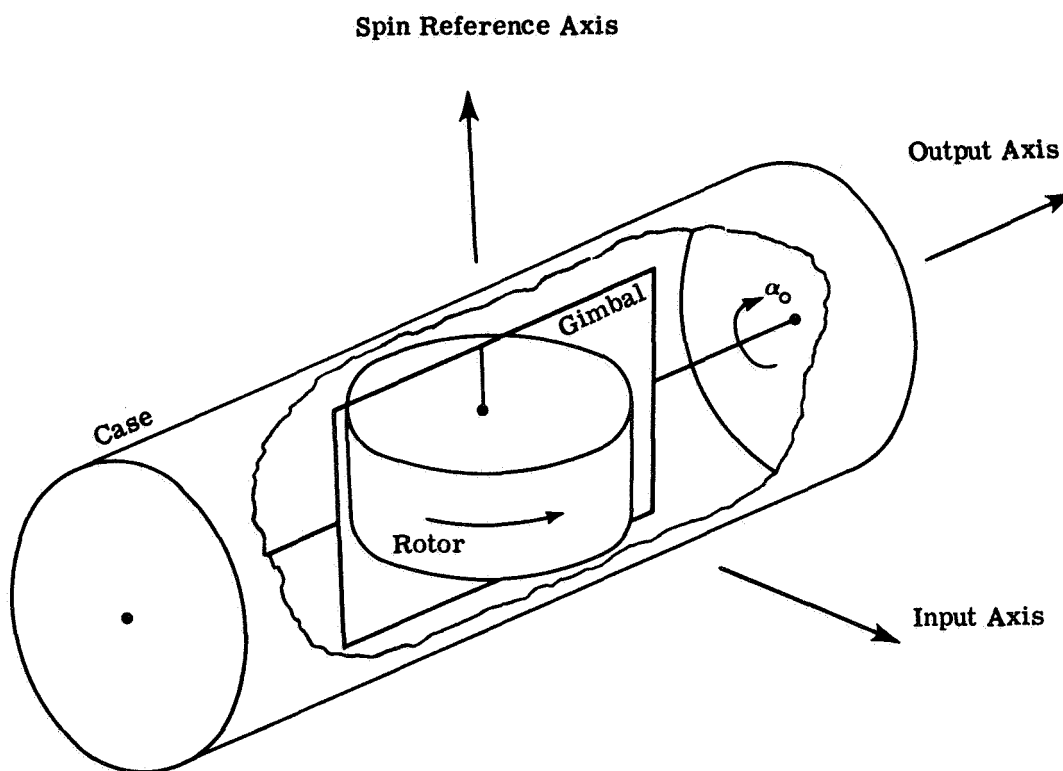


Figure 2.1-1 Single-Degree-of-Freedom Gyro

As the float rotates with respect to the gyro case, the sensitive axis of the instrument moves with it; if the angular rates measured are to be expressed in case-fixed coordinates a transformation must be performed between float and case axis systems. Also, if α_0 is permitted to become

large, a wide angle transducer is required to measure this angle. In most applications the output angle is not allowed to exceed a few milliradians. Consequently, a very accurate pickoff is employed to measure α_0 and the sensitive axis is assumed to be fixed with respect to the instrument case.

In inertial navigators employing a stable platform, gyros of this type are used to sense angular motion with respect to an inertially fixed reference and the platform is rotated in a manner which seeks to null the output angle. Consequently, the sensitive axis of the gyro is always in close coincidence with the case-fixed input axis and α_0 is an accurate measure of angular rotation about that direction. When it is necessary to rotate platform inertial navigation systems relative to a fixed coordinate frame, a mechanism for applying precise torques about the output axis is added to the gyro. The gimbal, rotor and float assembly then acts as a torque summer, interpreting the moment applied by the torque generator in terms of an angular rate about the input axis. Since the platform is rotated in a manner which always nulls the output angle, a true angular rate results, equal in magnitude and of opposite sign from that represented by the torque generator output.

Gyros used in strapdown navigators are likely to experience large angular motions about the case input axis. In order to avoid the complications connected with a large output angle, a powerful torque generator is included in the instrument and the rotor spin axis is kept in close coincidence with the spin reference axis. By keeping the output angle small, variations in α_0 can be attributed to angular motion about the input axis. Information concerning angular motion about the input axis is largely contained in the history of torque required to cage, or restrain, the gyro about its output axis. The equivalence between torque applied to the gimbal and input angular rate is employed in a platform system to generate motion.

The same relation can be used in the strapdown application to imply angular rate from torque. Figure 2.1-2 is a schematic representation of a rebalanced single-degree-of-freedom gyro.

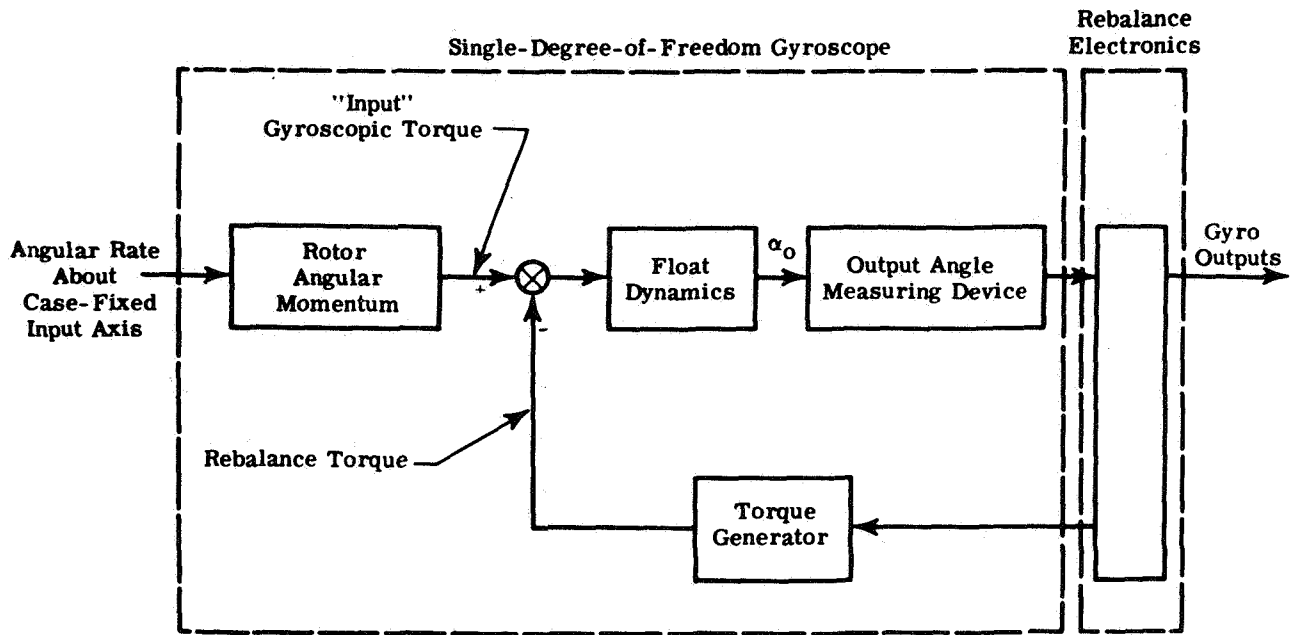


Figure 2.1-2 Rebalanced Gyro Schematic

Direct determination of the torque applied is difficult and most designers rely on measurements of current flow in the torquer windings to indicate the moment produced. Unfortunately, the torque generator does not exhibit a gain characteristic which is sufficiently linear, and if a wide range of torquer currents is employed extensive calibration is required. A common way to avoid problems with torquer nonlinearity to permit application of only two torque levels, equal in magnitude and opposite in sign. (A third, or zero level may also be considered.) In this case, the torque generator need only be calibrated and adjusted at two distinct points on its gain curve, permitting very accurate control of the moments applied to the

gyro output axis. A further refinement to the gyro rebalance mechanism is provided by carefully dividing the torquer current into pulses of known duration. Each pulse then represents an incremental rotation of the gyro about its input axis and the gyro rebalance loop output is well suited for calculating system attitude changes in a digital computer. In the ideal situation, the rebalance torque occurs as a sequence of pulses of positive and negative torque, each pulse having the same weight, and the strapdown gyro output consists of a train of positive and negative electronic impulses accurately representing incremental rotations about the sensor input axis. The single-degree-of-freedom gyro is thus said to be "pulse rebalanced."

Binary Delta Modulation - The binary delta modulation pulse rebalance scheme always provides a rebalance torque. The possibility of omitting a torque pulse is purposely excluded. This mechanization can be represented by a binary logic element inserted between the torquer and a signal representing the gyro output angle (see Fig. 2.1-3). The torquer current, of magnitude D , is supplied with a direction (sign) depending on the sign of the output angle. Pulses of torque are created by only allowing the logic output to change at fixed intervals, T . A further refinement may be employed, permitting torque to be applied only over a known fraction of each interval, but this has little bearing on the aspects of pulse rebalance techniques under consideration here. Figure 2.1-4 shows a representative train of torque pulses applied to a gyro gimbal when binary pulse torquing is employed. The shape of the pulses generated differs from a rectangle because of lags in both the torquer and the current source driving it.

Ternary Delta Modulation - The ternary delta modulation technique differs from the scheme described above by permitting the absence of a torque pulse when the output angle magnitude is small. The mechanization can be represented by a relay with an input deadzone inserted between the output angle signal and the torquer. Figure 2.1-5 illustrates the ternary

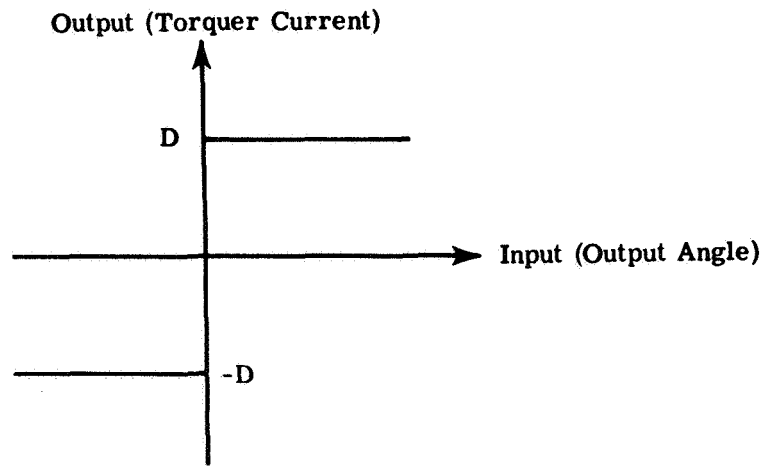


Figure 2.1-3 Two Level Logic

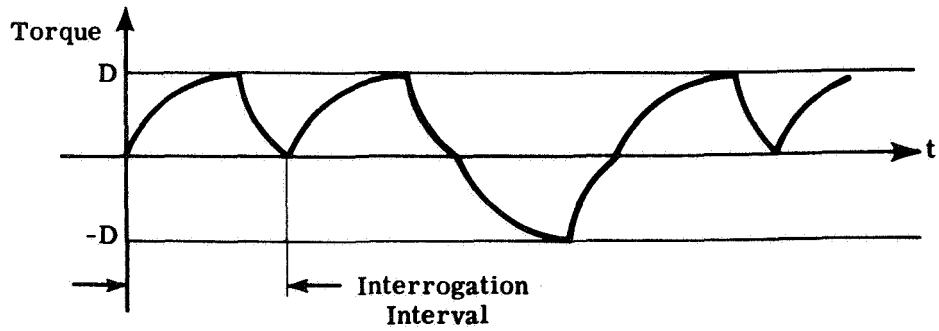


Figure 2.1-4 Representative Torque Output from Delta Modulated Pulse Rebalance Technique

detection logic. The deadzone width, 2δ , is symmetric about zero and defines a range of output angles for which no rebalance torque is applied. For low frequency inputs δ can be related to an angular rotation about the input axis of the gyro which will not be detected. However, for input frequencies above the float bandwidth, the relation is more complex. All other aspects of the ternary delta modulation technique are identical to those of the binary approach just discussed.

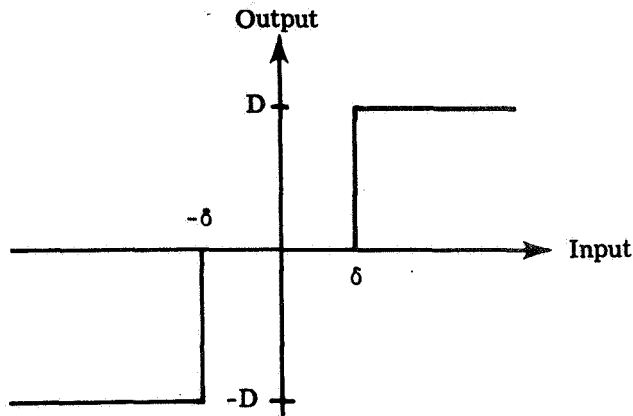


Figure 2.1-5 Three Level Logic

Time Modulation - A third pulse torquing technique, time modulated torquing, adds the gyro output angle to a periodic waveform and employs binary logic on the sum. Figure 2.1-6 illustrates this approach. The binary logic is interrogated at a frequency which is a multiple of the sawtooth frequency. In this manner, each period of the added waveform is divided into an even integral number of parts. Current driving the torque generator can only be switched at the moment the binary logic is interrogated.

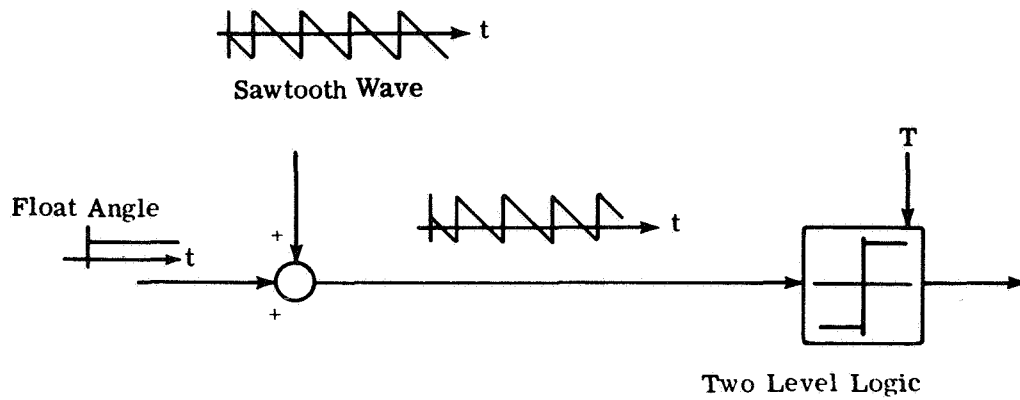


Figure 2.1-6 Time Modulated Torquing

If the output angle is at null, the torquer provides a pair of pulses, one positive and one negative. The torque pulses are of equal duration and occur at the frequency of the sawtooth wave. The net effect of each pulse pair on the output angle is zero, but the float will oscillate at the sawtooth frequency. To avoid detecting this float oscillation the signal representing output angle is usually passed through an appropriate filter. If the filtered indication of output angle differs from null, the pulse pairs appear at the same frequency but the pulses in each pair are of different duration, as illustrated in Fig. 2.1-7. The difference between the length of two adjacent pulses is such that the net effect is to drive the output angle toward null. The sawtooth amplitude is chosen to ensure that the torquer always provides a moment in the same direction at the start of each sawtooth period; the amplitude of the added waveform is larger than any anticipated signal representation of α_0 . For this reason, the torquer current always changes sign at the start of a new sawtooth. Also, the current is only allowed to reverse once during each period of the added waveform. These restrictions ensure the appearance of one positive and one negative pulse, in the same sequence, each sawtooth period.

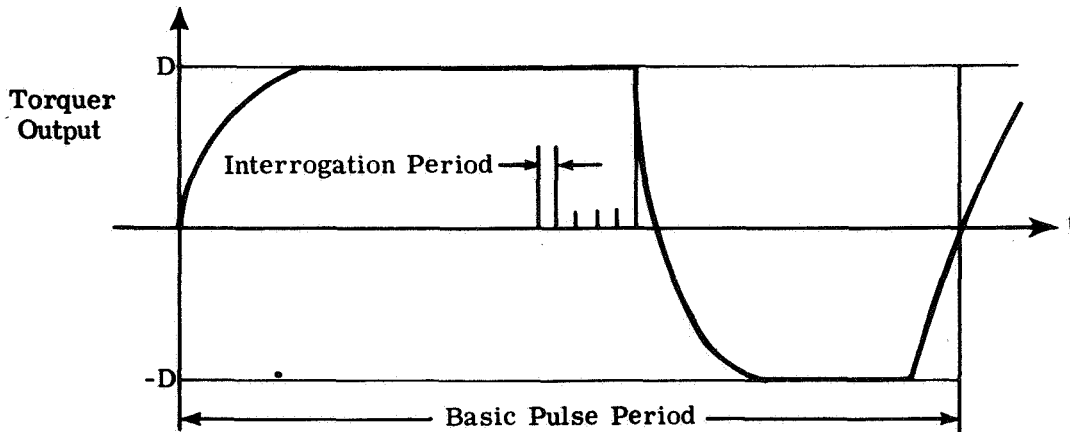


Figure 2.1-7 Torquer Waveform for Time Modulated Torquing

When time modulated torquing is employed, the gyro output can take two forms. A pulse sequence can be provided at an even multiple of the sawtooth frequency, corresponding to the rate at which the binary logic is interrogated. In this case, the output would appear as a long series of pulses of one sign followed by a long series of pulses with the opposite value. Each pulse represents an incremental rotation about the input axis, of a magnitude determined by the torquer capability and the interrogation frequency. Most of the information contained in this form of output represents the added waveform. Only the difference between the number of pulses in two successive series can be construed to represent α_0 and consequently motion about the gyro input axis. Commonly, this difference is determined by summing pulses over each period of the sawtooth. The net difference, available at the frequency of the sawtooth wave, represents the information content of the gyro output. Since the sawtooth typically has a one millisecond period this alternate form of the gyro output has a bandwidth compatible with many of the computers used to process angular motion information.

If a fixed increment Digital Differential Analyzer (DDA) is used to process gyro outputs, the high frequency pulse train can be employed. However, as stated earlier most of the information contained is related to the oscillatory signal that was added to α_0 and the attitude calculations will exhibit this oscillation. If all gyros are not provided with the same sawtooth wave serious pseudo-coning system drift rates can be caused.

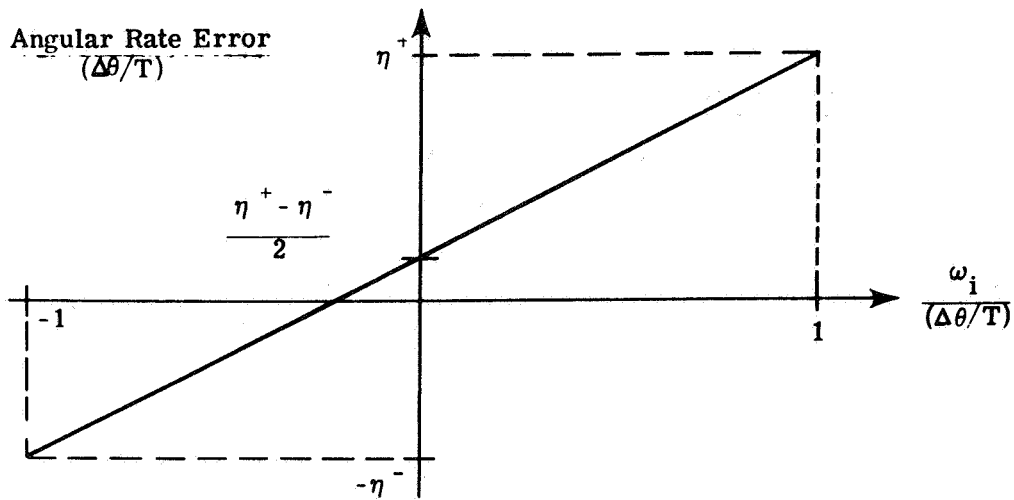
Summary - All three pulse torquing techniques provide digital outputs which represent increments of angular rotation about the sensor input axis. The angular rotation is implied from a carefully calibrated torque pulse applied to the gyro gimbals when a pulse occurs. Any deviation of the actual time integral of torque from that represented by each output pulse will cause an error which is not recoverable, i.e., differs in nature from gyro output errors caused by storage of information by the float. Constant deviation of the torque pulse can cause constant gyro drift rates while random variations provide random output errors. Differences between the net torque pulse generated and that implied by each output quantum are a major source of errors in strapdown sensors.

When system accuracy is considered, factors such as quantization and the information rate of pulse rebalanced gyros are important. The presence of unforced oscillations in the gyro output is also considered when comparing strapdown gyro torquing schemes. In addition, frequency response characteristics and energy dissipation in the gyro loops are significant. The major causes of pulse rebalancing errors are described below, followed by a discussion of the relative advantages of each torquing scheme.

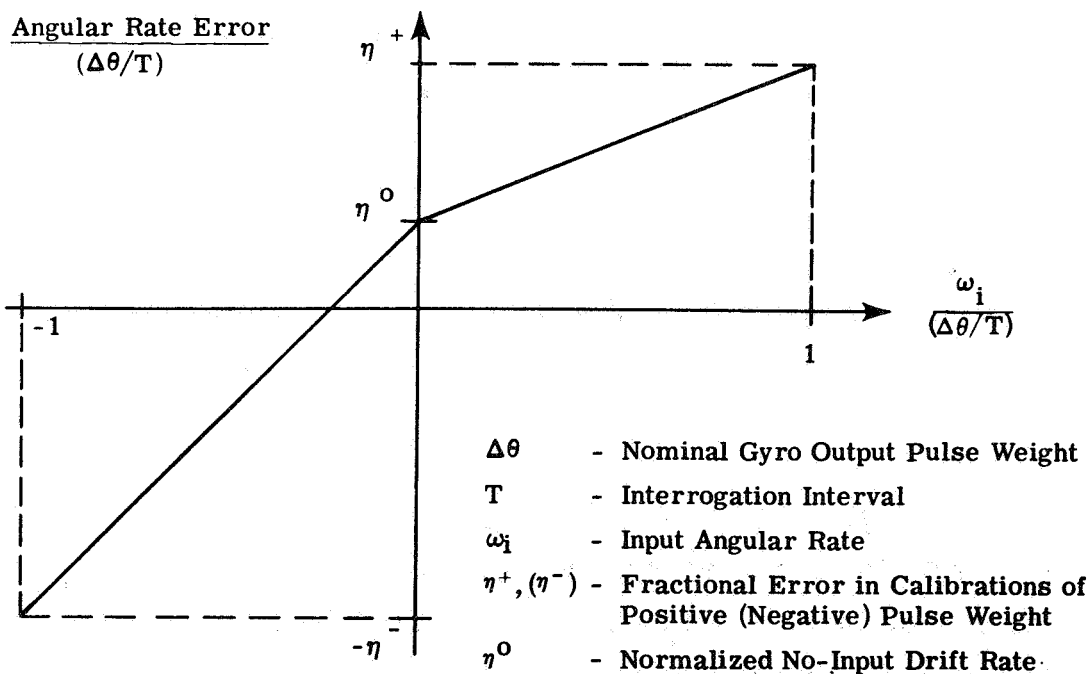
2.2 ASPECTS OF PULSE TORQUING GYRO ERRORS

Torque Pulse Variations - Frequently the magnitudes of torque pulses applied to the float differ from those inferred by the corresponding electrical impulses at the gyro output. If the deviations are constant, calibration of the strapdown gyro loop will eliminate some of the errors generated. From Fig. 2.2-1 it can be seen that a bias error can result for both the binary and ternary pulse rebalanced sensors. Also scale factor errors are present in both instruments. However, removing errors of this kind from the ternary gyro generally requires two scale factor corrections. The correction used at a particular time depends on the sign of the input angular rate. This represents an unwanted complication in processing the gyro output. When the rebalance electronics drift, causing uncompensated variations in torque pulse weights, new bias and scale factor errors in the binary gyro result. The bias error is caused by the fact that torque pulses are always being generated in the binary rebalance loop. It is independent of the angular motion environment. On the other hand, only scale factor errors are generated in the ternary loop when the rebalance electronics drift. Consequently, if the input angular rates are small the ternary gyro will be less sensitive to unknown variations in torque pulse weights.

Quantization - The output of each pulse rebalanced strapdown gyro is a series of digital pulses representing incremental rotations about the input axis. This form is not well suited for drift-free calculation of the direction cosine matrix because information is lost regarding the order in which rotations take place about the system axes. The commutativity errors which can result are largely related to the gyro output quantization level and the manner and speed with which the outputs are processed. (Reference 4 provides an approximate expression for commutation errors generated by gyro output quantization. In the relation stated there, the



(a) Binary Torquing



(b) Ternary Torquing

Figure 2.2-1 Drift Rates Resulting from Incorrect Torque Pulse Weights

drift rate about a particular axis is given by half a gyro output quantum multiplied by the difference in angular rates experienced about the other two axes.) As a general rule, fine quantization is to be preferred.

Delta modulation pulse torquing schemes achieve fine quantization by interrogating the nonlinear logic element at a high frequency, premitting the torque level to change sign rapidly. While the size of the output quantum in the time modulation technique is also determined by the interrogation frequency, the rate at which torquer current changes sign is determined by the frequency of the sawtooth wave. In gyros employing delta modulation rebalance schemes, quantization is limited by time constants in the torque generation mechanisms. If the pulses are of too short a duration, the torquer current will not reach its design level before the next potential switching time occurs. Because of eddy current effects, when the torquer lag is on the order of the pulse period, two consecutive torque pulses in the same direction will not have the same time integral (effect on α_0) as the sum of two separate pulses (see Fig. 2.2-2). Consequently, all current pulses will not have equal weight and an accurate measure of angular motion about the gyro input axis cannot be found by counting output pulses.

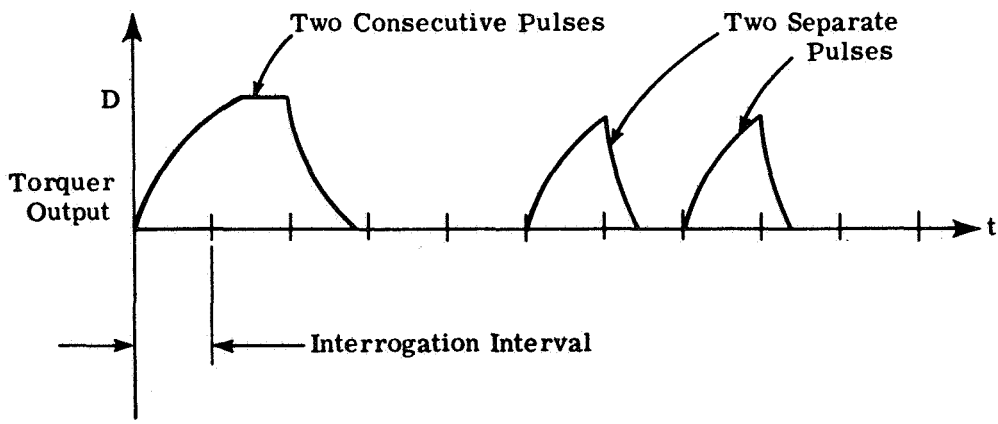


Figure 2.2-2 Torque Pulse Variation when the Torquer Lag is a Significant Fraction of the Pulse Period

In the time modulation torquing scheme, quantization is not tied directly to torque pulse width. The current switching frequency is strictly limited and quantization is determined by the number of points in each cycle of the sawtooth at which the torque can change sign. In the absence of switching delays, infinitesimal quantization is possible. The practical limit is imposed by the ability to switch the torque levels accurately in time. Using this approach, torquer time constant problems are eliminated by choosing the amplitude of the added waveform so that torquer current always reaches the desired level before the next change occurs.

Information Rate - The information rate, defined here as the frequency with which new indications of system angular motion will be available to the attitude transformation computer, can depend on the pulse torquing technique chosen. Typically, a gyro with time modulation rebalance torquing can provide output impulses faster than one using either of the delta modulation approaches. Each impulse is interpreted as an increment of angular rotation about the instrument's input axis. However, as discussed earlier, most of the information actually present in the raw output of this rebalance technique relates to the oscillatory signal added to α_0 and not to angular motion experienced by the gyro. The information rate of a gyro employing time modulated torquing is essentially limited by the frequency of the additive oscillatory signal used in mechanizing this approach. It would then appear that the information rate of gyros using the delta modulation approach to rebalance torquing is higher than those employing the time modulation technique, when present interrogation frequencies are considered. However, the practical rate at which angular motion can be sensed by this kind of strapdown gyro is usually limited by lags in the float dynamics, not the sampling frequency; output pulses which change sign at a rate near that of the interrogation clock are more likely to be caused by electrical noise than high frequency motion inputs. In

summary, the useful information rate of a contemporary floated single-degree-of-freedom strapdown gyro generally is limited not by the pulse rebalance technique employed but by float dynamics.

Unforced Oscillations - All three pulse torquing schemes produce unforced oscillations in the gyro loop at one time or another. The limit cycle behavior of a control loop containing a binary nonlinearity is well known (Ref. 1). In the presence of many inputs, the three level pulse torqued gyro and the time modulation scheme will also exhibit cyclic errors. The unwanted oscillations all result from the use of torque pulses to rebalance the gyro. Limit cycles in pulse rebalanced gyros can be mistaken for coning motion if they occur with proper phase and at the same frequency. System attitude drift rates are generated in this manner. The binary delta modulation scheme is usually thought to be the least satisfactory from this point of view. However, it can be shown that slight differences between limit cycle periods of the different gyros in a strapdown triad will prevent large system errors of this type (see Ref. 1). Thus, gyros with slightly different characteristics may be desired.

Gyro Frequency Response Characteristics - Closed loop response to sinusoidal inputs is a useful description of behavior. Closed loop gain and phase shift characteristics are useful in determining strapdown system errors when the gyro loop is assumed to be linear (see Section 3). Approximate determination of these characteristics is discussed in this report for all three rebalance techniques. Torque loops employing binary logic appear to be more readily described in terms of linear behavior than those using ternary logic (see Section 5.1), offering an advantage when analyzing and compensating dynamic system errors.

Energy Dissipation - Temperature gradients within the gyro structure are a major cause of single-degree-of-freedom gyro drift. If the gradients can be held constant, proper testing will enable accurate compensation of these effects. While it consumes less power in most motion environments, the ternary delta modulation torquing scheme does not usually provide a uniform energy flow into the torquer. To avoid this obvious cause of varying temperature gradients, the current source can be switched into a dummy load when no torque is called for. However, if the same heat pattern is to be produced, this requires a dummy winding the same size as the torquer. Situations do exist where the ternary technique will provide essentially constant energy flow without the extra winding. For example, while operating in the angular rate environment generated by a limit cycling spacecraft attitude control system.

2.3 COMPARISON OF PULSE TORQUING TECHNIQUES

Binary Delta Modulated Torquing - The binary delta modulation rebalance technique provides a gyro loop response which is linear because of the limit cycle always present in this kind of system. However, some compensation within the gyro loop may be desired to improve its behavior. Because torque is always being generated, energy is dissipated within this kind of an instrument at a constant rate and no significant errors are caused by variations in temperature gradients. A high rate of power consumption results, even in the most benign motion environment. A limit cycle is always present in this instrument and consequently strap-down system attitude drift rates can result. The output quantization level of a gyro using this rebalance technique is limited by torquer dynamics and the output resolution is generally poorer than can be obtained from sensors using time modulation torquing. Also, the instrument is relatively sensitive to uncompensated deviations in the size of rebalance torque pulses.

Binary delta modulation requires a minimum of electronic components, suggesting better reliability. Section 4.1, 4.2 and 4.3 of this report treat aspects of binary pulse torquing.

Ternary Delta Modulated Torquing - Gyros employing ternary delta modulated torquing can conserve electrical energy in a benign environment such as that encountered during long space missions. In addition, there is less tendency to exhibit cyclic output errors. Because a null torquer current can be achieved with high accuracy, they usually have a lower drift rate in the absence of an input and are less sensitive to deviations in torque pulse size. However, in a variable environment unstationary temperature gradients can be generated inside the instrument unless a dummy electrical load is used to dissipate energy when no torque pulse is called for. If this additional device is added to the gyro, low power consumption is sacrificed and the weight and size of the instrument are increased. As with the gyro using binary delta modulated torquing, the ternary rebalanced sensor suffers from an output resolution that is limited by torquer dynamics. A gyro loop using this torquing scheme exhibits a nonlinear response to high frequency inputs, casting doubt on its value as a strapdown sensor in vigorous angular vibration environments. The ternary gyro also displays multi-valued response characteristics in the high frequency range. Section 5 of this report deals with the ternary pulse rebalanced gyro.

Time Modulated Torquing - The output resolution of a gyro employing time modulated torquing is essentially independent of torquer dynamics. Consequently, this type of instrument uses finer quantization than is commonly found in other pulse rebalanced gyros. An oscillatory error can appear in the gyro output but this is much smaller than those occurring with binary delta modulation techniques. A high power consumption is characteristic of this rebalance scheme but temperature gradients

within the device are held constant. This type of instrument exhibits a relatively large sensitivity to variations in torque pulse weight. Analysis indicates that a more satisfactory linear response can be obtained from this type of gyro than is possible using simple binary torquing in an uncompensated loop. Of the three techniques discussed, time modulated torquing requires the largest number of electronic components.

Summary - The three pulse torquing techniques discussed are compared in Table 2.3-1. Some representative values of important parameters are listed to aid in the comparison. None of the approaches discussed offers a clear advantage in all situations. If constant energy dissipation over a wide range of inputs and linear response are required at the outset, the ternary approach can probably be ruled out. However, when the angular motion environment is quiet and reasonably constant the ternary gyro has the advantage of low power consumption and is less affected by torque pulse deviations. All three techniques appear capable of providing the same information rate, but the time modulation approach can give better output resolution because it permits output quantization to be specified independent of the torquer design.

TABLE 2.3-1

COMPARISON OF
PULSE TORQUE TECHNIQUES

UNDESIRABLE FEATURES	REBALANCE TECHNIQUES			COMMENTS
	BINARY DELTA MODULATION	TERNARY DELTA MODULATION	TIME MODULATION	
Output Quantum Level Limited by Torquer Dynamics.	x	x		Gyro output quantum, $\Delta\theta$, is independent of torque lags when the time modulation technique is employed.
	$\Delta\theta_{\min} > 3\omega_{i\max} r_{tg}$ about 20 sec or more when $\omega_{i\max} = 1 \text{ rad/sec}$		$\Delta\theta < 1 \text{ sec}$ for the Hamilton Standard RI-1170 under similar circumstances.	
Unforced Oscillations in the Sensor Output.	x		x	Ternary gyro can also exhibit output oscillations. The finer quantization available with the time modulation schemes reduces the amplitude of these errors.
Amplitude Dependent Response Characteristics.		x		See Fig. 5.1-7 for an illustration of the amplitude dependent response characteristics of the ternary gyro.
Nonstationary Temperature Gradients in the Gyro.		x		This can be avoided in the ternary gyro also but at the expense of significant increases in torquer size and weight.
High Power Consumption in a Benign Environment.	x		x	The ternary gyro also suffers this problem if a dummy electrical load is added to give stationary temperature gradients.

3.

STRAPDOWN SYSTEM ATTITUDE ERRORS
ARISING FROM VIBRATIONAL MOTION

SUMMARY

The system attitude drift rate caused by the interaction of vehicle vibrations and single-degree-of-freedom (SDF) gyro parameters is discussed. Major sources of system drift rate are developed followed by a discussion of possible gyro parameter selections to reduce attitude error. It is assumed that the gyros can be represented by a linear transfer function relating torque on the float to sensor output. No errors are presumed to be generated in the calculations used to process gyro outputs. The importance of simple analytic descriptions of gyro loop transfer characteristics is discussed.

3.1 DESCRIPTION OF GYRO AND VIBRATION CHARACTERISTICS

The error torques on a single-degree-of-freedom gyro are developed in Ref. 1. In the discussion which follows these torques are assumed to propagate through a linear gyro loop whose Laplace transform transfer function is represented as $G(s)$. At any particular frequency of input the in-phase and quadrature components of the gyro output are specified by decomposing $G(s)$ into real and imaginary parts:

$$G(s) \Big|_{s = j\nu} = \text{Re } G(\nu) + j \text{Im } G(\nu) \quad (3.1-1)$$

The correlation characteristics of angular and linear vibrations are described in terms of spectral density functions when only one axis is considered and the components of cross spectral density, cospectrum and quadspectrum, when two axes are considered. For example, when angular vibrations are described the spectral density is represented by the symbol $\Phi_{rr}(\nu)$, which is the mean product of angular rate oscillations at frequency ν , about the r axis. When angular motion about two different axes is under consideration the cospectral density function $\Phi_{rs}(\nu)$ represents the mean product of two angular rate oscillations at frequency ν , one about the r axis, the other about the s axis. Only those components of the oscillations which are in phase provide contributions to Φ_{rs} . To describe vibrations that are correlated but in quadrature, a quadspectral density function $\Phi'_{rs}(\nu)$ is defined. It is the mean product of the angular rate oscillation about the r axis and the vibration about the s axis phase shifted $\pi/2$ radians. To illustrate, suppose the spin and input axes of a particular gyro experience the following angular rates:

$$\begin{aligned}\omega_s &= a \sin \nu t \\ \omega_i &= b \sin \nu t + c \cos \nu t\end{aligned}$$

Then;

$$\begin{aligned}\Phi_{ss}(\nu) &\triangleq \frac{a^2}{2} \\ \Phi_{ii}(\nu) &\triangleq \frac{b^2 + c^2}{2} \\ \Phi_{is}(\nu) &\triangleq \frac{ab}{2} \\ \Phi'_{is}(\nu) &\triangleq \frac{ac}{2}\end{aligned}$$

Similar spectral density functions which describe the correlation characteristics of linear vibrations are designated $\Psi_{RR}(\nu)$, $\Psi_{RS}(\nu)$ and $\Psi'_{RS}(\nu)$. It is assumed that all necessary density functions are known.

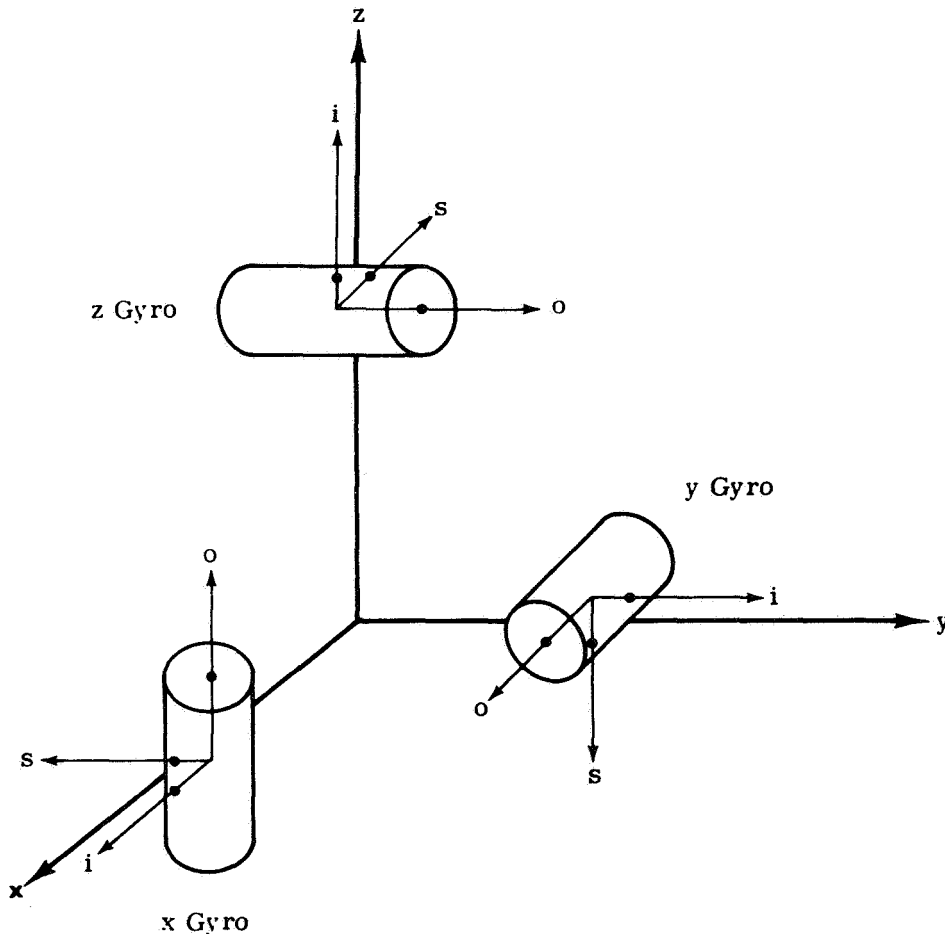


Figure 3.1-1 Orientation of Gyro and System Axes

In order to relate system error growth to vibration-induced gyro errors the orientation of each gyro with respect to the vibration axes must be specified. The most general orientation is used here. The strapdown system (vehicle body) axes in which the vibration spectral density information is stated are designated x, y and z. The gyro which measures angular motion about the x axis has, of course, its input axis in the x direction.

The spin and output axes of this sensor are parallel to the y and z system axes. The gyro measuring angular motion about the y axis has its spin and output axes parallel to the z and x directions, etc. Figure 3.1-1 illustrates the relative orientation of gyro and system axes.

3.2 DRIFT RATE CONTRIBUTIONS

Only constant system attitude drift rates are considered here. The causes discussed below represent the major contributors to vibration-induced system drift rate. However, the list is not necessarily complete.

3.2.1 Spin-Input Crosscoupling

This error is caused by coupling between angular motion about the nominal rotor spin axis and a float angle generated by angular motion about the gyro input axis. It can result in a constant drift rate component in the individual gyro. The float angle is given by

$$\alpha_0(s) = \frac{-H \omega_i(s)}{K_{sg} K_{tg}} G(s)$$

where

- H = gyro angular momentum
- ω_i = angular rate about the input axis
- K_{sg} = signal generator gain
- K_{tg} = torquer gain

The average value of the vibration-induced gyro drift rate $\omega_s \alpha_0$ is given by

$$\begin{aligned}
 -\overline{\alpha_0 \omega_s} &= \frac{H}{K_{sg} K_{tg}} \overline{\omega_i(s) \omega_s(s) G(s)} \\
 &= \frac{H}{K_{sg} K_{tg}} \int_0^\infty d\nu \left[\text{Re } G(\nu) \Phi_{is}(\nu) - \text{Im } G(\nu) \Phi'_{is}(\nu) \right]
 \end{aligned}
 \tag{3.2-1}$$

3.2.2 Spin-Output Crosscoupling

This error is caused by angular motion about the nominal rotor spin axis and a float angle generated by angular acceleration about the gyro output axis. It can result in a constant drift rate in the individual gyro. The float angle is given by

$$\alpha_0 = \frac{-I_{00} \dot{\omega}_0(s)}{K_{sg} K_{tg}} G(s)$$

where

I_{00} = moment of inertia of the gimbal
and rotor about the output axis

The average value of the vibration-induced drift rate is given by

$$\begin{aligned}
 -\overline{\alpha_0 \omega_s} &= \frac{I_{00}}{K_{sg} K_{tg}} \overline{\dot{\omega}_0(s) \omega_s(s) G(s)} \\
 &= \frac{-I_{00}}{K_{sg} K_{tg}} \int_0^\infty \nu d\nu \left[\text{Re } G(\nu) \Phi'_{os}(\nu) + \text{Im } G(\nu) \Phi_{os}(\nu) \right]
 \end{aligned}
 \tag{3.2-2}$$

3.2.3 Anisoinertia

This error is caused by a mismatch of moments of inertia about the spin and input axes, in combination with angular motion about these two axes. Spin axis angular motion of the gyro case and gimbal is transferred to the rotor through the wheel speed control loop. Consequently, the spin axis inertia of the rotating member can be considered coupled to the float only at vibration frequencies below the bandwidth of this control loop; the anisoinertia is a function of frequency. Anisoinertia error torques can cause constant vibration-induced drift rates in the individual gyro. The drift rate is given by

$$\begin{aligned} \text{anisoinertia drift rate} = & -\frac{1}{H} (I_{ii} - I_{SSg}) \omega_i \omega_s \\ & + \frac{I_{SSr}}{H} Q(s) \omega_i \omega_s \end{aligned}$$

where

- I_{ii} = rotor and gimbal moment of inertia about the input axis
- I_{SSg} = gimbal moment of inertia about the spin axis
- I_{SSr} = rotor moment of inertia about the spin axis

Rotor inertia coupling about the spin axis is represented by the transfer function

$$Q(s) \cong \frac{\omega_r^2}{s^2 + \omega_r^2}$$

where

$$\omega_r = \text{wheel speed control loop bandwidth}$$

The expression for the average anisoinertia drift rate is

$$\text{average anisoinertia drift rate} = \frac{-1}{H} \int_0^{\infty} d\nu (I_{ii} - I_{SSg} - I_{SSr} Q(\nu)) \Phi_{is}(\nu) \quad (3.2-3)$$

3.2.4 Torquer Scale Factor Asymmetry

This error is caused by a lack of symmetry in the gain (scale factor) relating gyro output to the rebalance torque applied. In a gyro with linear rebalance electronics, a sinusoidal angular rate about the input axis

$$\omega_i = W \sin \nu t$$

will cause a mean drift rate of $-\epsilon W/\pi$ if the frequency ν is within the loop bandwidth and the torquer gain for applying positive rebalance moments is $(1 + \epsilon)$ times that for negative moments. The same drift rate occurs in a pulse rebalanced gyro when positive and negative pulses are similarly unequal (see Ref. 1). For the linear gyro the mean drift rate caused by scale factor asymmetry and angular vibrations is given by

$$\text{mean drift rate caused by scale factor asymmetry} = -\frac{\epsilon}{\pi} \left[\int_0^{\infty} d\nu |G(\nu)|^2 \Phi_{ii}(\nu) \right]^{1/2} \quad (3.2-4)$$

3.2.5 Pseudo-Coning

The cause of this system level error is the combination of an angular vibration correctly measured by one gyro with a vibration-induced error from a second gyro. The strapdown navigator erroneously believes that it is experiencing coning motion and a system drift rate occurs about the third system axis. The major cause of pseudo-coning system errors is the sensitivity of the single-degree-of-freedom gyro to angular acceleration about its output axis. This effect provides an error signal of the proper phase to combine with the true motion measured by another gyro, giving the erroneous indication of system coning motion. The average pseudo-coning error per gyro pair (of which there are three in each system) is

$$\text{pseudo-coning drift rate} = \frac{-I_{00}}{H} \int_0^{\infty} d\nu \Phi_{00}(\nu) |G(\nu)|^2 \quad (3.2-5)$$

3.2.6 Undetected System Coning Motion

If the angular vibration environment contains frequencies beyond the gyro bandwidth, the system can experience coning motion which is not detected by the gyro. The mean drift rate due to undetected angular rotation about the system z axis is given by

$$\text{undetected coning drift rate} = - \int_0^{\infty} \frac{d\nu}{\nu} (1 - |G(\nu)|)^2 \Phi_{xy}(\nu) \quad (3.2-6)$$

Similar expressions can be written for drift about the x and y axes by proper permutation of the subscripts on the quadspectral density function.

3.2.7 Linear Vibration Errors

Linear vibrations can cause error torques about the output axis of an SDF gyro. Compliance in the gimbal and rotor structure is the mechanism for rectifying the effects of linear vibrations to generate constant drift rates in the individual gyros. If the structural compliance coefficients K_{ij} , relating rotor center of mass displacement in the i direction to acceleration in the j direction, are constant the mean drift rate per gyro is

$$\begin{aligned} \text{linear vibration} \\ \text{drift rate} = \frac{m^2}{H} \int_0^{\infty} d\nu \left[K_{so} \Psi_{oi}(\nu) + K_{si} \Psi_{ii}(\nu) \right. \\ \left. + (K_{ss} - K_{ii}) \Psi_{is}(\nu) - K_{io} \Psi_{os}(\nu) \right. \\ \left. - K_{is} \Psi_{ss}(\nu) \right] \end{aligned} \quad (3.2-7)$$

where

$$m = \text{rotor mass}$$

Unfortunately, the compliance coefficients can be frequency dependent and Eq. (3.2-7) is a very simple representation of linear vibration errors. For a more detailed treatment see Ref. 7.

3.3 SYSTEM DRIFT RATE

The system drift rate about any axis can be found by referring to the gyro orientation and properly summing appropriate drift rate terms from Section 3.2. For example,

mean x-axis system drift rate =

$$\begin{aligned}
 & - \frac{\epsilon_x}{\pi} \left[\int_0^\infty d\nu |G(\nu)|^2 \Phi_{xx}(\nu) \right]^{1/2} \\
 & + \int_0^\infty d\nu \left\{ \text{Re } G(\nu) \left[\frac{I_{00}\nu}{K_{sg}K_{tg}} \Phi'_{zy}(\nu) - \frac{H}{K_{sg}K_{tg}} \Phi_{xy}(\nu) \right] \right. \\
 & + \text{Im } G(\nu) \left[\frac{I_{00}\nu}{K_{sg}K_{tg}} \Phi_{yz}(\nu) + \frac{H}{K_{sg}K_{tg}} \Phi'_{xy}(\nu) \right] \\
 & + \frac{1}{H} (I_{ii} - I_{ssg} - I_{ssr} Q(\nu)) \Phi_{xy}(\nu) \\
 & - \frac{I_{00}}{H} \Phi_{zz}(\nu) |G(\nu)|^2 - \frac{1}{\nu} (1 - |G(\nu)|)^2 \Phi'_{yz}(\nu) \\
 & + \frac{m^2}{H} \left[K_{so} \Psi_{xz}(\nu) + K_{si} \Psi_{xx}(\nu) + (K_{ii} - K_{ss}) \Psi_{xy}(\nu) \right. \\
 & \quad \left. + K_{io} \Psi_{yz}(\nu) - K_{is} \Psi_{yy}(\nu) \right] \left. \right\}
 \end{aligned} \tag{3.3-1}$$

Some observations regarding gyro design can be made from Eq. (3.3-1). If $\Phi_{xy}(\nu)$ is significant only in a narrow range of frequencies, adjusting the wheel speed regulator to provide a constant value of $Q(\nu)$ over that band will permit elimination of the aniso inertia drift rate by proper selection of gimbal moments of inertia. All other errors induced by angular vibration are in some way affected by the gyro loop response, represented by the expression $G(\nu)$. Torquer asymmetry and pseudo-coning errors can be diminished by reducing the gyro bandwidth. However, at least for the linear gyro, reducing bandwidth will increase crosscoupling errors and will cause information to be lost (for example, there will be more undetected coning motion). Evidently, determination of the optimum gyro parameters is not a trivial problem and is intimately

involved with the model of gyro transfer characteristics. While specifying $G(\nu)$ is easy when a linear rebalance technique is used, most strapdown gyros employ pulse torquing. The nonlinear elements in a pulse rebalanced gyro complicate the description of transfer characteristics for this type of instrument. Consequently, Eq. (3.3-1) cannot be used in a straightforward manner to compute vibration-induced errors or as the basis for selecting gyro parameters. The following two sections of this report outline attempts at describing the response characteristics of pulse rebalanced gyros in a concise manner that will facilitate calculation of vibration-induced errors.

BINARY PULSE REBALANCED GYROSUMMARY

Research Performed - An analytic technique is used to predict the behavior of binary pulse torqued gyros. In particular, closed loop frequency response characteristics are determined for limit cycling delta modulated gyros and for instruments employing time modulated torquing. Most of the effort is devoted to analysis of sensors employing the binary delta modulation rebalance technique. For these gyros the effects of interrogation period, float time constant and rotor bearing compliance are investigated and a gyro simulation is employed to verify the behavior predicted analytically. The influence of various compensation networks on closed loop behavior is also discussed.

In this section the effect of sampling in the rebalance loop is represented as a linear, first order lag in the gyro loop. Rotor bearing compliance is modeled in terms of a linear, lightly damped spring-mass system.

Results - Because of the limit cycle usually exhibited, the binary gyro is shown to have an essentially linear response to sinusoidal inputs. Good agreement is observed between the closed loop gain and phase shift characteristics determined analytically and those observed during simulation. Analytic techniques are also shown to accurately forecast limit cycle quenching - the situation where the input signal extinguishes the limit cycle in a binary gyro. It is demonstrated that the effect of sampling on gyro loop behavior can be studied in terms of an equivalent first order dynamic lag. An analysis is also performed for a strapdown gyro loop employing a time modulation torquing technique. It is concluded that this rebalance

scheme can provide more flexibility in achieving a desirable closed-loop gain characteristic. The analysis is not checked by a simulation.

Conclusions Related to Gyro Design - A tool for analyzing binary strapdown gyro designs as demonstrated. However, at present it has only been validated for the case of sinusoidal inputs. Further work is required before the same analytic approach can be used with confidence to compute vibration-induced strapdown system errors. This technique is not limited to a particular set of linear dynamics within the loop and accurately predicts what range of input frequencies will be distorted by the gyro. An uncompensated limit cycling binary loop exhibits a frequency response that can be closely approximated by a linear, second order transfer function whose damping ratio and natural frequency are given by Eqs. (4.1-1) and (4.1-2). Unfortunately, the damping ratio of the approximate system never exceeds one-half, giving high peaks in the closed-loop gain. It is demonstrated that the response characteristics of a limit cycling binary gyro can be changed by inserting linear dynamic compensation between the signal generator and the rebalance logic.

Rotor bearing compliance can have a sizeable effect on the closed loop transfer characteristics of a single-degree-of-freedom gyro. Stiff rotor bearings must be provided to enable a strapdown gyro to realize its full potential. Sampling in the gyro rebalance loop also lowers the bandwidth and the highest sampling rate compatible with other constraints should be used.

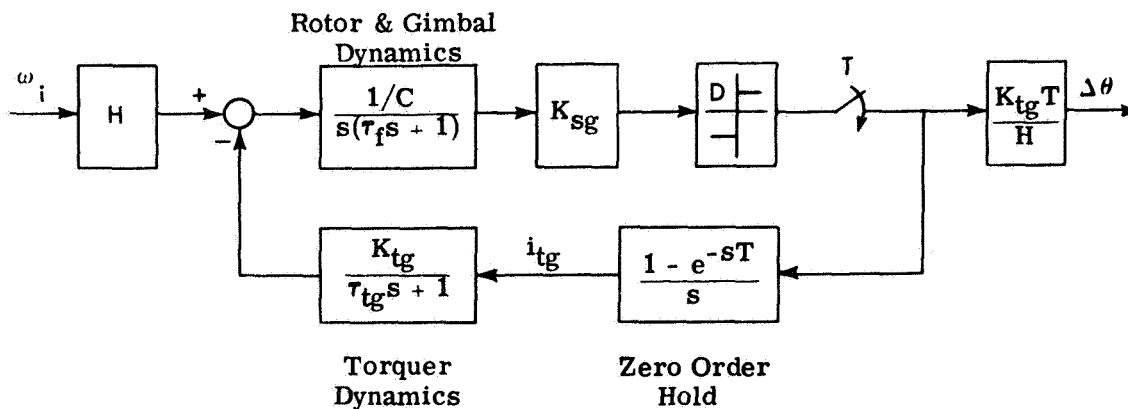
The float time constant affects binary strapdown gyro bandwidth. Generally, reducing this parameter raises the natural frequency and damping ratio of the approximate loop response model.

Quenching of the binary gyro limit cycle and, consequently, destruction of the linear response characteristics of this sensor can be accurately predicted. Since prediction is possible, a designer should be able to avoid quenching through proper choice of gyro parameters.

Finally, the time modulated rebalance technique offers greater flexibility in adjusting gyro loop transfer characteristics.

4.1 ANALYSIS OF THE LIMIT CYCLING BINARY GYRO

This section discusses analytic techniques for deriving the closed loop transfer characteristics of the binary pulse torqued gyro loop. Gyros with second order dynamics and those with significant compliance between rotor and gimbal are considered in separate sections. Closed loop gain characteristics predicted analytically are displayed to illustrate the effects of different instrument parameters.



- H = Rotor Angular Momentum
- C = Float Damping Coefficient
- i_{tg} = Torquer Current

Figure 4.1-1 Binary-Torqued Gyro Loop with Second Order Gyro Dynamics

4.1.1 Simple Gyro Dynamics

Figure 4.1-1 illustrates a simple representation of a binary pulse rebalanced gyro loop. The rotor and gimbal are assumed to behave as a single rigid body for angular motion about the gyro output axis. When sampling is ignored, the response of the gyro loop illustrated to oscillatory

inputs closely approximates that of a linear second order system with damping ratio and natural frequency given by (Section 2.4, Ref. 1):

$$\zeta = \sqrt{\frac{1}{2\tau_f} \left(\frac{\tau_f \tau_{tg}}{\tau_f + \tau_{tg}} \right)} \quad (4.1-1)$$

$$\omega_n = \sqrt{\frac{1}{2\tau_f} \left(\frac{\tau_f + \tau_{tg}}{\tau_f \tau_{tg}} \right)} \quad (4.1-2)$$

The linearization of the binary gyro loop is a consequence of the limit cycle usually found in a system of this type. Under certain circumstances (discussed in Appendix D) an oscillatory input to the gyro loop can cause the limit cycle to vanish. In that case, the closed loop characteristics of the binary torqued instrument differ significantly from those presented above. When the limit cycle is not quenched, Eqs. (4.1-1) and (4.1-2) can be used to study the effect of varying gyro parameters. Figure 4.1-2 illustrates the behavior of the closed loop gain as the float time constant is varied. A similar comparison could be made of phase shift. Changes in τ_f are easily made by varying the float damping coefficient, C.

Effects of Sampling in the Gyro Loop - In the above discussion the effect of sampling in the loop has been ignored for the sake of simplicity. The sample and hold operation contributes an additional frequency-sensitive phase lag to the open loop dynamics. This can cause the limit cycle frequency and amplitude to be different from those experienced in a continuous binary gyro loop. Consequently, there is a different value for the nonlinearity gain to the signal and the closed loop frequency response is not the same.

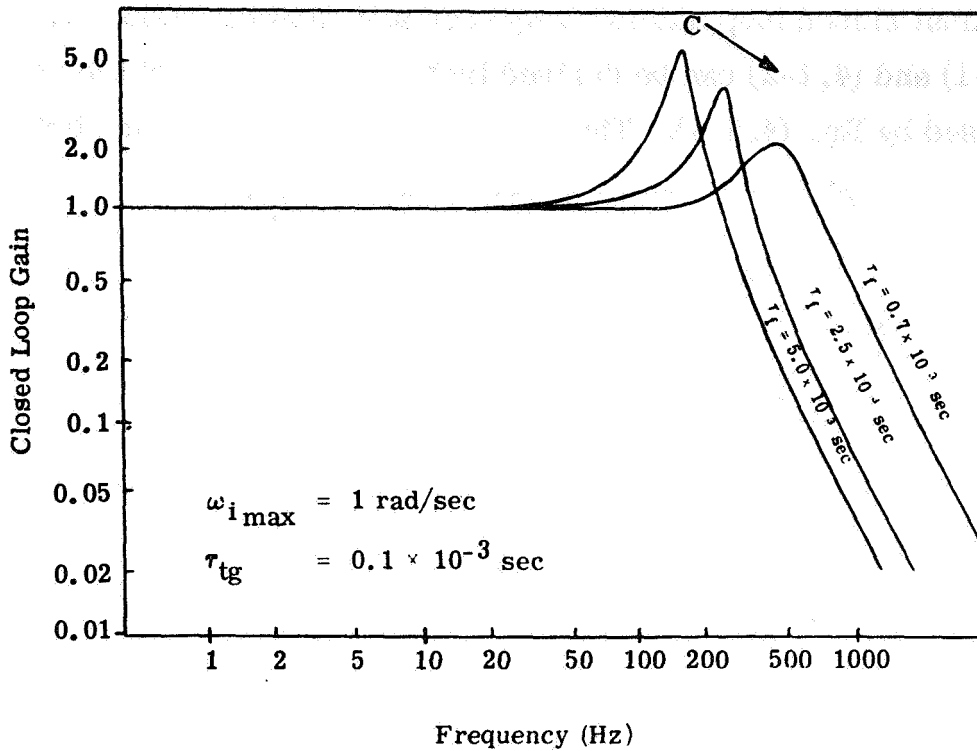


Figure 4.1-2 Closed Loop Frequency Response as a Function of Float Time Constant

The sample and hold transfer function is

$$S(j\nu) = e^{-j \nu T/2} \frac{\sin \frac{\nu T}{2}}{\frac{\nu T}{2}} \quad (4.1-3)$$

where T is the sampler period in seconds. If $\nu T/2 \ll 1$ because the sampler frequency is much higher than other frequencies encountered in the loop, the transfer function is approximately

$$S(j\nu) \approx \frac{1}{1 + j \frac{\nu T}{2}} \quad (4.1-4)$$

The equivalent closed loop natural frequency and damping ratio given in Eqs. (4.1-1) and (4.1-2) can be derived including the effect of the sampler lag expressed by Eq. (4.1-4). The resulting relations are given below.

$$\omega_n = \sqrt{\left(\frac{\tau_f + \tau_{tg}}{2\tau_f}\right) \left(\frac{\tau_f \tau_{tg} + \frac{T}{2}(\tau_f + \tau_{tg}) + \left(\frac{T}{2}\right)^2}{\left(\tau_f \tau_{tg} + \frac{T}{2}(\tau_f + \tau_{tg})\right)^2}\right)} \quad (4.1-5)$$

$$\zeta = \sqrt{\left(\frac{1}{2\tau_f(\tau_f + \tau_{tg})}\right) \left(\frac{\left(\tau_f \tau_{tg} + \frac{T}{2}(\tau_f + \tau_{tg})\right)^2}{\tau_f \tau_{tg} + \frac{T}{2}(\tau_f + \tau_{tg}) + \left(\frac{T}{2}\right)^2}\right)} \quad (4.1-6)$$

The effect of a finite sampling rate on the closed loop gain is illustrated in Fig. 4.1-3 where response curves are shown for a very high sampling frequency and a 10 kc rate. It can be seen that sampling in the gyro loop tends to reduce the useful bandwidth of the instrument.

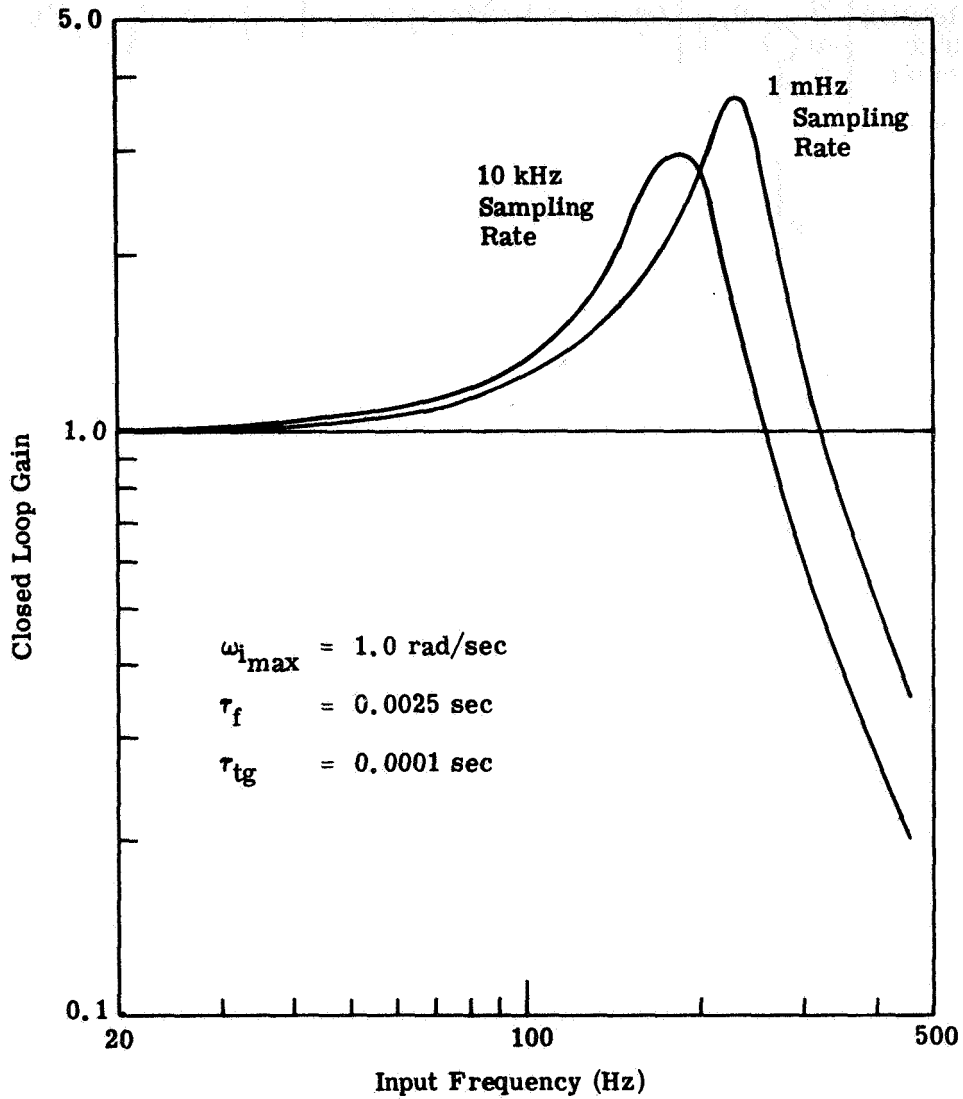


Figure 4.1-3 Closed Loop Frequency Response Showing the Effect of Sampling

4.1.2 Gyro Dynamics with Rotor Bearing Compliance

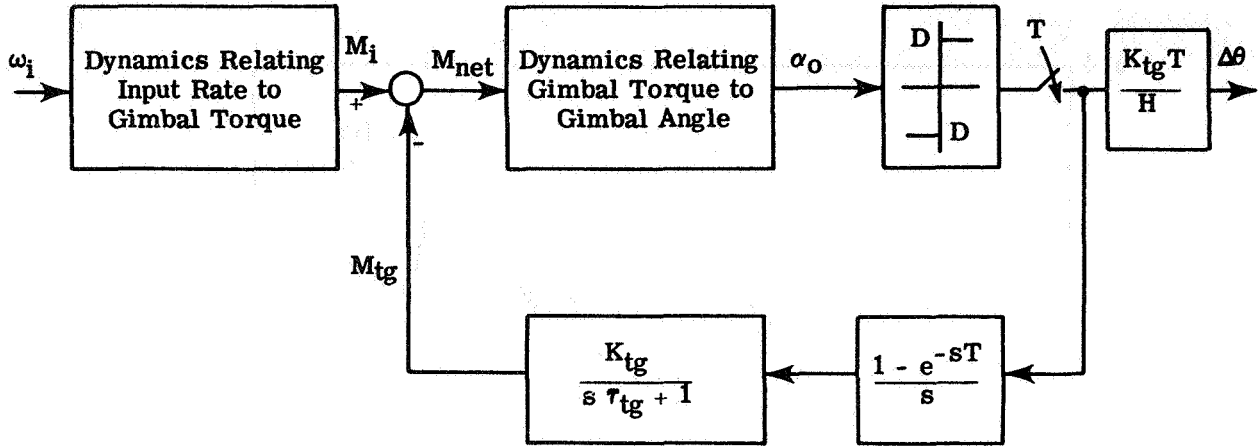


Figure 4.1-4 Binary-Torqued Gyro Loop when Rotor Bearing Compliance is Considered

The binary-torqued gyro loop with significant rotor-to-gimbal compliance is in many respects similar to that discussed in Section 4.1.1. The difference lies in the transfer functions relating torque on the float to input angular rate, and float angle to torque (see Fig. 4.1-4). When linear rotor bearing compliance is present, the transfer functions become

$$\frac{M_i}{\omega_i}(s) = -H \left(\frac{4\rho^2\nu_n^2s^2 + 4\rho\nu_n^3s + \nu_n^4}{s^4 + 4\rho\nu_n s^3 + (2\nu_n^2(1+2\rho^2) + \omega_g^2)s^2 + 4\rho\nu_n^2s + \nu_n^4} \right) \quad (4.1-7)$$

$$\frac{\alpha_o}{M_{net}}(s) = \frac{1}{sI_{00g}} \left(\frac{s^4 + 4\rho\nu_n s^3 + (2\nu_n^2(1+2\rho^2) + \omega_g^2)s^2 + 4\rho\nu_n^3s + \nu_n^4}{s^5 + C_4s^4 + C_3s^3 + C_2s^2 + C_1s + C_0} \right) \quad (4.1-8)$$

where

$$C_4 \triangleq 4\rho\nu_n + \frac{d}{I_{00g}} + \frac{1}{\tau_f}$$

$$C_3 \triangleq 2\nu_n^2 (2\rho^2 + 1) + \omega_g^2 + \frac{4\rho\nu_n}{\tau_f} + \frac{k}{I_{00g}} + \frac{2\rho\nu_n d}{I_{00g}}$$

$$C_2 \triangleq 4\rho\nu_n^3 + \frac{\omega_g^2}{\tau_f} + \frac{2\nu_n^2 (2\rho^2 + 1)}{\tau_f} + \frac{2\rho\nu_n k}{I_{00g}} + \frac{d}{I_{00g}} (\nu_n^2 + \omega_g^2)$$

$$C_1 \triangleq \nu_n^4 + \frac{4\rho\nu_n^3}{\tau_f} + \frac{k}{I_{00g}} (\nu_n^2 + \omega_g^2)$$

$$C_0 \triangleq \frac{\nu_n^4}{\tau_f}$$

$$\omega_g \triangleq \frac{H}{I_r}$$

These relations are derived in Appendix I. If the coupling between the wheel and gimbal is represented by a linear second order system, ρ and ν_n are the damping ratio and natural frequency of this system. They are computed from the stiffness between the rotor and gimbal, k , a damping coefficient, d , and the rotor moment of inertia about input and output axes, I_r .

$$\rho \triangleq \frac{d}{2\sqrt{I_r k}} \quad (4.1-9)$$

$$\nu_n \triangleq \sqrt{\frac{k}{I_r}} \quad (4.1-10)$$

The float time constant τ_f is computed by considering only the gimbal moment of inertia about the output axis and output axis damping:

$$\tau_f \triangleq \frac{I_{oog}}{C} \quad (4.1-11)$$

Since only the linear parts of the loop are changed as a result of considering compliance, many of the phenomena seen for simple gyro dynamics are again observed. As in Section 4.1.1, the effect of the sample and hold operation is neglected until later in this discussion. Due to the absence of any phase shift contribution from the nonlinearity, the loop still limit cycles at a frequency determined only by the phase characteristics of the linear part of the open loop. As before, the limit cycle "linearizes" the nonlinearity with respect to a signal circulating in the loop. Unfortunately, the closed loop signal transfer characteristic can no longer be approximated by that of a second order system.

The limit cycle analysis of the loop under discussion is more difficult than when simple gyro dynamics are considered. Here, the linear open loop transfer function $H(s)$ has seven poles, instead of three.

$$H(s) = \frac{K_{tg}}{s\tau_{tg} + 1} \left(\frac{\alpha_o}{M_{net}} \right) K_{sg} \quad (4.1-12)$$

$$H(s) = \frac{K_{sg}K_{tg}}{I_{og}} \frac{1}{s} \frac{(s^4 + 4\rho\nu_n s^3 + (2\nu_n^2(2\rho^2 + 1) + \omega_g^2)s^2 + 4\rho\nu_n^3 s + \nu_n^4)}{\left[\tau_{tg}s^6 + (1 + C_4\tau_{tg})s^5 + (C_4 + C_3\tau_{tg})s^4 + (C_3 + C_2\tau_{tg})s^3 \right. \\ \left. + (C_2 + C_1\tau_{tg})s^2 + (C_1 + C_0\tau_{tg})s + C_0 \right]} \quad (4.1-13)$$

where C_4 , C_3 , C_2 , C_1 and C_0 are defined above. It is observed that the phase condition for a limit cycle, $\angle H(j\omega) = -180^\circ$, occurs at several frequencies. The limit cycle frequencies can be computed numerically as the positive real root(s) of a polynomial which is derived from this constraint.

$$\gamma_{10}\omega^{10} + \gamma_8\omega^8 + \gamma_6\omega^6 + \gamma_4\omega^4 + \gamma_2\omega^2 + \gamma_0 = 0 \quad (4.1-14)$$

where

$$\gamma_0 \triangleq EC_0$$

$$\gamma_2 \triangleq (DC_0 - EC_1)\tau_{tg} + DC_1 - EC_2 - CC_0$$

$$\gamma_4 \triangleq (CC_1 + EC_3 - BC_0 - DC_2)\tau_{tg} + EC_4 + CC_2 + C_0 - DC_3 - BC_1$$

$$\gamma_6 \triangleq (BC_2 + DC_4 - C_1 - CC_3 - E)\tau_{tg} + D + BC_3 - CC_4 - C_2$$

$$\gamma_8 \triangleq (C + C_3 - BC_4)\tau_{tg} + C_4 - B$$

$$\gamma_{10} \triangleq -\tau_{tg}$$

$$B \triangleq 4\rho\nu_n$$

$$C \triangleq 2\nu_n^2(2\rho^2 + 1) + \omega_g^2$$

$$D \triangleq 4\rho\nu_n^3$$

$$E \triangleq \nu_n^4$$

In general, there can be as many as five positive, real solutions to Eq. (4.1-14), each corresponding to a different "crossover frequency" where the linear, open loop phase lag is 180° . Stability analyses are applied to discard certain solutions of Eq. (4.1-14). In general, if the five solutions are ordered by ascending frequency ($\omega_{l1}, \omega_{l2}, \dots, \omega_{l5}$), the stable limit cycles correspond to the frequencies with odd numbered subscripts ($\omega_{l1}, \omega_{l3}, \omega_{l5}$).

For each stable limit cycle there is a different limit cycle amplitude, corresponding to a different gain, N_B , of the nonlinearity to signal inputs. Because the closed loop frequency response to an input depends on N_B there can be as many as three different sets of transfer characteristics, each resulting from a different limit cycle. Figure 4.1-5 shows two closed-loop gain responses obtained for a system with two stable limit cycle modes ($\omega_l = 727 \text{ Hz}, 868 \text{ Hz}$). Although the limit cycle frequencies differ significantly, the two responses are quite similar. Appendix G discusses the fact that exciting the gyro loop with a particular input at certain frequencies can cause the limit cycle to change, with a resultant shift to a different frequency response. The system whose closed loop is shown in Fig. 4.1-5 can be shifted from the 727 Hz limit cycle mode to the 868 Hz mode by excitation with a 0.1 rad/sec amplitude angular rate input at 810 Hz or above. However, it cannot be shifted back to the 727 Hz mode in a corresponding manner.

Two effects - finite sampling frequency and limit cycle quenching - remain to be discussed in connection with binary loops containing rotor-to-gimbal compliance. It was shown in Section 4.1.1, that the sample and hold operation introduces a lag which can be approximated by the transfer function $1/(1 + j\nu T/2)$ where T is the sampler period. This causes a modification of the limit cycle frequency and amplitude, changing the nonlinearity gain to the signal and altering the closed loop response.

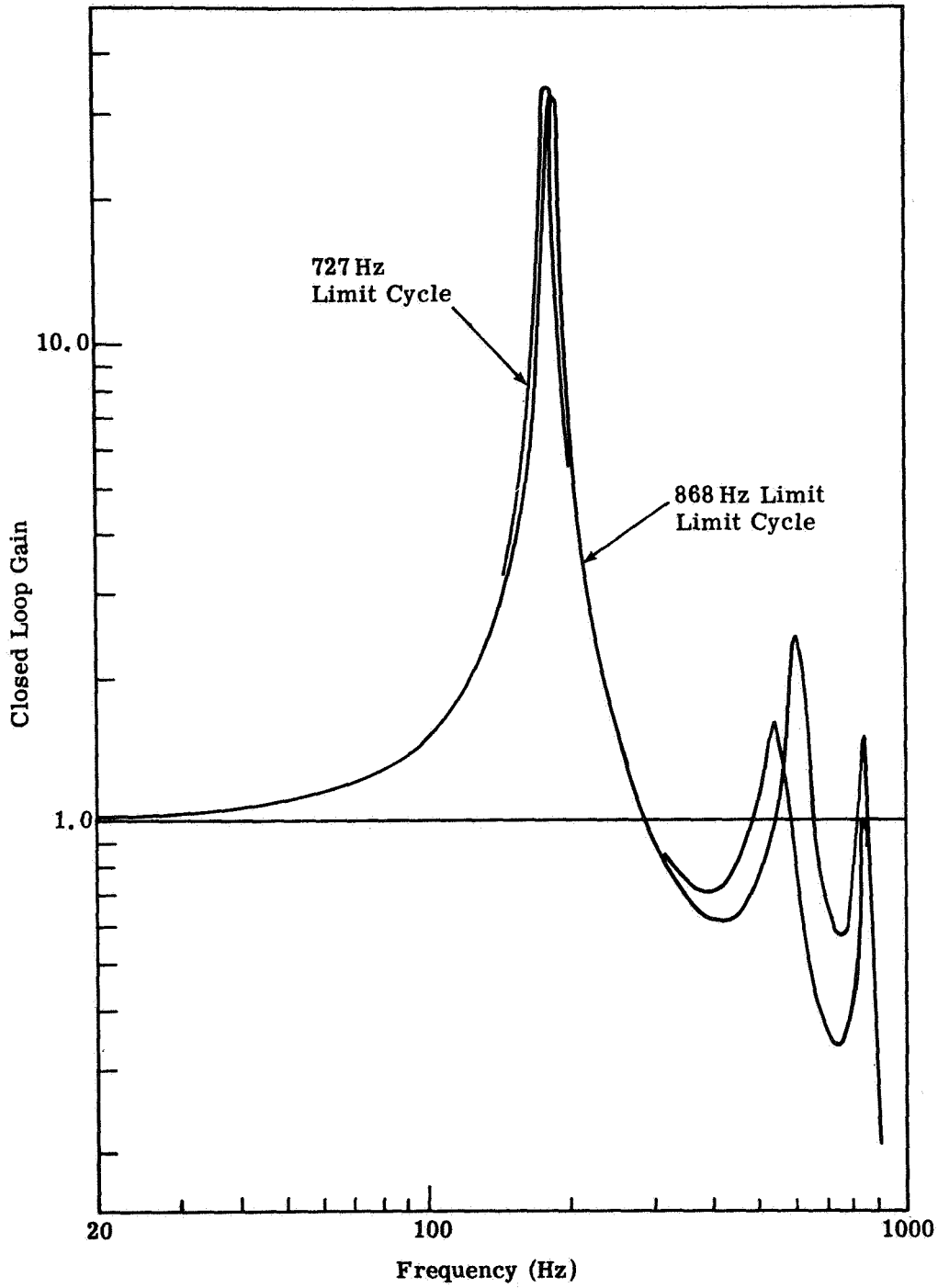


Figure 4.1-5 Potential Frequency Responses of System with Two Stable Limit Cycles

The effect of sampling on a gyro with significant compliance between rotor and gimbal is illustrated in Fig. 4.1-6. Two analytically determined frequency response curves are shown; one for a high sampling frequency ($T \cong 0$) and the other for a 10kHz rate. Limit cycle quenching and its effect on the performance of the gyro loop discussed in this section are treated in Appendix D.

4.2 SIMULATION OF THE LIMIT CYCLING BINARY GYRO

The analyses of Section 4.1 provide interesting insights into the closed loop behavior of the binary torqued gyro. The accuracy of these predictions depends on how well the describing function linearization characterizes the true nonlinearity response to a signal in the presence of a limit cycle. As a check on this approach, typical gyro loops were analyzed by the methods discussed in Section 4.1 and were then simulated on an analog computer to verify the gyro transfer characteristics predicted analytically.

4.2.1 Simple Gyro Dynamics

A binary gyro loop was examined analytically and by analog simulation. The dynamic characteristics of the linear portion of the gyro were identical with those presented in Fig. 4.1-1. Details of the simulation are given in Appendix F. The important gyro parameters for this comparison are:

$$\begin{aligned} H &= 2 \times 10^5 \text{ dyne-cm-sec} \\ \omega_i \text{ max} &= 1 \text{ rad/sec} \\ \tau_f &= 0.0025 \text{ sec} \\ \tau_{tg} &= 0.0001 \text{ sec} \end{aligned}$$

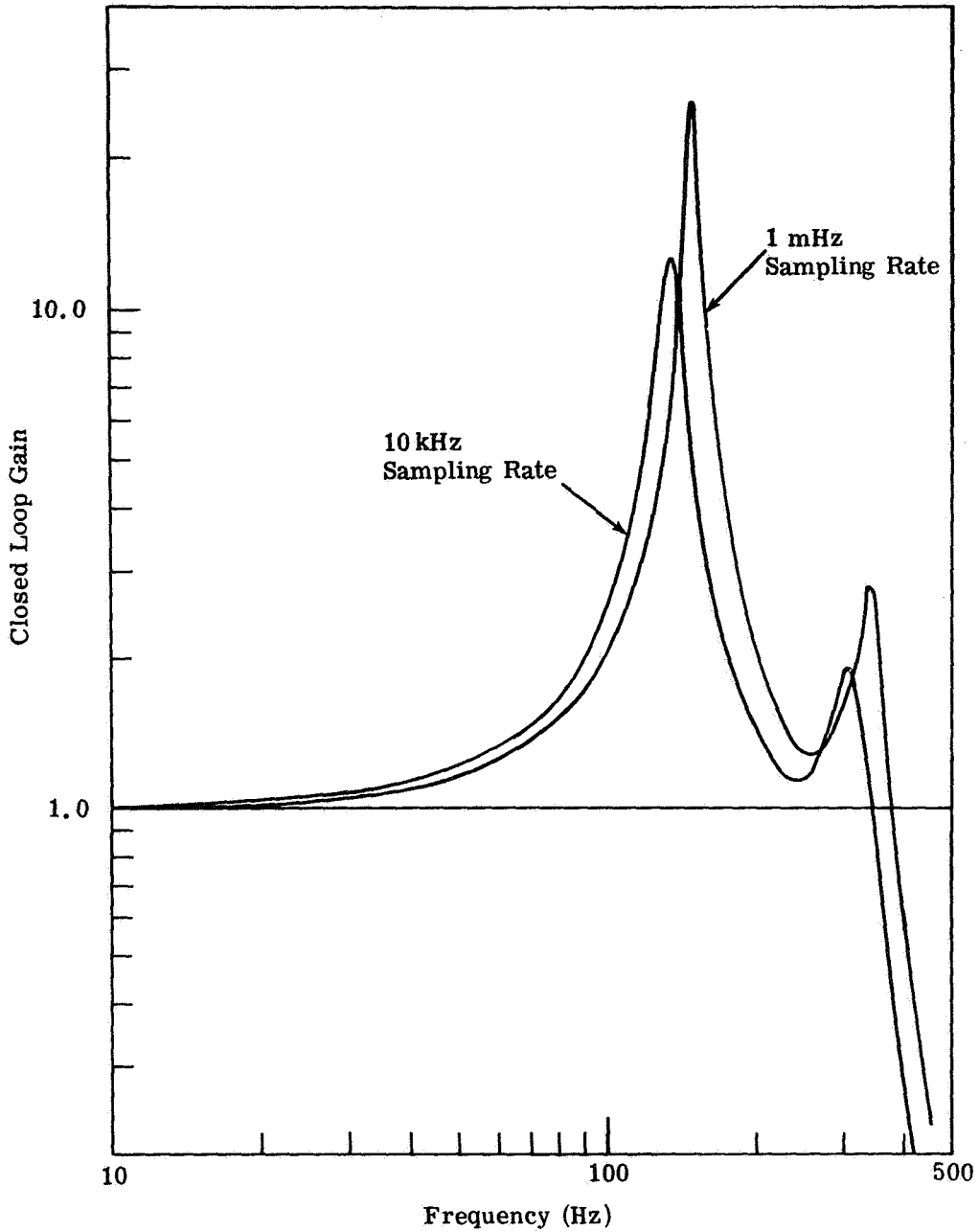
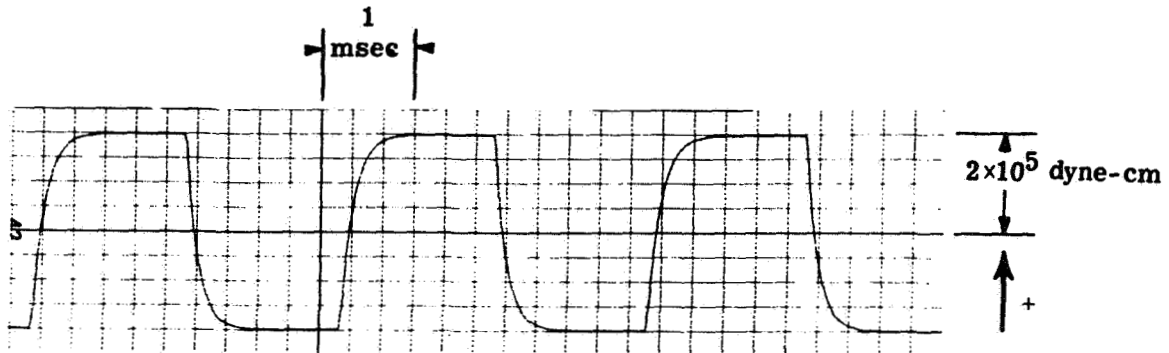
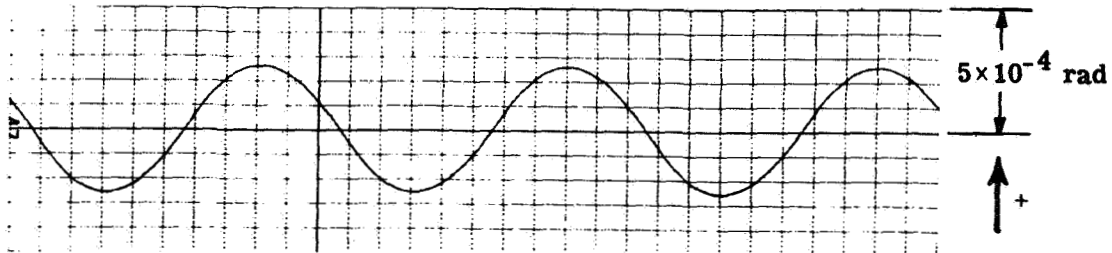


Figure 4.1-6 Effect of Sampling Rate on Gyro Frequency Response: Significant Rotor Bearing Compliance

Figure 4.2-1 displays simulation records of the binary gyro float angle and torquer output in the absence of an input angular rate. A very high sampling rate (1 MHz) was used. The limit cycle observed was in close agreement with that predicted for a continuous loop.



(a) Torquer Output, M_{tg}

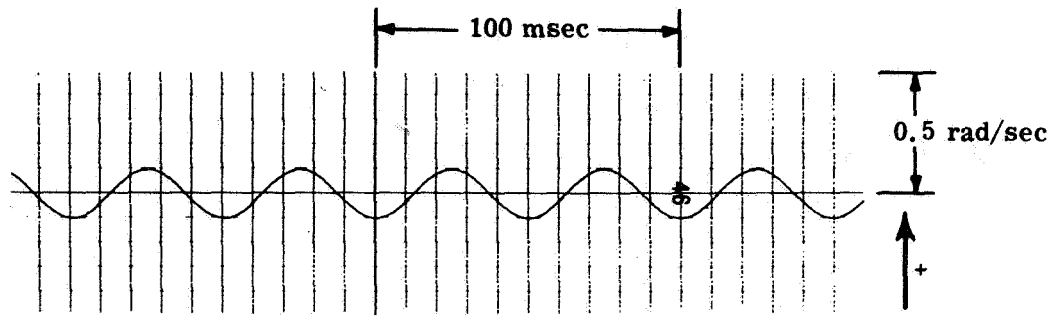


(b) Float Angle, α_0

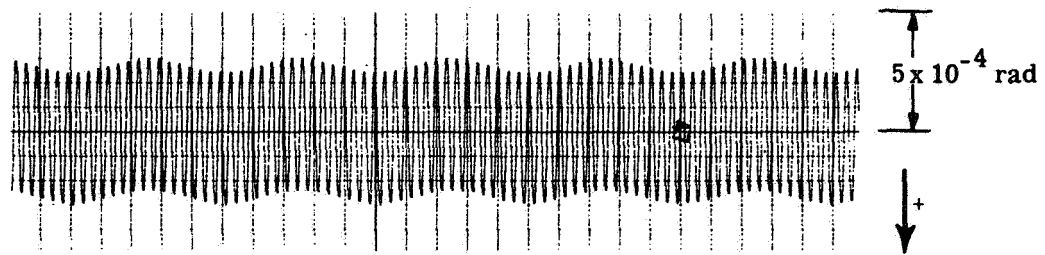
Figure 4.2-1 Simulation Records for Limit-Cycling Binary Gyro

An oscillatory angular rate with a peak amplitude of 0.1 rad/sec was applied to the gyro loop. Figure 4.2-2 and 4.2-3 display simulation records of gyro input, float angle and torquer output for two values of input frequency. Again, an essentially continuous loop was considered. It can be seen that for a low frequency input the gyro float angle follows the input very closely, despite the simultaneous presence of a limit cycle oscillation. At a higher input frequency, however, it is more difficult to identify signal and limit cycle effects separately. The closed loop frequency response predicted analytically for this system is seen in Fig. 4.2-4, together with points obtained by simulation. There is a good agreement between the two techniques.

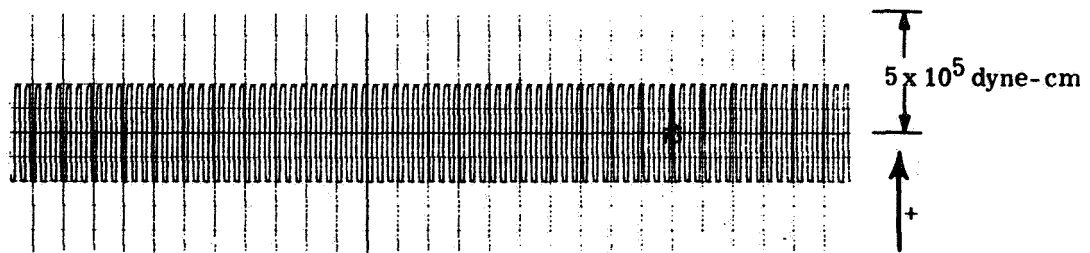
Figure D-2 of Appendix D indicates that, for an input amplitude of 0.1 rad/sec, the limit cycle seen in this system is quenched over a range of frequencies above 200 Hz. Accordingly, the analytically derived response has been corrected over this frequency range to show a flat-topped peak characteristic of the binary system when the limit cycle is quenched. In this region the system output is a square wave at the input frequency with amplitude equal to the nonlinearity drive level. This level is equivalent to 1 rad/sec input rate and the fundamental component of the output has an amplitude of $4/\pi = 1.273$ rad/sec. Since the input amplitude is 0.1 rad/sec, gain of the closed loop is a constant value of 12.73. Moreover, all information about the input signal amplitude (except that it is large enough to extinguish the limit cycle) is lost, and the gyro loop ceases to function as a linear system. Limit cycle quenching can represent a definite restriction on the range of the amplitudes and frequencies that can be accurately detected by a binary gyro. However, quenching is not common at frequencies well below that of the limit cycle.



(a) Input Angular Rate, ω_1



(b) Float Angle, α_0



(c) Torquer Output

Figure 4.2-2 Binary Gyro Simulation: 20 Hz Input

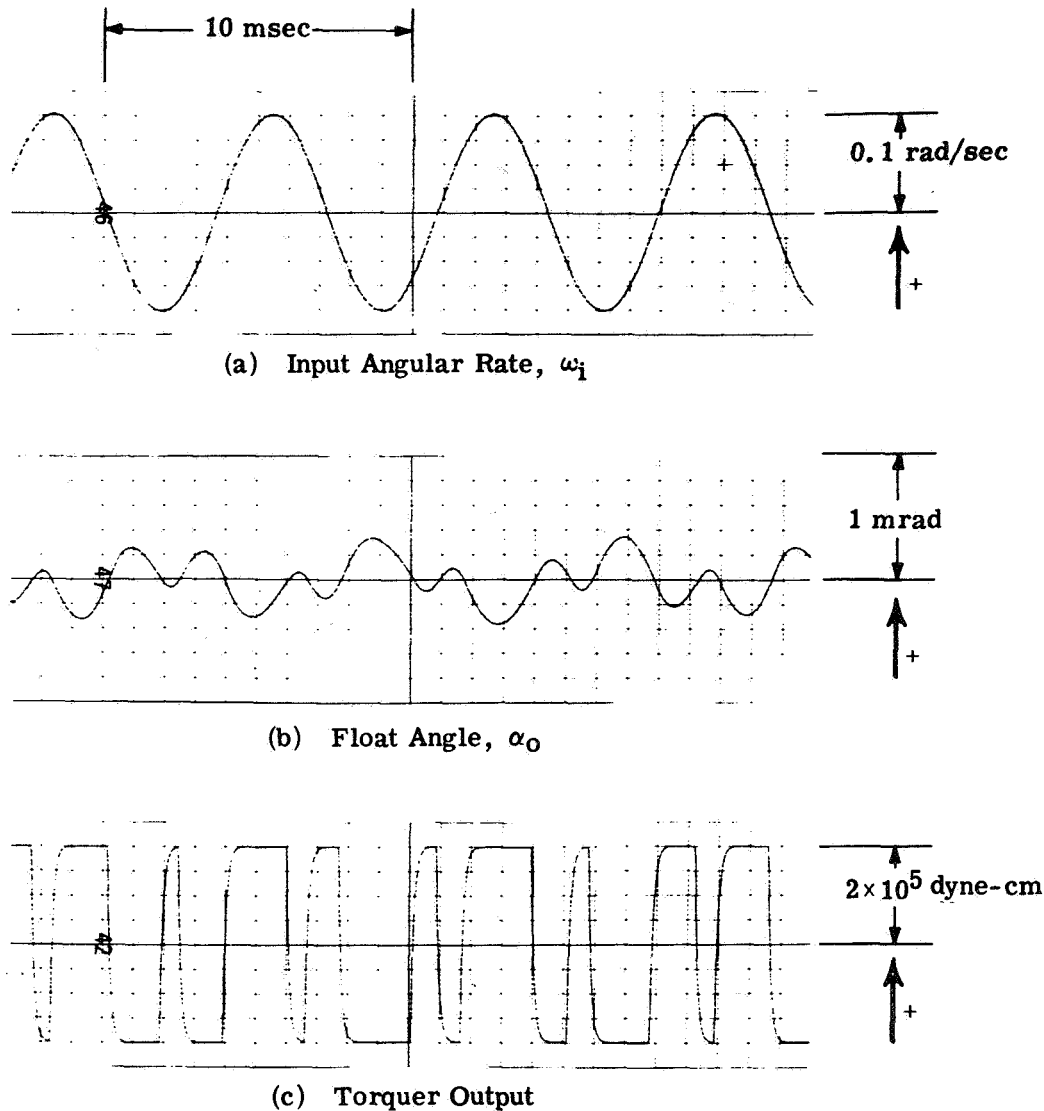


Figure 4.2-3 Binary Gyro Simulation: 165 Hz Input

Sampling - Simulations were also conducted for the binary limit cycling gyro with significant sampling lags. Figure 4.2-5 shows the frequency response for a loop with 10^4 samples per second. It differs noticeably from that shown in Fig. 4.2-4. The solid line indicates the response computed using describing function theory and simulation points obtained are also shown. Good agreement between analysis and simulation is indicated.

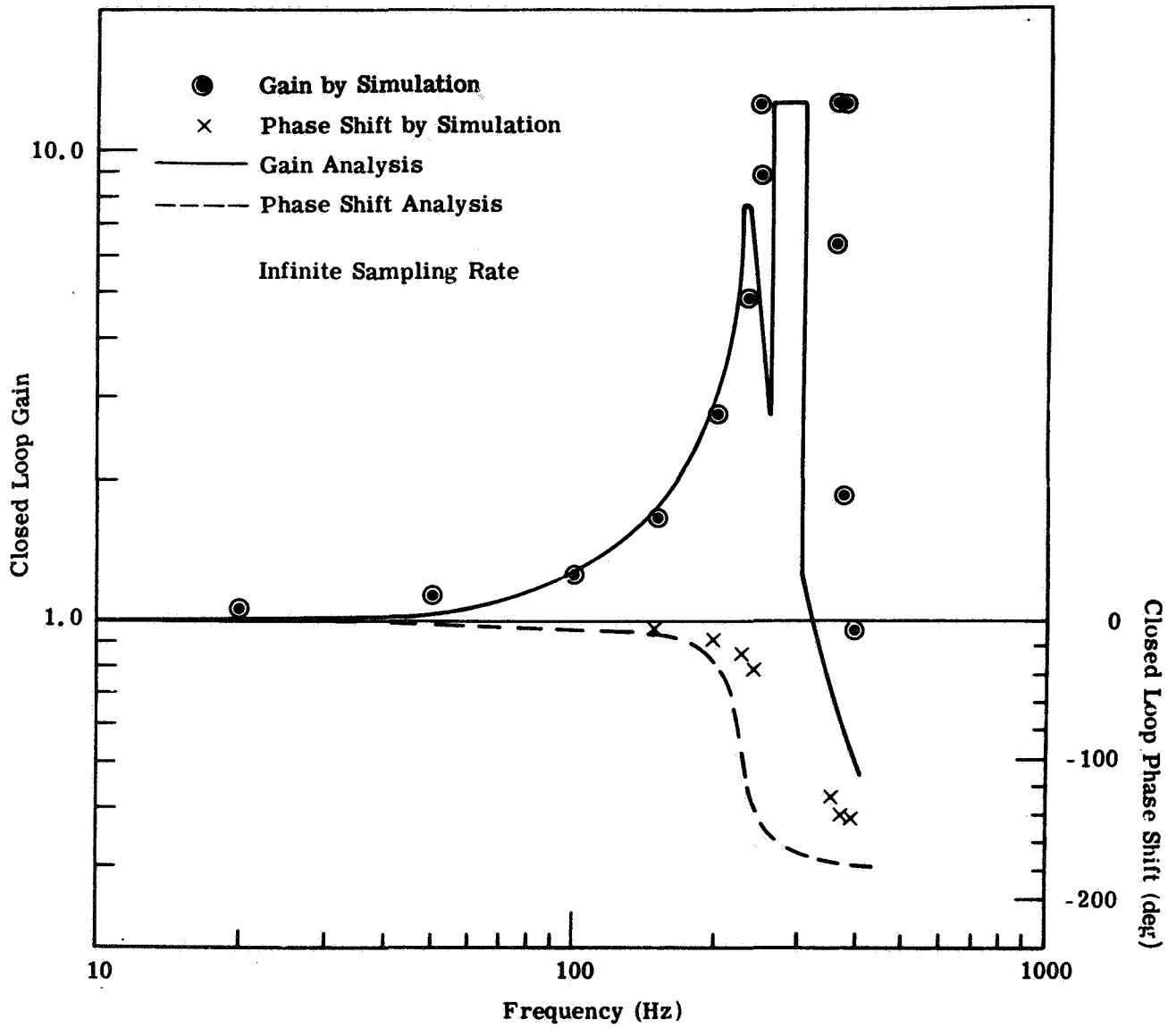


Figure 4.2-4 Frequency Response of a Limit Cycling Binary Gyro: Comparison of Analytic and Simulation Results

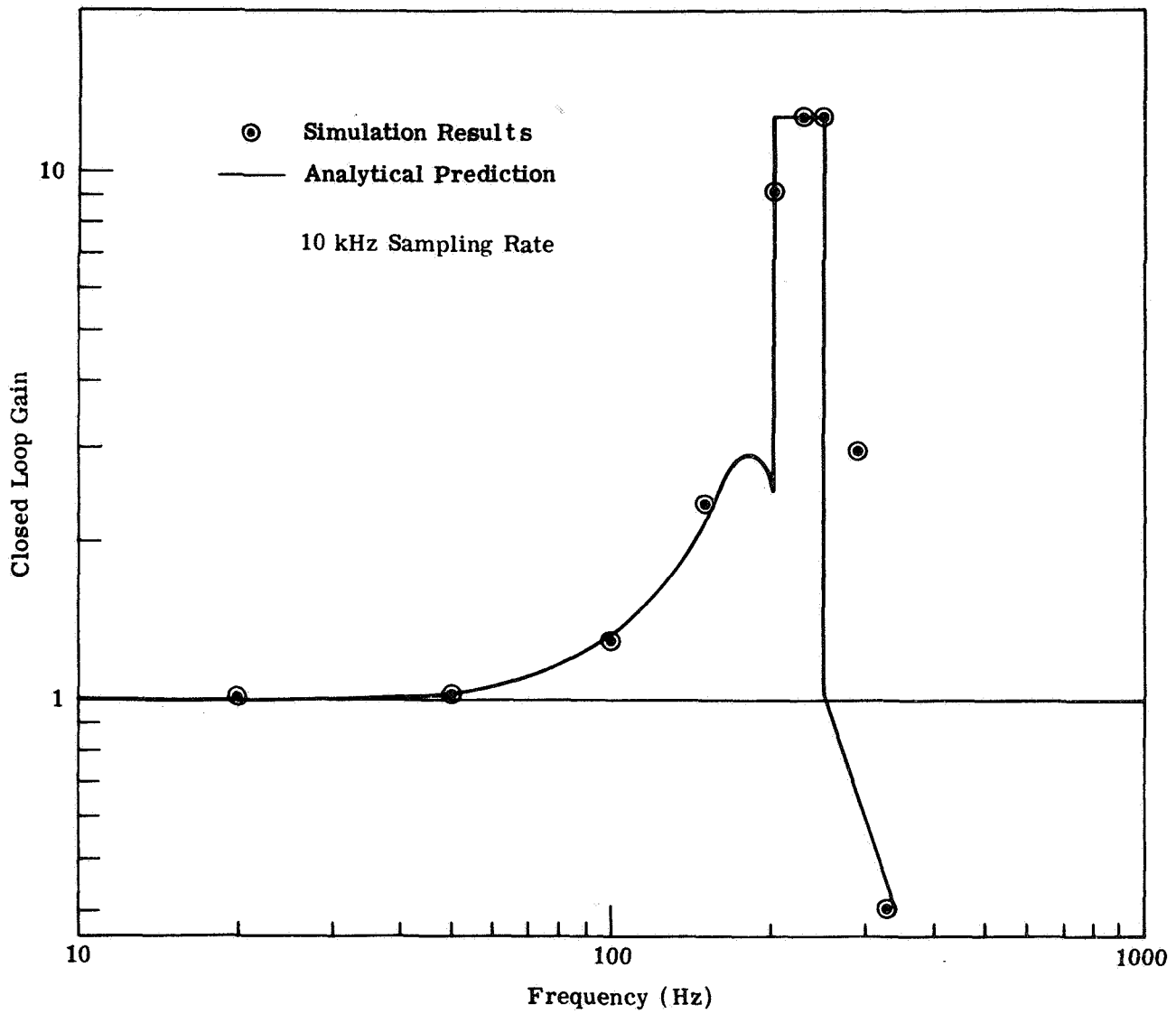


Figure 4.2-5 Frequency Response of a Limit Cycling Binary Gyro: Comparison of Analytic and Simulation Results

4.2.2 Gyro Dynamics with Rotor Bearing Compliance

Section 4.1.2 discusses the changes made to the gyro model when rotor-to-gimbal compliance is assumed to be significant. For the purpose of comparing analytic and simulation results, the following set of gyro parameters was employed:

$$\begin{aligned}\omega_g &= 4000 \text{ rad/sec} \\ \nu_n &= 2512 \text{ rad/sec} \\ \rho &= 0.02\end{aligned}$$

The frequency response predicted analytically for this system is shown in Fig. 4.2-6, along with points obtained by simulation. Good agreement is observed between the two methods except near the frequencies at which limit cycle quenching takes place. A small hysteresis region, not predicted by the analysis, is observed in the simulation for input frequencies near the first (low frequency) quenching region. The other quenching region, occurring at frequencies near that of the limit cycle, is not accurately described by the analysis. This error in determining quenching is thought to be caused by beat frequency terms not considered in the describing function approach used. It can be seen from the figure that the analysis provides adequate estimates of the general frequency range for quenching and gives an excellent prediction of the low frequency portion of the gyro loop response. Comparison of Figs. 4.2-4 and 4.2-6 indicates that, for the parameters chosen, rotor bearing compliance reduces the useful bandwidth of the gyro. Since the low frequency peak in Fig. 4.2-6 is caused by the compliance, greater bearing stiffness would help to alleviate this effect.

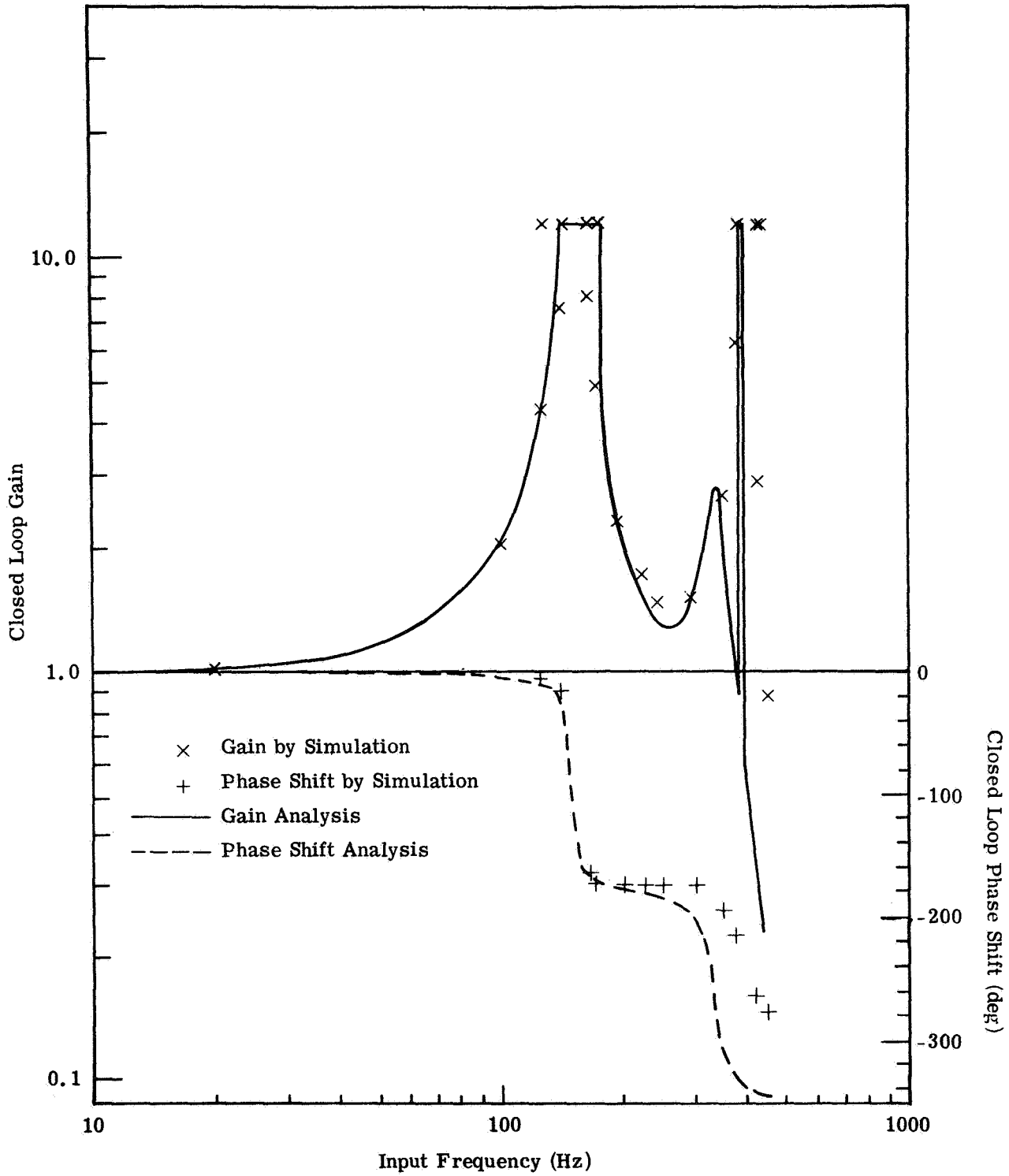


Figure 4.2-6 Frequency Response of a Binary Gyro with Rotor Bearing Compliance: Comparison of Analytic and Simulation Results

4.3 COMPENSATION FOR THE LIMIT CYCLING BINARY GYRO

Introduction - The binary gyro loop limit cycles whether or not a rate signal is present at the input (unless the signal is of high enough amplitude or suitably shaped to quench the limit cycle). As a consequence of the limit cycling property, the closed loop frequency response to an input signal is largely determined by gyro and torquer time constants and not by easily manipulated electrical gains (see Section 4.1.1). Specifically, if the loop is linearized using describing function techniques, a response characteristic approximately that of a second order system can result with natural frequency and damping ratio given by Eqs. (4.1-1) and (4.1-2). These frequency response characteristics cannot be changed without making hardware modifications to change τ_f and τ_{tg} . In general, τ_{tg} is made as small as possible in order to permit high sampling rates. Also the float time constant is related to gyro noise effects through the damping coefficient, C . Raising the damping reduces gyro resolution and increases the effect of electrical noise in the pickoff. In addition, no reasonable choice of the time constants can make the damping ratio greater than 1/2. Thus, the frequency response is forced to have a peak near the natural frequency. Clearly, some frequency sensitive compensation may be desired to remove this peak and, more generally, to permit control of the frequency response characteristics without changing τ_f and τ_{tg} .

Analysis - Following the approach used to obtain Eqs. (4.1-1) and (4.1-2), we represent the effective gain of the binary nonlinearity to a sinusoidal signal by the Two Sinusoid Input Describing Function (TSIDF), written $N_B(A, B)$. This describing function is the ratio of the amplitude of the signal-frequency harmonic at the nonlinearity output to the amplitude B of the signal at the nonlinearity input when a sinusoid (limit cycle) of amplitude A is also present at the input. If B is considered small compared to A , a simplified form for $N_B(A, B)$ results:

$$N_B(A, B) \cong N_B(A, 0) \quad B \ll A \quad (4.3-1)$$

$$\cong \frac{2D}{\pi A}$$

where D is the drive level of the nonlinearity. Appendix C examines in greater detail the conditions under which this approximation holds.

In attempting to compensate the limit cycling binary loop, we must consider the effect of the limit cycle on the total open loop gain and phase performance as seen by the signal sinusoid. The binary nonlinearity TSIDF gain to the limit cycle, written $N_A(A, B)$, is given by

$$N_A(A, B) \cong \frac{4D}{\pi A}; \quad B \ll A \quad (4.3-2)$$

The complex open loop transfer function of the linear part of the loop is written $H(j\omega)$. The definition of the limit cycle requires that, at the limit cycle frequency, ω_l ,

$$H(j\omega_l) N_A(A, B) = 1 \angle -180^\circ \quad (4.3-3)$$

The limit cycle amplitude A and frequency ω_l adapt to maintain this equality regardless of the compensation introduced. From Eqs. (4.3-1) and (4.3-2), it can be seen that

$$N_A(A, B) \cong 2N_B(A, B); \quad B \ll A \quad (4.3-4)$$

Substituting for N_A in Eq. (4.3-3) yields

$$H(j\omega_l) N_B(A, B) = \frac{1}{2} \angle -180^\circ \quad (4.3-5)$$

Here, $H(j\omega_l) N_B(A, B)$ is the expression for the complex open loop gain as seen by the signal sinusoid. We conclude that, due to the adaptive properties of the limit cycle amplitude and frequency, the open loop gain and phase shift as seen by the signal sinusoid will always be $1/2 \angle -180^\circ$ at ω_l . The linear analysis technique used to investigate in-loop compensation of binary pulse torqued gyros makes use of the rectangular gain-phase plot (Nichols chart). The open loop gain and phase characteristics are plotted as a function of frequency. On the same plot, lines of constant M (closed loop amplitude ratio) are constructed. The closed loop amplitude ratio for any sinusoidal input is the value of M intersected by the open loop gain-phase curve at the same frequency. The $M = 1$ line represents the desired unity closed loop gain. Figure 4.3-1 shows the $M = 1$ line and the open loop gain-phase curve of the uncompensated gyro loop with the following parameters:

$$\begin{aligned} \tau_g &= 10^{-4} \text{ sec} \\ \tau_f &= 2.5 \times 10^{-3} \text{ sec} \end{aligned}$$

Note that the gain-phase curve cuts through high closed loop gain lines at frequencies lower than ω_l , producing a peaked frequency response.

In Section 4.1 torquer lag was neglected to allow approximation of the uncompensated binary gyro loop by a second order linear system. This representation of the gyro is adequate for computing closed loop gain and phase shift characteristics at low frequencies. However, the torquer begins to contribute open loop phase shift at frequencies below the limit cycle, causing a significant difference between the open loop gain-phase plots of the approximate (second order) and more complete gyro models. Consequently, the peak closed loop gain calculated using a second order approximation to the gyro loop is always less than the true value.

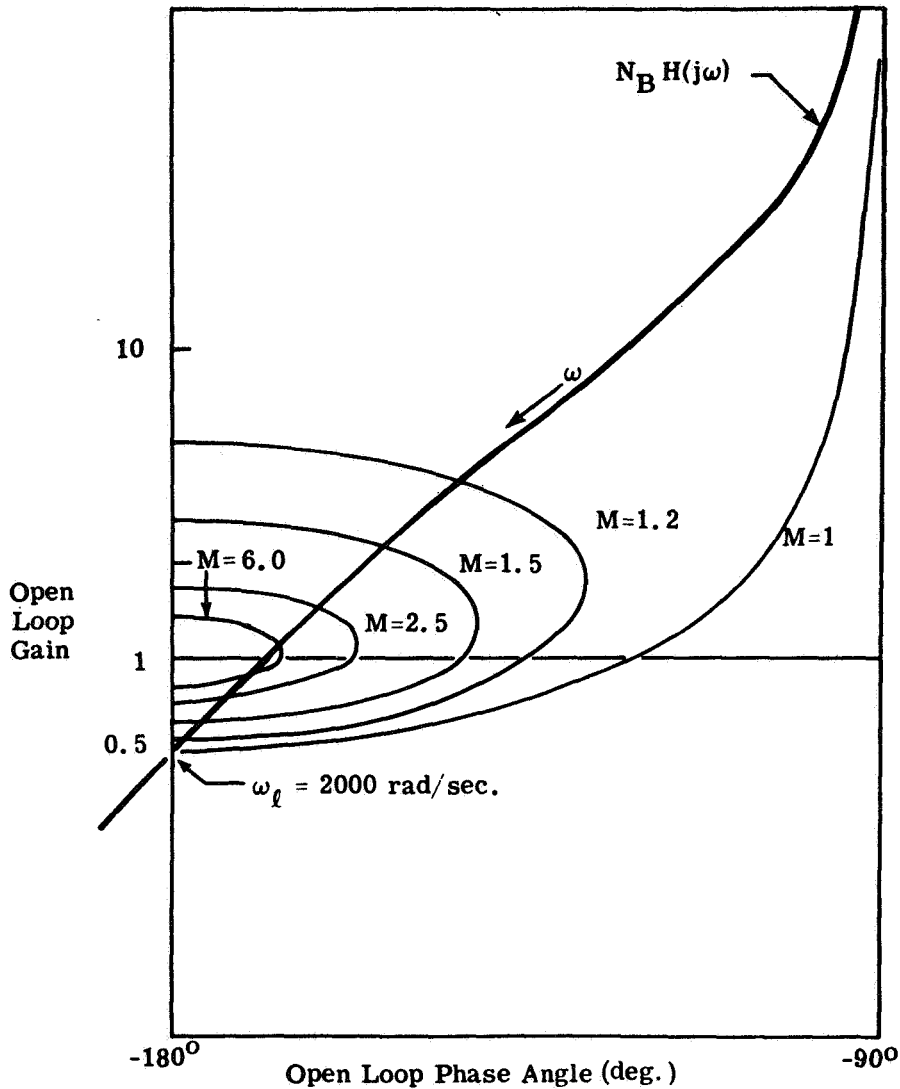


Figure 4.3-1 Open Loop Gain-Phase Plot for Uncompensated Binary Gyro

In order to obtain unity closed loop gain at all frequencies below the limit cycle, we must make gain and phase changes to the open loop which cause the compensated gain-phase curve to coincide with the $M=1$ line. As discussed earlier, the complex open loop gain must always be $1/2 \angle -180^\circ$ at the limit cycle frequency, ω_ℓ ; the gain-phase curve always

crosses the -180° phase shift line with a gain of $1/2$ at ω_g whether or not compensation is used. It can be seen from Fig. 4.3-1 that the $M=1$ line also intersects the -180° line at $1/2$. Four sets of linear dynamic compensation schemes are discussed below. In each case the compensation is assumed to be placed in the forward signal path as illustrated in Fig. 4.3-2. The closed loop gains for gyros employing various compensation schemes are shown in Fig. 4.3-3.

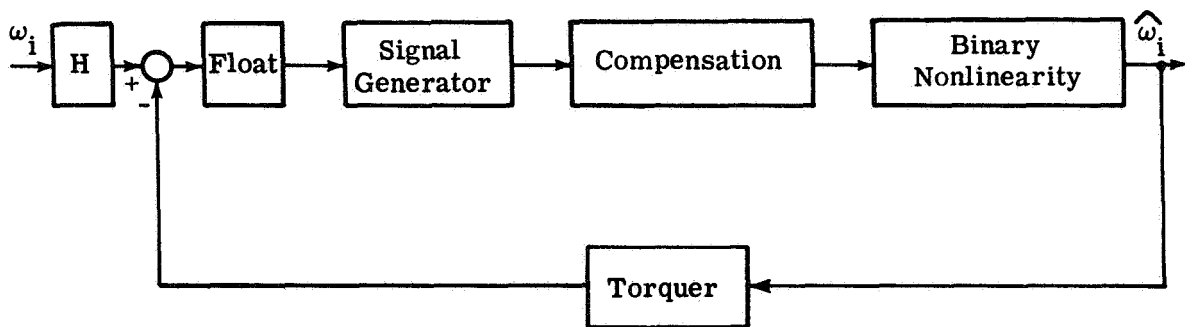


Figure 4.3-2 Position of Binary Gyro Loop Compensation

From Fig. 4.3-1 it can be seen that the linear compensation necessary to provide an open loop gain-phase characteristic which coincides with the unity closed loop gain curve must provide rapidly increasing phase lag with little change in amplitude ratio at frequencies immediately below ω_g . A resonant second order system provides rapid changes in phase shift but gives a sharp amplitude ratio peak. By cascading such a system with a first order lag to reduce the gain peak, it was hoped that the desired gyro open loop characteristics could be achieved. For the gyro parameters postulated, this form of compensation produces both amplification and attenuation in the critical range of frequencies, $\omega < \omega_g$. Departure from unity closed loop gain is not desirable at any frequency. Large amplification

in particular is associated with limit cycle quenching. In view of the fact that this compensation scheme cannot produce a perfectly flat response, the best course of action is to choose a set of compensation parameters which will minimize the maximum deviation of any part of the closed loop response from unity gain. The values used to get the response shown are:

$$\begin{aligned} \text{resonant natural frequency} &= 159 \text{ Hz} \\ \text{resonant damping ratio} &= 0.03 \\ \text{lag time constant} &= 3.3 \times 10^{-4} \text{ sec} \end{aligned}$$

The resulting closed loop response has a maximum gain of approximately 1.29 at 48 Hz and a minimum gain of about 0.80 at 100 Hz with a limit cycle frequency of 126 Hz. (The uncompensated gyro gain has a peak of about 7.5 at 230 Hz and $\omega_l = 318$ Hz.) The decrease in limit cycle frequency as a result of compensation is unavoidable. Since this form of compensation adds open loop phase lag, ω_l is lowered and the unstable bandwidth is always decreased when the binary limit cycling loop is compensated in this way. Also, because of the nature of binary torqued gyro loops, the limit cycle amplitude increases.

Another attempt to reduce variations in the closed loop gain uses a lead-lag-lag-lead network to generate the abrupt open loop phase shift required. The network transfer function is

$$\frac{(s\alpha\tau_c + 1)(s\frac{\tau_c}{\alpha} + 1)}{(s\tau_c + 1)^2}; \quad \alpha > 1$$

The parameter α is chosen to be 20. Selection of $\tau_c = 1/\omega_l$ causes the compensation to produce no phase shift at ω_l . Thus, the limit cycle frequency is unchanged.

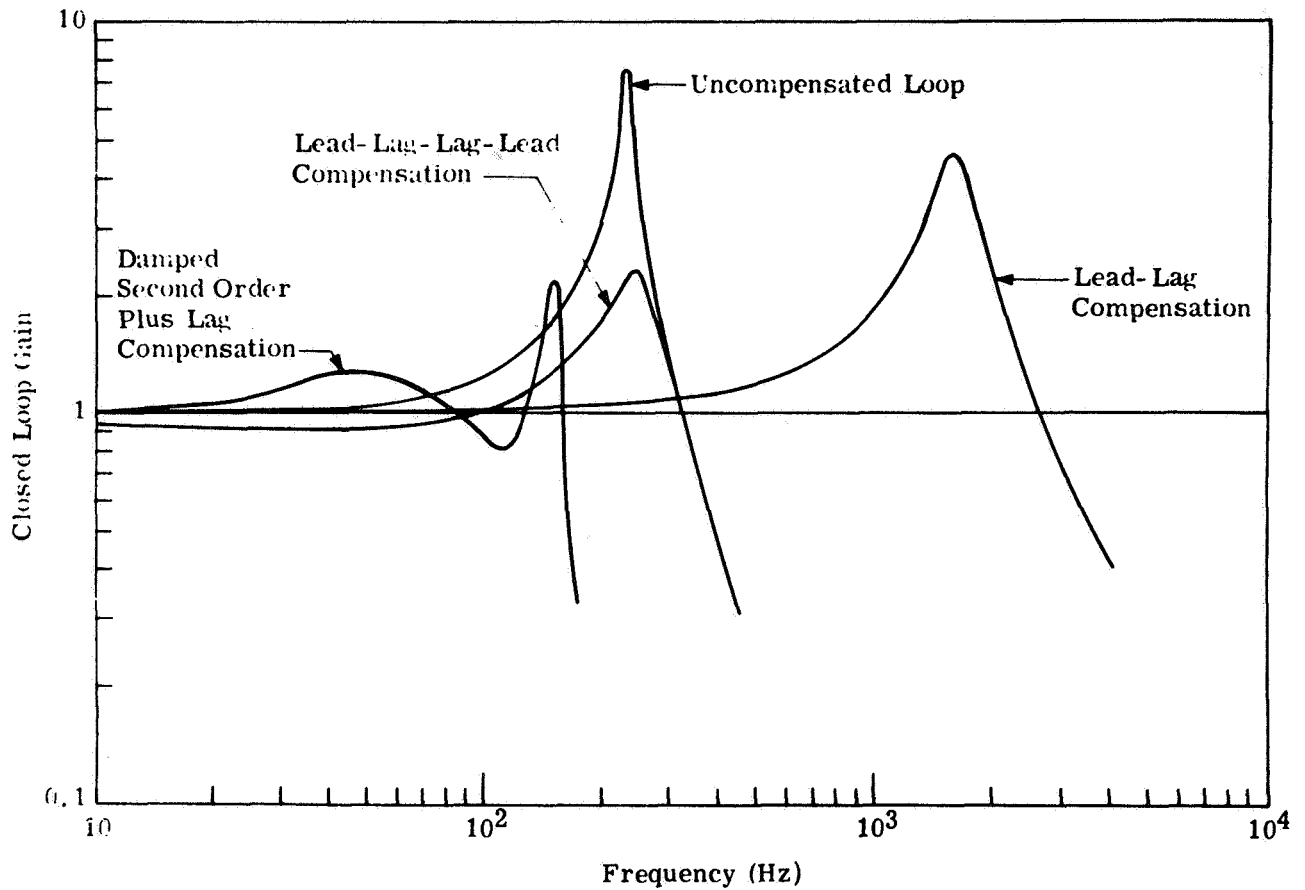


Figure 4.3-3 Closed Loop Gain for Limit Cycling Binary Gyro: Effect of Loop Compensation

If it is desired to increase the useful bandwidth of the loop without attempting to significantly alter the peak gain, lead-lag compensation is effective. A compensation network with the following transfer function was used to get the response illustrated in Fig. 4.3-3.

$$\frac{s\alpha\tau_c + 1}{s\tau_c + 1}; \quad \alpha = 20$$

$$\tau_c = 0.00005 \text{ sec}$$

Integral-Bypass Compensation - The motivation for using integral bypass compensation is to reduce the average low frequency float angle (taken over one or more limit cycle periods). Specifically, it is desired to use compensation at the nonlinearity input which approximates a pure integrator for low frequencies, thus giving the open loop a double integration characteristic for constant inputs. When the additional integration is inserted in the loop, the average float angle is zero for a constant input. This compensation also reduces the float angles caused by low frequency inputs.

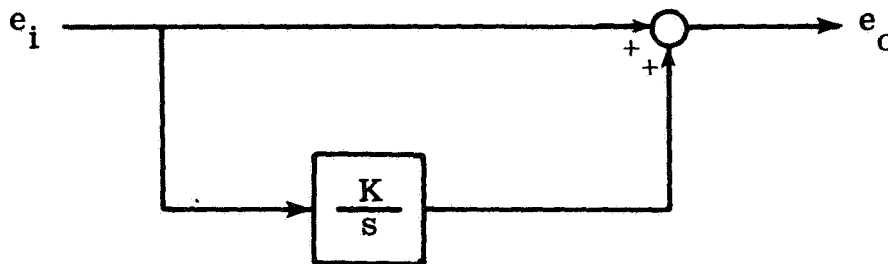


Figure 4.3-4 Block Diagram for Integral-Bypass Compensation

Integral-bypass compensation (see Fig. 4.3-4) has the transfer function

$$\frac{s + K}{s}$$

At low frequencies the transfer function is approximately K/s , while at high frequencies the compensation has unity gain, no phase shift and does not influence the loop response. The effect of integral bypass compensation is seen in Fig. 4.3-5 as a bending of the open loop response towards

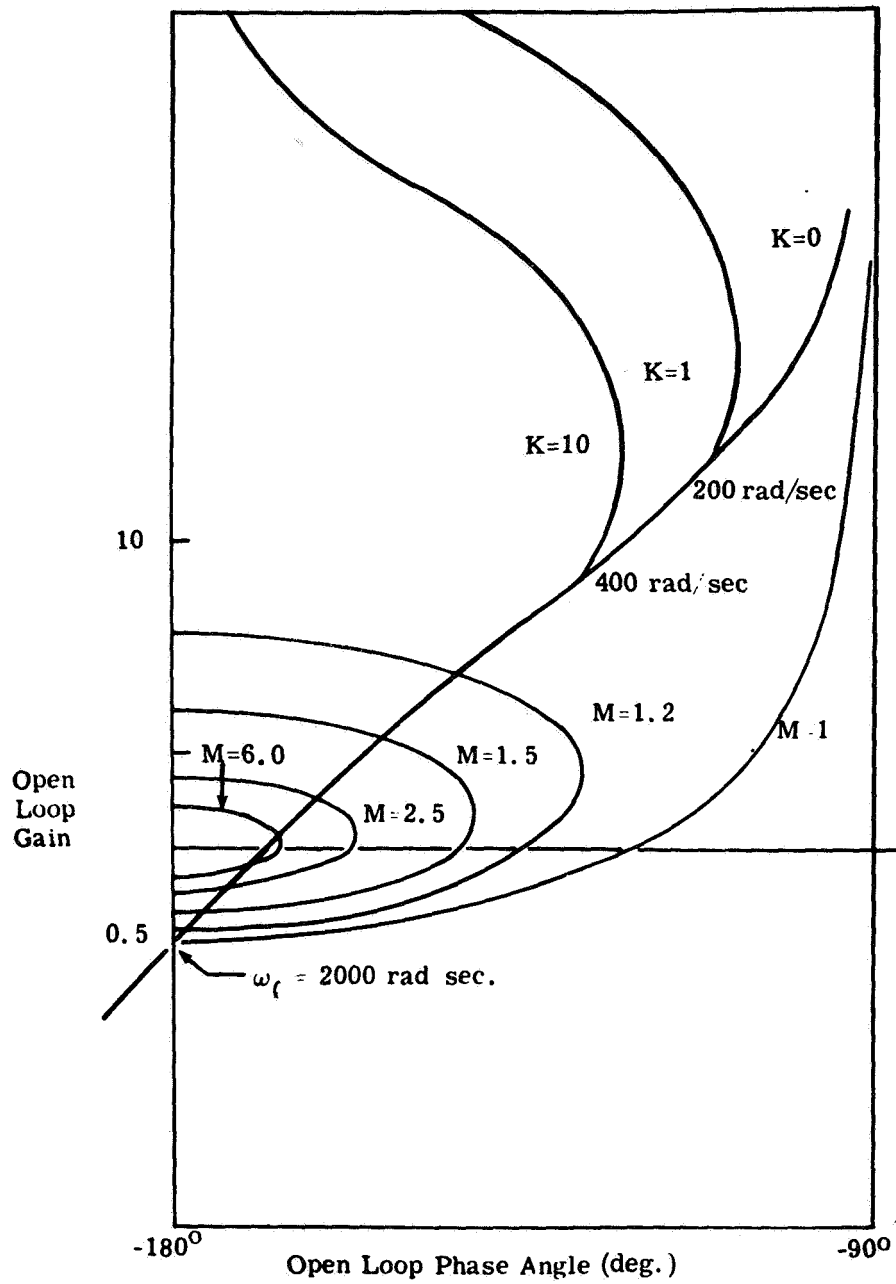


Figure 4.3-5 Nichols Chart Showing the Effect of Integral Bypass Compensation on Open Loop Response

the -180° phase line at low frequencies. Increasing K broadens the frequency range over which float motion is suppressed by enlarging the frequency band where the compensation behaves like an integrator. Note that a value of K as high as 10 has little effect on the limit cycle frequency or the closed loop response near ω_l . For values of $K \leq 10$, integral bypass compensation reduces the average float hangoff from low frequency inputs and leaves the closed loop response and limit cycle essentially unchanged.

Conclusions - The value of compensation in the limit cycling binary gyro loop has been studied analytically. Two forms of compensation which reduced the peak closed loop gain gave poor loop behavior at low frequencies. A third form of compensation, introducing lead into the gyro loop, increased the bandwidth of the gyro loop. Integral compensation was investigated as a means for stiffening the response of the gyro float to low frequency inputs. The investigation conducted was exploratory in nature and no consideration was given to the practical aspects of implementing the compensation schemes proposed.

4.4 LINEAR ANALYSIS OF THE DITHERED BINARY GYRO

The addition of a dither signal to the nonlinearity input of a binary torqued gyro can be used to create an approximately linear relation between the gimbal angle, α_0 , and the gyro output (see Ref. 1). Also, if attenuation of the dither oscillation by float dynamics is large enough, the dither nonlinearity can be represented as a limiter as shown in Fig. 4.4-1. Linear feedback analysis techniques can be used to investigate the transfer characteristics of the loop illustrated over a wide range of amplitudes and frequencies. However, the limiting nature of the new representation for

the dithered binary nonlinearity raises the possibility of a no-input limit cycle in the rebalance loop. Careful consideration reveals that the potential limit cycle in the dithered gyro is essentially the same unforced oscillation that occurs in any simple binary loop. Using the block diagram of Fig. 4.4-1, it can be seen that any limit cycle must have a frequency which provides π radians of phase lag in the linear part of the loop; the nonlinearity shown provides no phase change. The sinusoidal describing function for the limiter, N_A , is illustrated in Fig. 4.4-2. Peak gain occurs when the input sinusoid has an amplitude smaller than the dither magnitude, A_d . In that case the describing function is a constant, D/A_d , where D is the torquer current level. For a limit cycle to exist, the following relation must be satisfied:

$$N_A |H(j\omega_\ell)| = 1 \quad (4.4-1)$$

For the gyro model illustrated the open loop gain at the limit cycle frequency is;

$$|H(j\omega_\ell)| = \frac{K_{sg} K_{tg}}{C} \frac{\tau_f \tau_{tg}}{\tau_f + \tau_{tg}} \quad (4.4-2)$$

Consequently, to prevent a limit cycle the dither amplitude must be chosen so that

$$A_d > \frac{K_{sg} K_{tg} D}{C} \frac{\tau_f \tau_{tg}}{\tau_f + \tau_{tg}} \quad (4.4-3)$$

If the dither frequency attenuation by the float is sufficient (validating the representation of the nonlinearity shown in Fig. 4.4-1) and Eq. (4.4-3) is

satisfied, the application of dither at the input to the binary nonlinearity will prevent the occurrence of a limit cycle. Analysis of the dithered gyro loop for a wide range of inputs can then proceed using techniques developed for linear feedback systems.

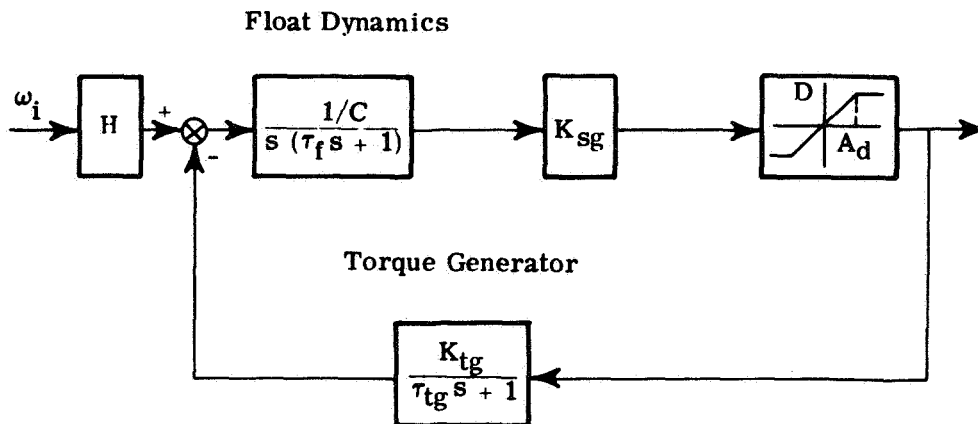


Figure 4.4-1 Dithered Binary Gyro

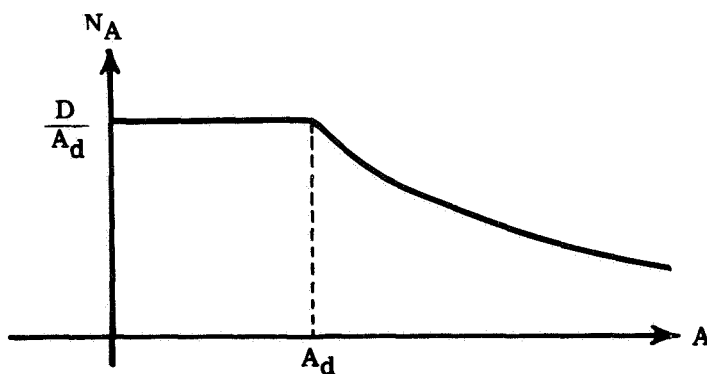


Figure 4.4-2 Describing Function for the Limiter

Example - Consider a single-degree-of-freedom gyro with the following parameters:

$$\begin{aligned}
 I_{oo} &= 250 \text{ gm-cm}^2 \\
 K_{tg} &= 1200 \text{ dyne-cm/mA} \\
 H &= 2 \times 10^5 \text{ gm-cm}^2/\text{sec} \\
 C &= 1 \times 10^5 \text{ dyne-cm-sec} \\
 K_{sg} &= 20 \text{ mv/mrad} \\
 \omega_{i\max} &= DK_{tg}/H = 1 \text{ rad/sec}
 \end{aligned}$$

Using Eq. (4.4-3), the minimum dither amplitude to preclude a limit cycle is 3.84 mV and the slope of the linear portion of the nonlinearity, $K_1 = D/A_d$, is 43.2 mA/mV. The natural frequency and damping ratio of the linearized gyro loop (ignoring torquer dynamics) are

$$\omega_n = \sqrt{\frac{K_{sg} K_{tg} K_1}{I_{oo}}} = 325 \text{ Hz} \tag{4.4-4}$$

$$\zeta = \frac{1}{2\pi_f \omega_n} = 0.098$$

Figure 4.4-3 illustrates the resultant frequency response for the linearized loop. For purposes of comparison the frequency response of a limit cycling binary gyro with the same parameters is shown. In interpreting the curve shown it should be remembered that for the dithered binary gyro no oscillation faster than half the dither frequency can be accurately detected at the gyro output. This is a consequence of averaging over each dither cycle. As the dither amplitude is increased above the minimum value required to prevent a limit cycle, K_1 decreases. From Eq. (4.4-4) it can be seen

that the natural frequency of the linearized gyro decreases and its damping ratio increases when A_d is made larger. The amplitude ratio frequency response for the dithered gyro is also shown in Fig. 4.4-3 for the case where dither amplitude is twenty-five times the minimum value computed above. Note the difference from that achieved by the limit cycling gyro.

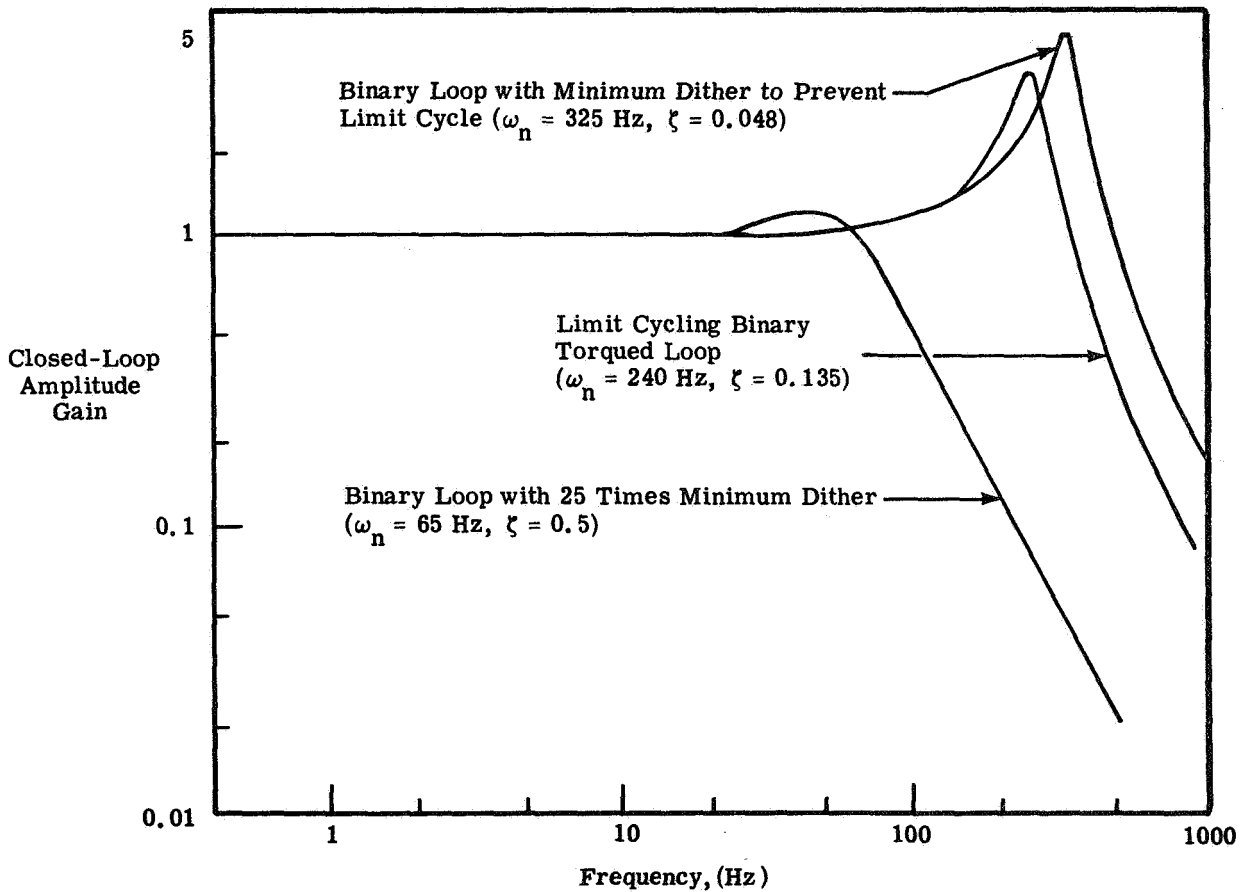


Figure 4.4-3 Frequency Response Characteristics for Binary Rebalance Loop

When the dithered binary gyro is represented as illustrated in Fig. 4.4-1 the frequency response characteristics of the second order linearized rebalance loop can be controlled by varying dither amplitude. However, damping ratio and natural frequency cannot be controlled

independently. Any increase in damping ratio (increase in dither amplitude) necessarily implies a decrease in natural frequency. In the example, the entire range of desirable loop transfer characteristics (ω_n and ζ) can be generated using dither signals large enough to prevent a limit cycle. Considerably more design flexibility is available with the dithered binary gyro. In addition, the interdependence of peak closed loop gain and bandwidth can be eliminated through insertion of linear compensation in the loop. The whole range of linear systems techniques is available for analyzing the dithered loop.

The use of a dither signal with a ternary nonlinearity offers no advantage relative to the technique discussed above.

5.

TERNARY PULSE REBALANCED GYRO

SUMMARY

Research Performed - The behavior of ternary pulse torqued gyros is predicted analytically. A major portion of the effort is devoted to determining the closed loop gain characteristics of ternary gyros and verifying the analysis by simulation. The influence of rotor bearing compliance is also analyzed and the predicted gyro response is checked by simulation. The effects on the ternary gyro frequency response of different gyro input amplitudes and random noise at the logic inputs are also treated.

Results - It is demonstrated that the closed loop behavior of ternary pulse rebalanced gyros can be accurately predicted. The gain and phase characteristics observed during simulation are in close agreement with those computed analytically.

It is shown that the ternary pulse rebalanced gyro can exhibit a jump resonance in its closed loop response to sinusoidal inputs. This history-dependent gain and frequency shift is observed in both the analysis and the simulation. In addition, analysis indicates that the gyro has a transfer characteristic which can depend greatly on the amplitude of the input signal; the ternary gyro loop transmission is nonlinear. The latter property was not thoroughly checked by simulation but enough confidence has been gained in the analytic technique that the conclusion is considered to be correct.

The effect of rotor bearing compliance on the ternary gyro loop response is similar to that found for the binary gyro. Both analysis and simulation indicate that bearing compliance can reduce the useful bandwidth of the gyro. Good agreement between the two approaches

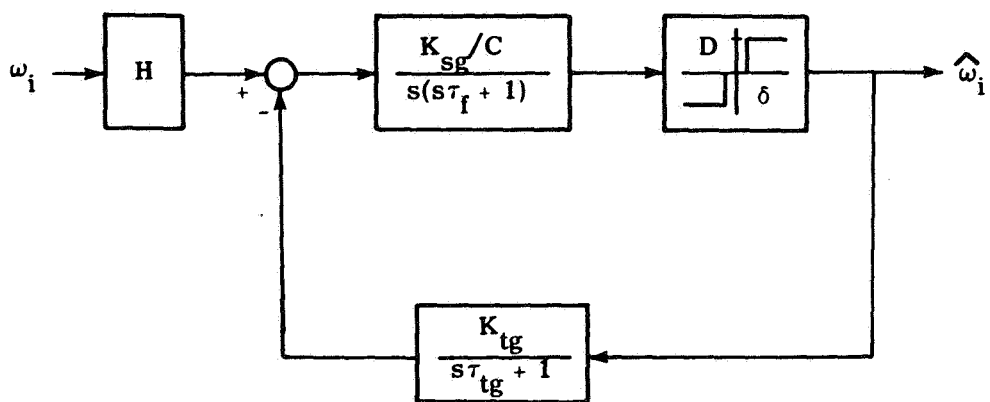
is observed, verifying the utility of the analytic technique. The addition of Gaussian noise to the signal representing float angle is analytically shown to create a more nearly linear transfer characteristic in the ternary gyro.

Conclusions Related to Gyro Design - It is demonstrated that the characteristics of ternary pulse rebalanced gyros can be predicted analytically. However, considerably more effort is required than for the binary gyro. No simple set of equations permits quick calculation of ternary gyro response. There is no limitation on the complexity of the linear gyro loop dynamics which can be treated by this approach.

Non-unique closed loop gains are predicted and observed for the ternary gyro, indicating that this instrument can exhibit an ambiguous response for inputs in a certain frequency range. In addition, analysis indicates that in a large band of input frequencies the ternary gyro loop gain depends on the input amplitude. These two observations suggest that a ternary pulse rebalanced gyro should not be used where high frequency angular vibrations must be measured accurately. As with the binary gyro, rotor bearing compliance can reduce the bandwidth of the ternary gyro.

Analysis indicates that the presence of random noise in the signal representing float angle can cause the ternary gyro to behave in a more linear fashion. However, the technique employed in the analysis does not permit phase shift characteristics to be specified. Further investigation is required before a random noise (dither) is intentionally added in the signal electronics of a ternary gyro to give a better response.

Introduction - Describing function analysis was shown to be of considerable value for treating the binary gyro in Section 4. Similar techniques are applied below to the ternary gyro of Fig. 5.1-1. Though the approach is basically the same, the effort involved is greater. Again, in order to simplify the problem the sampling nature of the pulsed gyro loop is ignored.



δ = dead-zone threshold in mV
 D = drive level in mA

Figure 5.1-1 Gyro Pulse Rebalance Loop with a Ternary Nonlinearity

5.1 ANALYSIS OF THE FREQUENCY RESPONSE CHARACTERISTICS OF THE TERNARY GYRO

As in Section 4, we desire to make approximations which will permit application of linear analysis techniques for determining the closed loop response to sinusoidal inputs. With the binary gyro, the presence of a limit cycle allowed us to approximate the describing function gain to a signal sinusoid by a quantity which depends only on the limit cycle amplitude

The closed loop frequency response to the signal was then determined by replacing the nonlinearity with the appropriate gain and applying conventional linear analysis techniques. Unfortunately, the ternary gyro does not exhibit a clearly defined limit cycle and the describing function gain of the three level nonlinearity must be treated as a function of the amplitude of the signal entering it. Also, because the float provides frequency dependent attenuation, the amplitude of a sinusoid entering the nonlinearity is a function of both the magnitude and frequency of the gyro loop input. Consequently, a different size sinusoid appears at the input of the nonlinearity for each frequency and amplitude combination applied at the loop input. For each input combination explored in the course of a frequency response analysis, a different nonlinearity equivalent gain must be calculated and a separate determination of system output amplitude made--all to obtain one value of closed loop gain. To simplify matters in the example which follows, the input amplitude is held constant and only the frequency varied to obtain a plot of closed loop gain. However, it should be emphasized that a different curve will result from each value of input amplitude assumed.

Linearization of the Ternary Nonlinearity - The gain approximation used to describe the ternary nonlinearity is the Sinusoidal Input Describing Function (SIDF), written $N_A(A)$ and defined as the ratio between the amplitude of the fundamental sinusoid at the nonlinearity output and the amplitude A of the pure sinusoidal input to the nonlinearity. $N_A(A)$ is evaluated from:

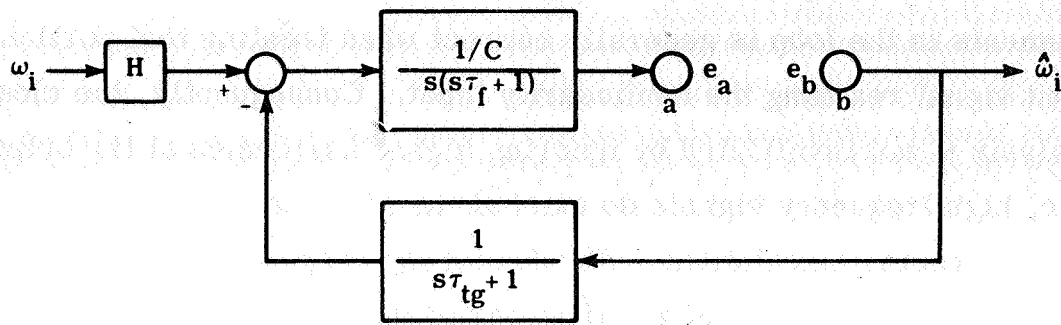
$$N_A(A) = \frac{4D}{\pi A} \sqrt{1 - \left(\frac{\delta}{A}\right)^2} \quad (5.1-1)$$

It should be noted that the SIDF gain relates only to the first harmonic of the waveform at the nonlinearity output. All higher harmonics are ignored. They are assumed to be attenuated when passed through torquer and float

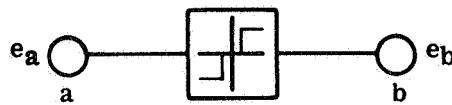
dynamics. The assumption that the higher harmonics are removed by low pass elements in the loop is generally correct when treating that portion of the output signal reaching the nonlinearity input. Consequently, the closed loop analysis is not invalidated by ignoring higher harmonics at the output. However, high frequency signals do exist at the gyro output and will enter the direction cosine calculations. The frequency response curves obtained in this section account only for the first harmonic of the gyro loop output. The signal entering the nonlinearity is essentially the sum of the output fundamental and the loop input signal, both filtered by float dynamics. The sampling nature of the nonlinearity is ignored in the analysis which follows.

Analysis Example: Simple Gyro Dynamics - The gyro loop is divided into two parts (see Fig. 5.1-2) each of which will be treated separately to obtain certain characteristics. Then the two similar sets of relations are compared to obtain a simultaneous solution for the system. The technique is analogous to load line solutions in electrical engineering. Lineal analysis is applied to the portion of the system shown in Fig. 5.1-2a. If ω_i is a sinusoid of known magnitude, an amplitude relation can be obtained between two sinusoids of the same frequency as the input, one at point a and the other at point b. This ratio results from linear theory and does not depend on the specification of an open loop gain relation between the signals e_a and e_b (see Appendix E). When plotted for a particular gyro, the relation defines an ellipse for each different amplitude and frequency of the input sinusoid. If the input magnitude is assumed constant, a set of ellipses, illustrated in Fig. 5.1-3, results. Each ellipse represents a different input frequency.

The ternary nonlinear element is treated separately (see Fig. 5.1-2b). The describing function, Eq. (5.1-1), is used to obtain a relation similar to that computed from linear system theory. This characteristic, illustrated in Fig. 5.1-4, depends on the quantities D and δ . When the plots



(a) Linear Part of the Loop



(b) Nonlinear Element

Figure 5.1-2 Pulse Rebalance Loop Divided into Linear and Nonlinear Parts

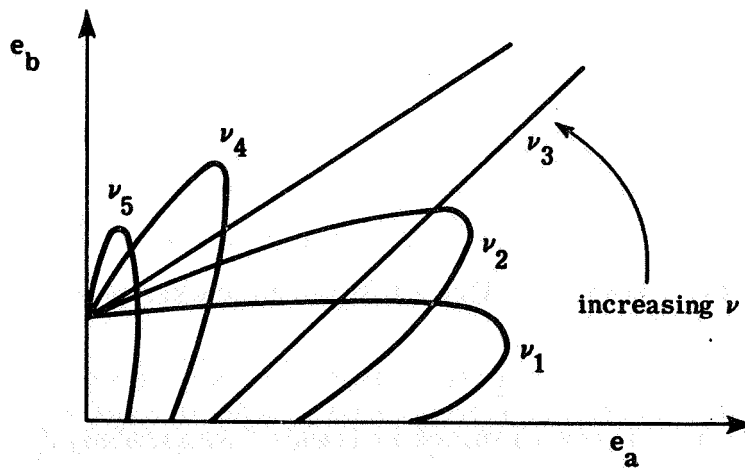


Figure 5.1-3 Ellipses Resulting from Analysis of the Linear Portion of the Loop

representing the two parts of the loop are superimposed in Fig. 5.1-5, the intersections constitute a set of operating points for the system. Since each ellipse represents a different loop input frequency, each intersection with an ellipse represents a loop operating point at that frequency. Every intersection point also supplies a particular value for the nonlinearity output. Since the output of the nonlinearity is also the loop output, the absolute value of the loop transfer function is simply e_b divided by the input amplitude. The ratios obtained for the ellipse of a particular frequency, ν , represent possible closed loop system gains to a sinusoid at that frequency. However, not all of the intersections represent stable solutions.

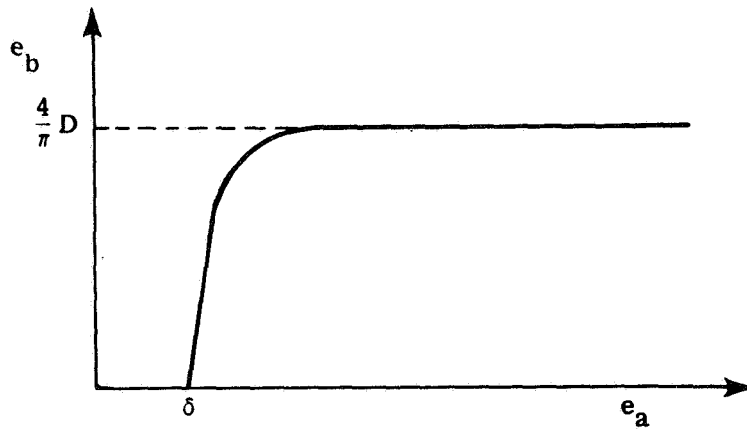


Figure 5.1-4 Output vs Input Computed from the SIDF Gain for the Nonlinearity

By determining a sufficient number of intersection points, it is possible to construct a closed loop amplitude ratio response curve for the ternary gyro. Figure 5.1-6 illustrates such a curve drawn from the intersection points determined in Fig. 5.1-5. The peaked portion of the closed loop response curve exhibits a "jump resonance" characteristic similar to that given by a softening spring. The effect of deadzone on the closed loop

gain is seen as an abrupt drop to zero at the frequency ν_c . If there was no deadzone, the response gain would fall off gradually with increasing frequency. However, the deadzone causes the relay to block all signals whose amplitude at the nonlinearity input is less than δ . As frequency increases, the float gain decreases until, at frequency ν_c , input amplitude at the nonlinearity input is less than δ . Then the output, and consequently the loop gain, drops abruptly to zero. Deadzone also causes the overhanging nature of the response curve. At high input frequencies, attenuation by float dynamics prevents the input to the nonlinearity from exceeding δ . As frequency is decreased the float angle eventually becomes larger than the deadzone, providing a loop output and generating signals at all points in the loop. This occurs at a frequency different from ν_c because the gyro is essentially an open loop system until an output appears at the nonlinearity.

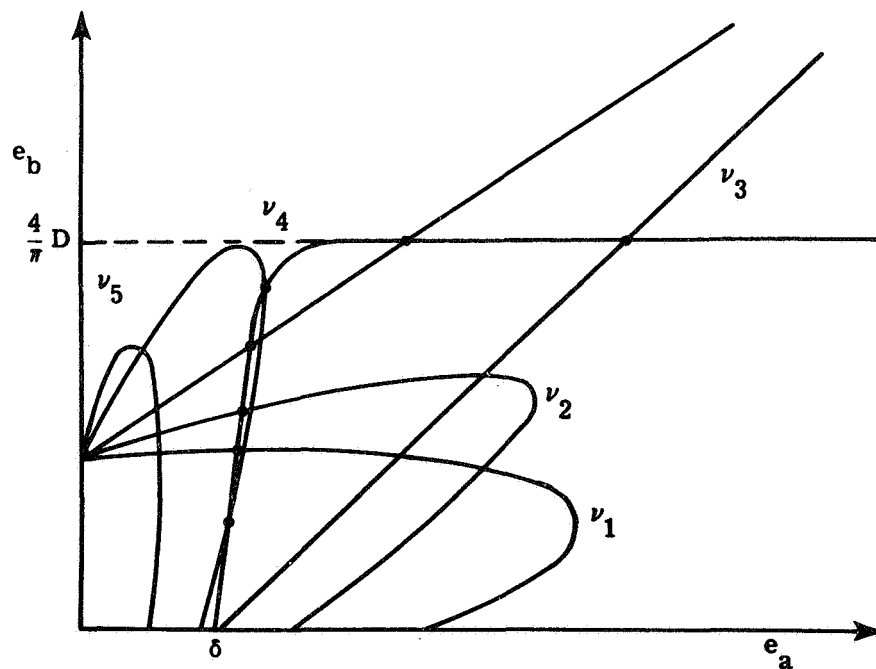


Figure 5.1-5 Superposition of Figs. 5.1-3 and 5.1-4 Showing Intersection Points

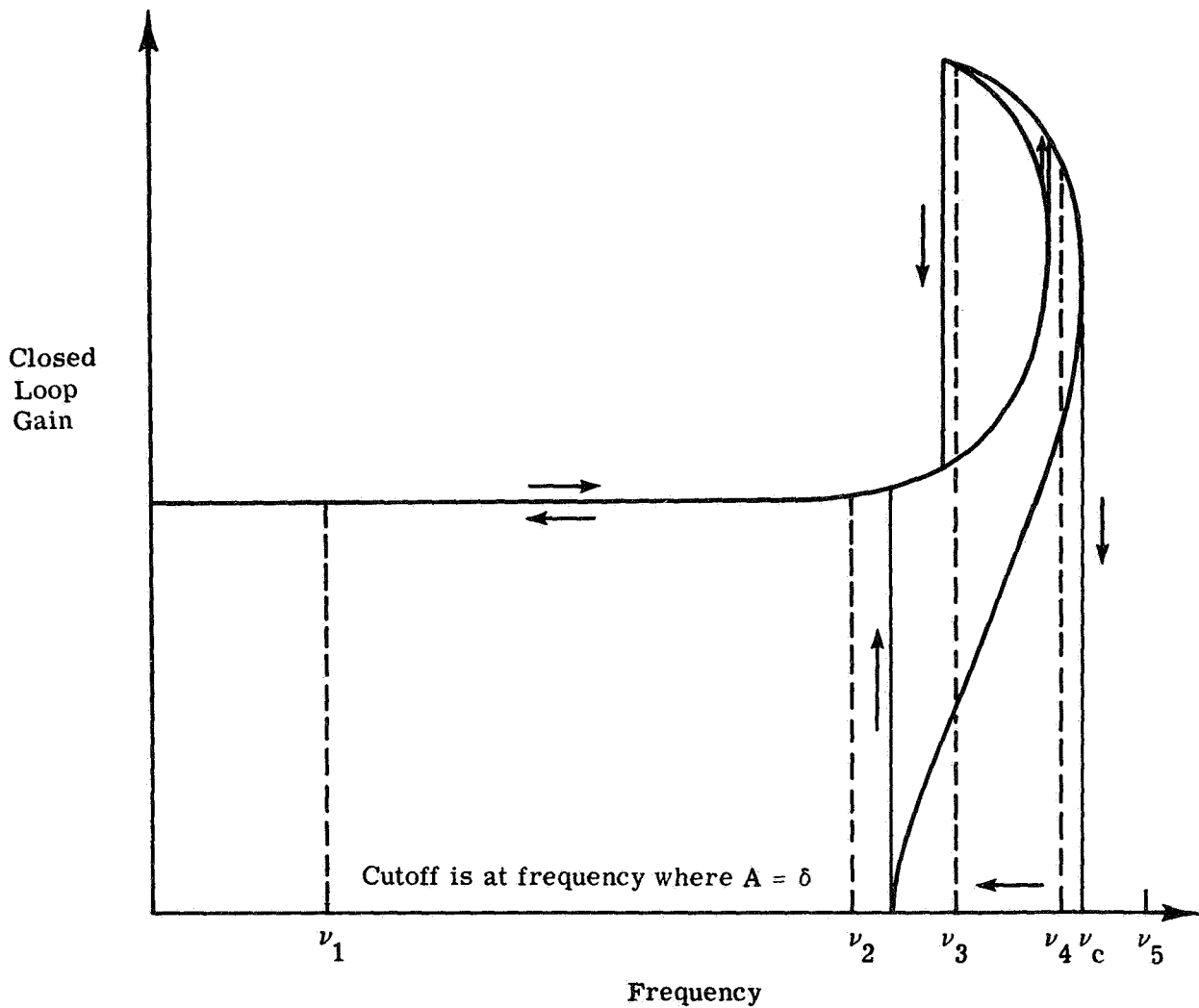


Figure 5.1-6 Ternary Gyro Closed Loop Gain

Effect of Input Amplitude - Because the nonlinearity it contains has an amplitude dependent output, the ternary gyro loop exhibits amplitude dependent characteristics. When plotted for different magnitudes of the input sinusoid, the frequency response curves have various shapes (see Fig. 5.1-7). If the input amplitude is small enough (0.01 rad/sec in the figure) the closed loop response has no peak. As the size of the input

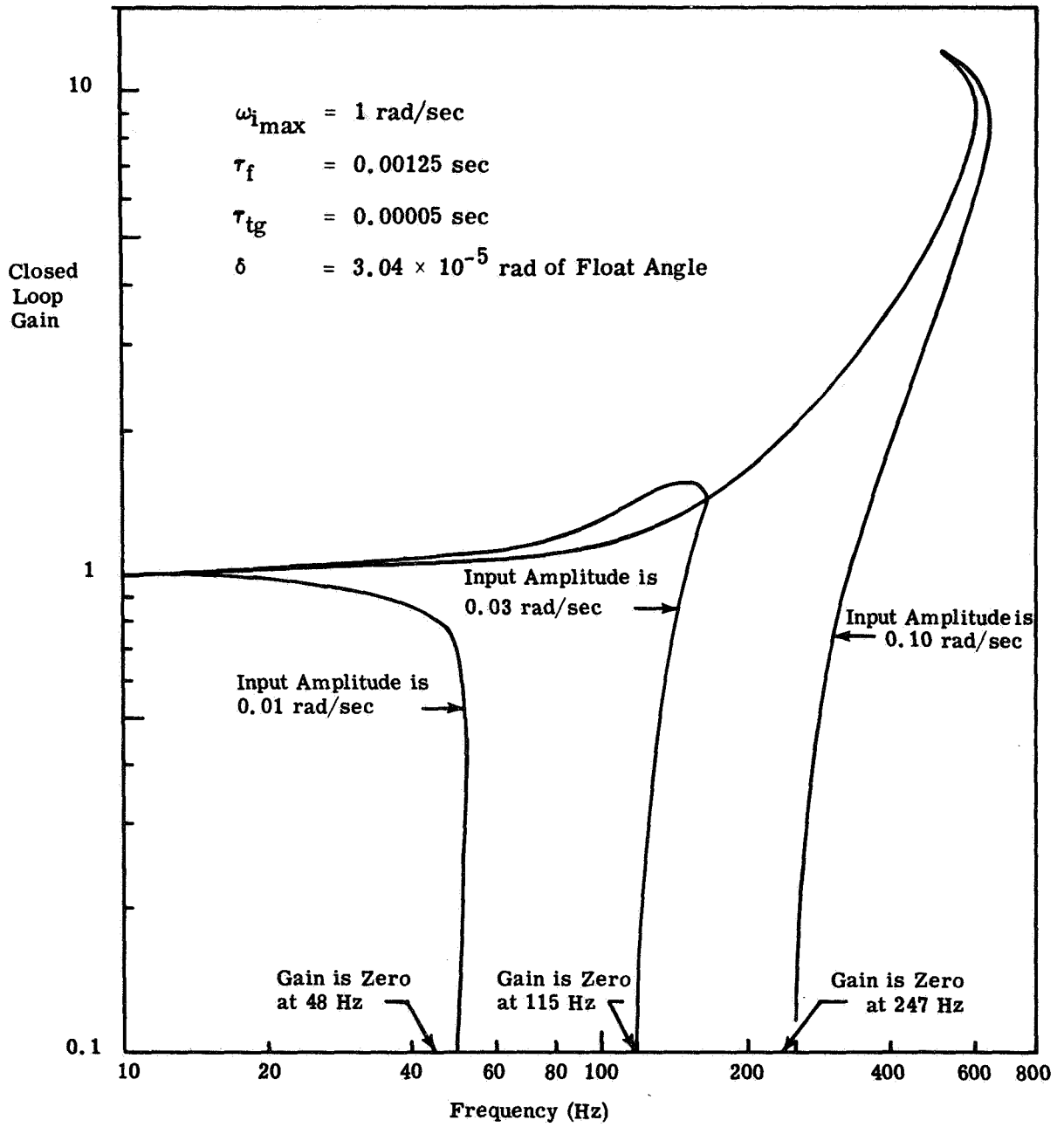


Figure 5.1-7 Effect of Input Amplitude on Closed Loop Gain of a Representative Ternary Gyro Loop

increases the jump resonance characteristics and dual gain cutoffs discussed above become more pronounced. A look at Fig. 5.1-5 provides an explanation. The ellipsoidal curves obtained from linear analysis are changing size and rotating. As frequency increases, the length of the major axis first increases, then declines. However, rotation of the major axis is monotonic. For the smallest input amplitude plotted in Fig. 5.1-7 no appreciable rotation of the ellipses takes place before the loop output drops to zero. When the gyro input is raised to 0.03 rad/sec the ellipses rotate and the intersection points occur at higher values of e_b , giving a peaked loop response. When the largest input is analyzed, the ellipses not only rotate but also become long enough to provide several intersection points at some frequencies. A jump resonance characteristic results. The fact that ternary gyros have a gain which depends on the input amplitude is a serious disadvantage for this type of instrument. If it is necessary to accurately measure high frequency angular vibrations, the ternary pulse rebalanced gyro does not appear satisfactory.

Gyro Dynamics when Rotor Bearing Compliance is Considered -

The loop with rotor-to-gimbal compliance is treated in the same manner as that with simple dynamics discussed above. Ellipses are generated to describe the linear part of the loop using the equations in Section 4.1.2. The SIDF gain for the nonlinearity remains unchanged. Points of intersection between the ellipses and the nonlinearity input-output characteristics define the loop output amplitude as a function of frequency. From this information, the closed loop gain to a sinusoid is inferred. Consideration of rotor bearing compliance does not change the basic procedures followed in obtaining the closed loop frequency response from describing function analysis.

5.2 SIMULATION OF THE TERNARY GYRO

The analytic techniques demonstrated in Section 5.1 provide interesting insights into the closed loop behavior of the ternary-torqued gyro loop. However, the accuracy of these predictions depends on how faithfully the describing function approximation characterizes true non-linearity performance. As a check on the validity of this approach, characteristics of certain ternary loops were computed and the results verified using analog computer simulation.

5.2.1 Simple Gyro Dynamics

A set of parameters is chosen to represent a typical ternary gyro loop with second order gyro dynamics (see Fig. 5.1-1):

$$\begin{aligned}\omega_{i_{\max}} &= 1 \text{ rad/sec} & \tau_{tg} &= 0.00005 \text{ sec} \\ \tau_f &= 0.00125 \text{ sec} & \delta &= 4.17 \times 10^{-5} \text{ rad about the} \\ & & & \text{input axis} \\ H/C &= 1\end{aligned}$$

With the exception of the nonlinearity deadzone δ , these are the same values as those shown in Fig. 5.1-7. A different value of deadzone was used for this comparison to ensure that no limit cycle took place in the simulated gyro loop. Oscillatory angular rate inputs with a peak amplitude of 0.1 rad/sec were applied to the simulated gyro. Figures 5.2-1 and 5.2-2 show records of the input, float angle and torquer output when two different input oscillation frequencies were simulated. The sampling rate in both cases illustrated is 1 mHz providing essentially continuous ternary loops. The closed loop frequency response of this gyro is distinguished by a peak at 400 Hz (see Fig. 5.2-3). Discrete points obtained via simulation are indicated while the curve predicted by describing function analysis

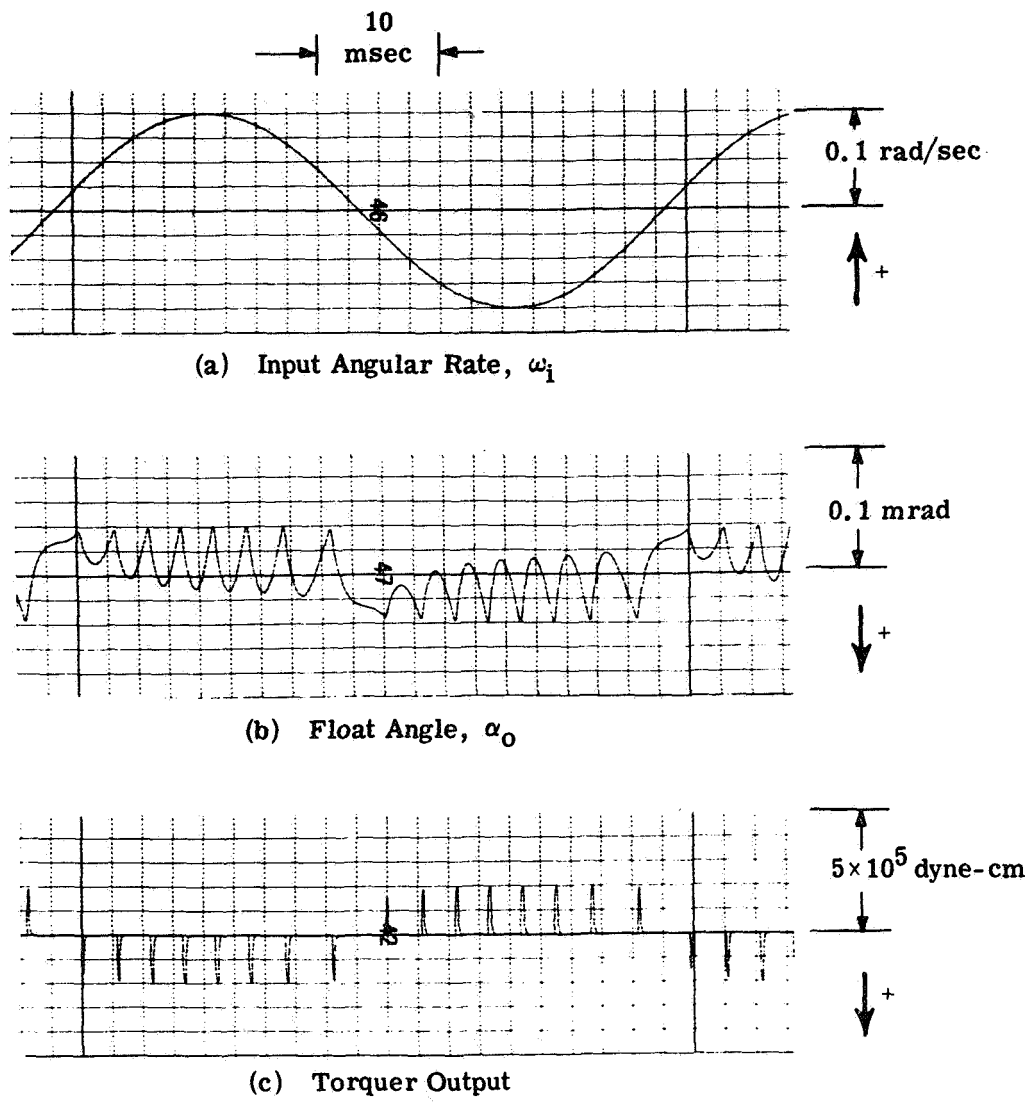
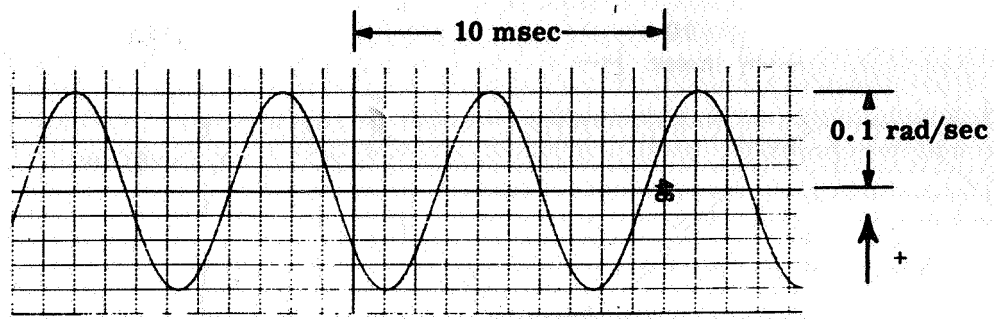
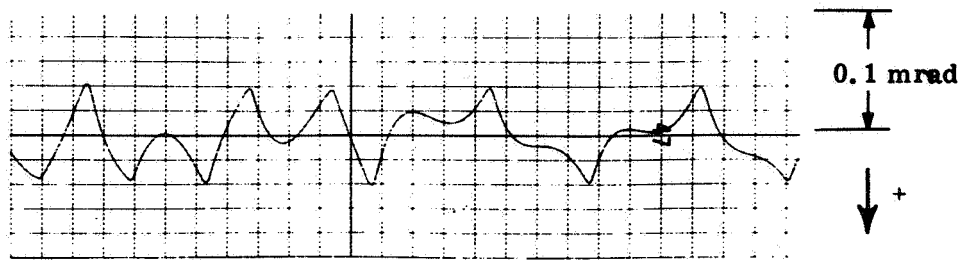


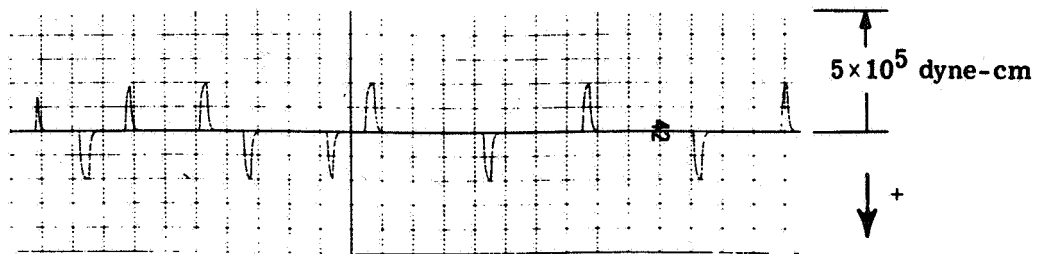
**Figure 5.2-1 Ternary Gyro Simulation Records:
20 Hz Input**



(a) Input Angular Rate, ω_i



(b) Float Angle, α_o



(c) Torquer Output

Figure 5.2-2 Ternary Gyro Simulation Records:
150 Hz Input

appears as a solid or dashed line. Note that the analytic response contains unstable segments in the jump resonance region which cannot be observed for any length of time by simulation. They represent unstable modes which do not occur in the actual instrument either. Agreement between the analytic and simulation results is quite good on the stable portions. The response is similar in shape to the curve seen in Fig. 5.1-7.

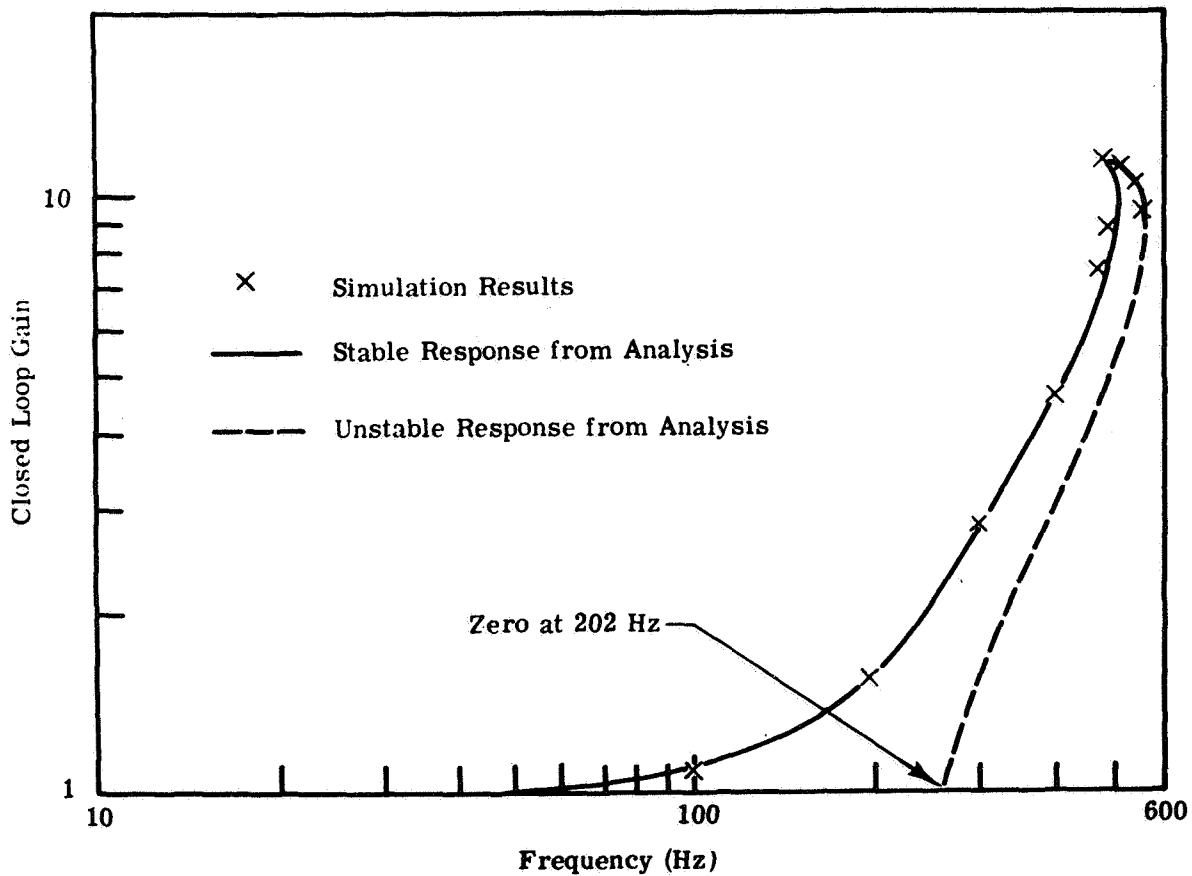
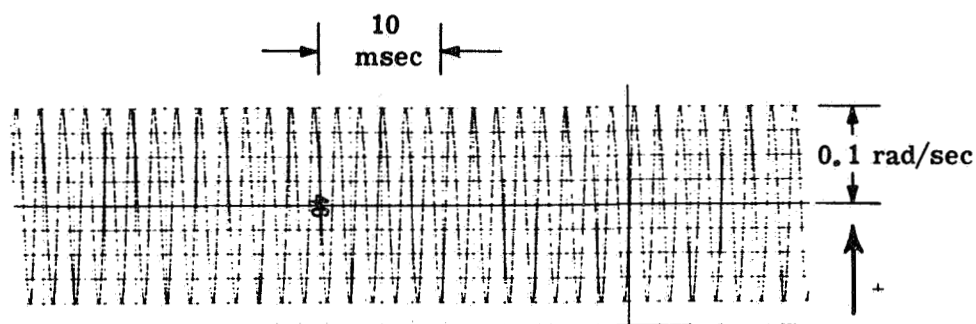
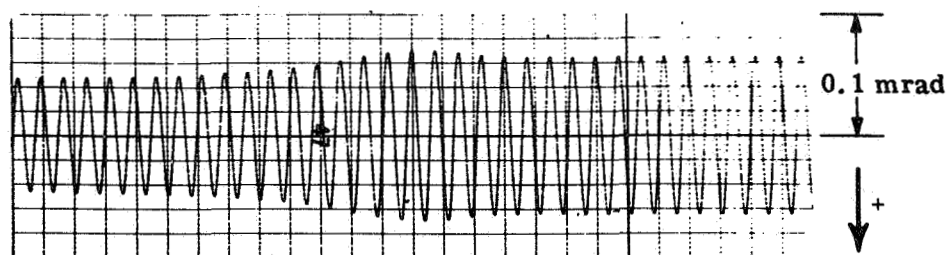


Figure 5.2-3 Frequency Response of a Ternary Gyro: Comparison of Analytic and Simulation Results

Figure 5.2-4 presents simulation records illustrating the behavior of the ternary gyro float angle at a jump resonance point. The input frequency is being raised so slowly that the change cannot be detected on the record, but the gyro float angle behavior shows a clear discontinuity. The gain of the gyro loop was observed to increase suddenly at the point where α_0 becomes larger.



(a) Input Rate, ω_i



(b) Float Angle, α_0

Figure 5.2-4 Ternary Gyro Simulation Record Illustrating Jump Resonance

5.2.2 Gyro Dynamics with Rotor-to-Gimbal Compliance

The same gyro discussed in Section 5.2.1 is treated here for the case where compliance between the rotor and gimbal are significant. The parameters related to compliance are:

$$\begin{aligned}\omega_g &= 4000 \text{ rad/sec} \\ \nu_n &= 2512 \text{ rad/sec} \\ \rho &= 0.02\end{aligned}$$

The float time constant, τ_f , is not the same quantity when the rotor and gimbal are not rigidly connected. The value $\tau_f = 0.001$ sec was used. The frequency response curve for this system has a peak centered near 180 Hz as shown in Fig. 5.2-5. The solid line represents the analytic solution and simulation results appear as discrete points. As before, certain points indicated analytically are unstable and cannot be observed. The simulation points substantiate quite well the response obtained by describing function analysis, however.

Note that the response peak resulting from consideration of compliance dynamics occurs at a noticeably lower frequency than the peak associated with a second-order description of the gyro. Apparently, the closed loop poles are radically altered by including compliance dynamics in the loop. There appears to be some correlation between the location of this peak and the low frequency complex conjugate poles of the transfer function relating torque exerted on the gimbal by the rotor to the input angular rate (Eq. (4.1-7)). The peak gain is centered at about 175 Hz, and the poles of the transfer function are at about 190 Hz. From a practical viewpoint this change in the frequency response can constitute a serious limitation on the useful bandwidth of the gyro loop. In the gyro analyzed, greater rotor bearing rigidity is required if the peak is to be moved to a higher frequency and a larger bandwidth (predicted by assuming simple gyro dynamics) is to be realized.

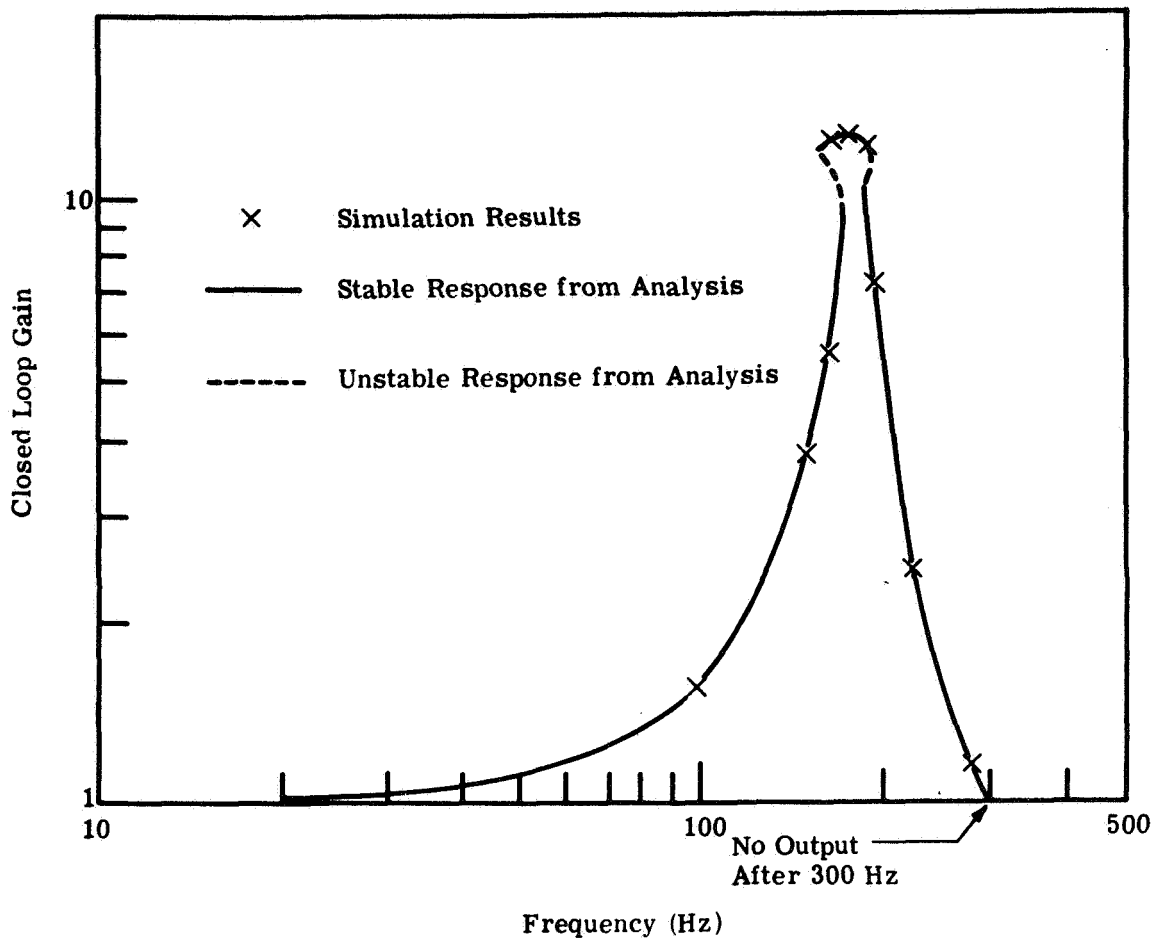


Figure 5.2-5 Frequency Response of a Ternary Gyro: Comparison of Analytic and Simulation Results when Rotor Bearing Compliance is Considered

5.3 EFFECT OF RANDOM SIGNAL AT THE NONLINEARITY INPUT

Describing function analysis is used to obtain the closed loop response of a ternary gyro when a Gaussian random signal is present at the nonlinearity input along with a sinusoidal signal. The random signal, described by its standard deviation, σ_r , can be present as a result of a random input to the gyro, noise in the loop, or deliberate injection in the form of a random dither. The present discussion makes no assumption about the origin of the random signal.

The Describing Function - Due to the presence of a random signal in addition to the sinusoid, the describing function gain to a sinusoid is different from that used in the previous section. It depends not only on the amplitude A of the sinusoidal input to the nonlinearity but also on the magnitude of the random input. A random signal can be described by its statistical moments. If it is assumed to be a Gaussian, zero mean variable its distribution is completely specified by a standard deviation, σ_r . The describing function for the sinusoid is written as $N_A(A, \sigma_r)$ and is given for the ternary nonlinearity in Appendix E of Ref. 3. As σ_r approaches zero $N_A(A, \sigma_r)$ becomes the describing function for a pure sinusoidal input. Figure 5.3-1 illustrates the effect of the random input on the sinusoid transfer characteristics of the ternary nonlinearity. It is similar to Fig. 5.1-4. The output characteristic shown is the average amplitude of the output harmonic of the same frequency as the sinusoidal input. The effect of a random input to the ternary nonlinearity is to make the rise of the sinusoidal input-output curve more gradual. When $\sigma_r > 0$ and $A < \delta$ there is a finite probability that the net input to the nonlinearity will exceed δ and have the same sign as the sinusoid. There is a smaller probability that it will exceed the dead-zone with the opposite sign. When the mean is taken, a non-zero average value for the appropriate nonlinearity output harmonic results. In this way

the sinusoid is boosted through the deadzone by the random signal. On the other hand, when A exceeds δ the fact that the noise input to the nonlinearity can have a sign opposite to that of the sinusoid produces a describing function gain somewhat lower than that occurring in the absence of random signals. It can be seen from Fig. 5.3-1 that the net effect of adding a random signal at the nonlinearity input is to make the describing function gain for the sinusoid less amplitude-dependent (more nearly linear).

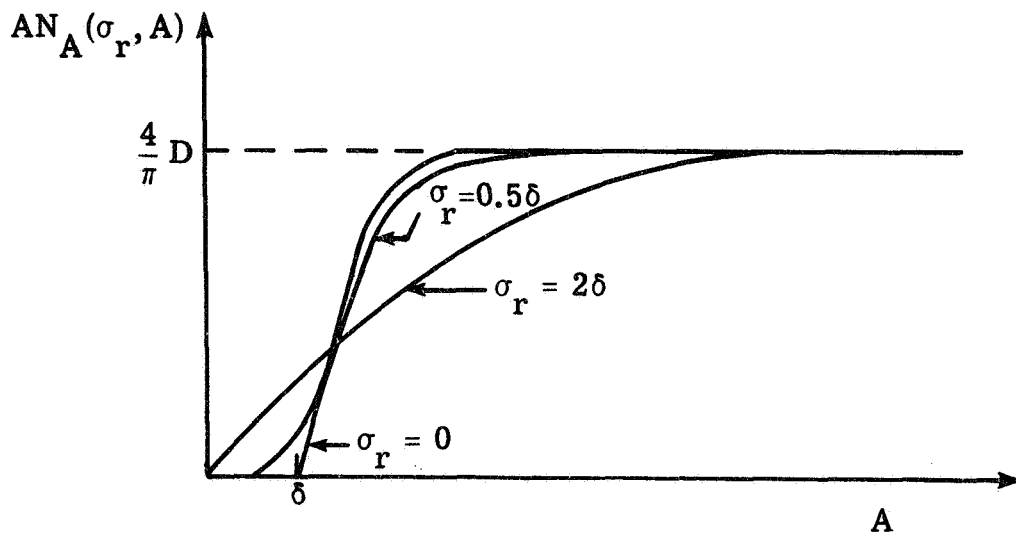


Figure 5.3-1 Effect of a Random Input on the Sinusoid Transmission Characteristics of a Ternary Nonlinearity

Unfortunately, the presence of the random signal in the loop involves more than just a change in N_A . Strictly speaking, σ_r must be determined through the use of a describing function gain $N_r(A, \sigma_r)$ and knowledge of the characteristics of the random signal at the point where it enters the gyro loop. Since N_A and N_r both depend on A and σ_r , solution of the closed loop relations in the presence of both a sinusoid and a

random signal requires a complicated iterative procedure. However, in order to illustrate the effect of random inputs to the nonlinearity we will assume different values of σ_r without specifying their origin.

The fact that the curves obtained represent the average response to a given sinusoid does not detract from their value. If we are interested in the effect of gyro output on a resonant mode of the direction cosine matrix calculation or on the system drift rate generated, the mean value representation is often as useful as an exact one.

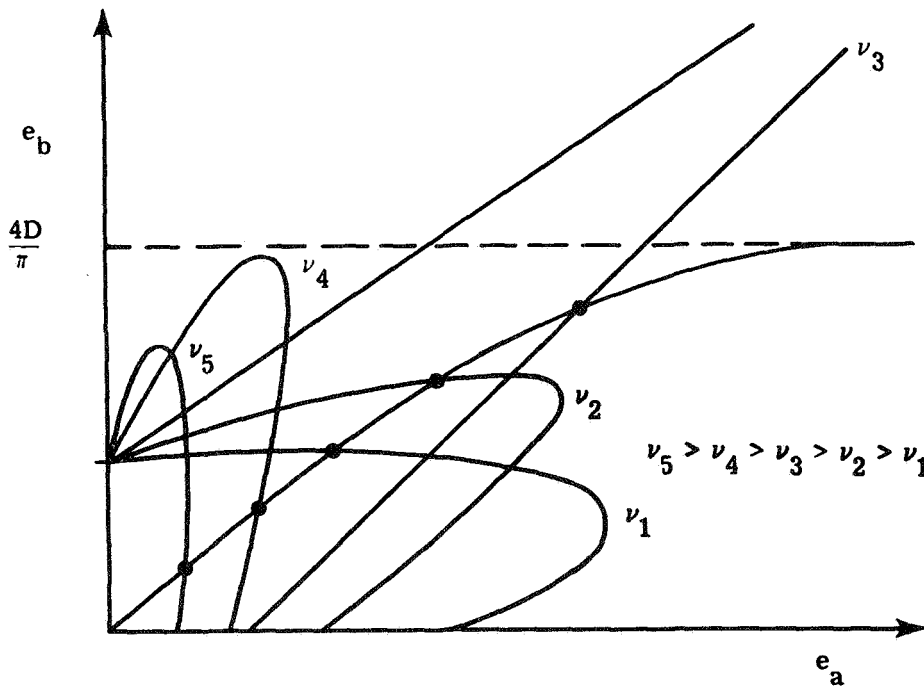


Figure 5.3-2 Ellipse Intersection Points Caused by Random Nonlinearity Input

Changes in the Frequency Response - Figure 5.3-2 indicates the ellipse intersection points for the sinusoid input-output curve which result when a random signal also enters the nonlinearity. Note that the

likelihood of multiple intersection points occurring on any one ellipse is reduced. In this particular example there are no multiple intersection points. Also, because there can be an output for $A < \delta$, all ellipses have at least one intersection point. The effect on the sinusoid frequency response is illustrated in Fig. 5.3-3. Since no ellipse has multiple intersections, there is only one value of closed loop gain at each frequency; the jump resonance phenomenon is eliminated. Also, the closed loop gain is more than zero for all frequencies and the sharp cutoff found in Fig. 5.1-4 is eliminated. Figure 5.3-4 shows the three frequency responses corresponding to the three nonlinearity curves of Fig. 5.3-1. As σ_r increases, the jump resonance disappears and bandwidth increases. Gradual gain reduction at high frequencies replaces the sharp attenuation. In short, when the random signal is present, the closed loop frequency response appears to be more like that of a linear system.

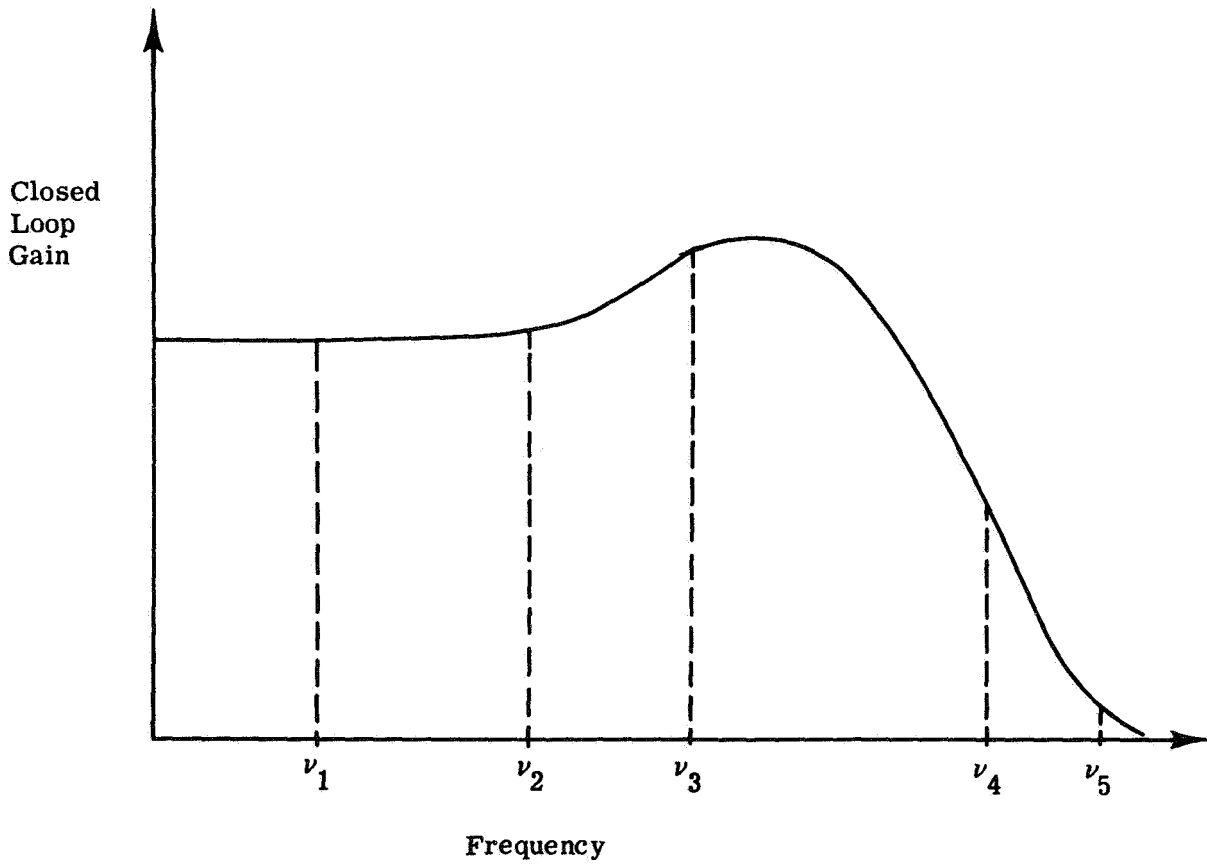


Figure 5.3-3 Closed Loop Response for a Ternary Gyro with a Certain Random Nonlinearity Input

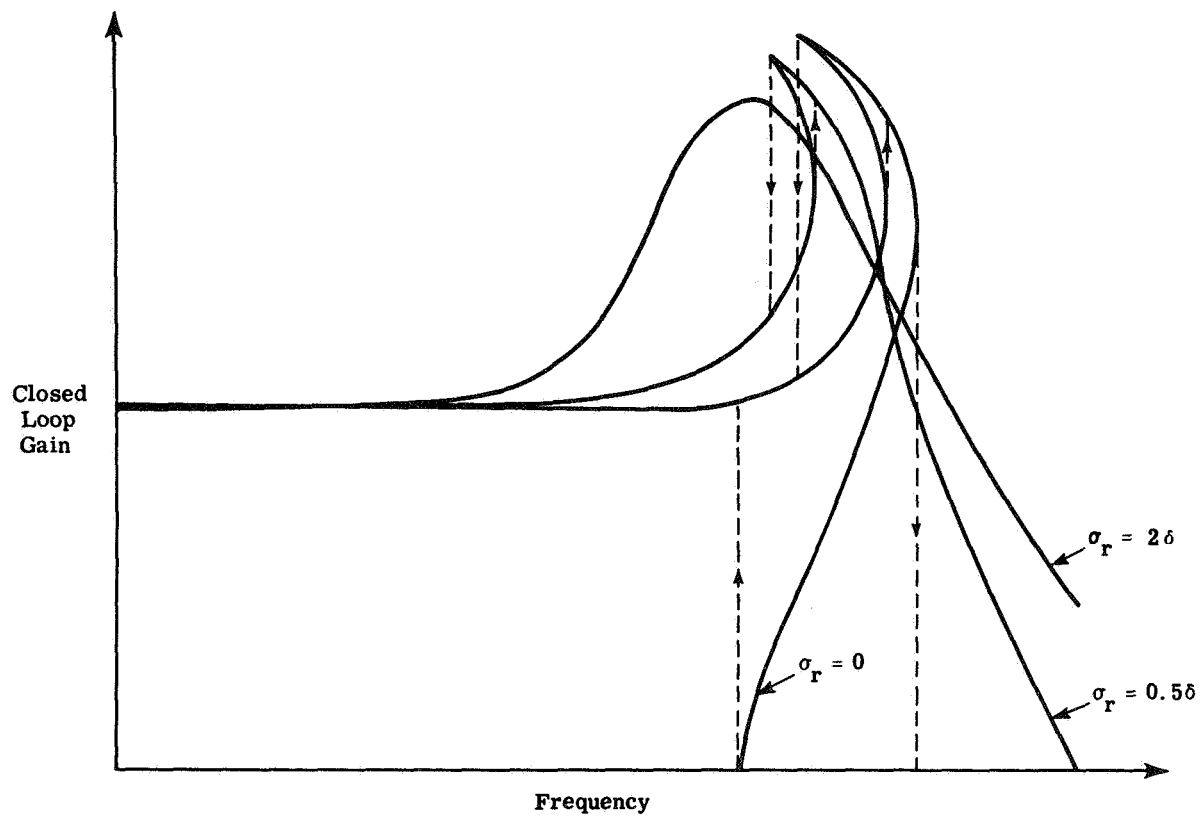


Figure 5.3-4 The Effect of σ_r on the Closed Loop Gain

SUMMARY

A hybrid simulation which will facilitate the study of errors in strapdown gyros and strapdown navigation systems is described. To begin with, the motivation for a strapdown gyro and error simulation is discussed. The form of the proposed simulation is presented, along with some reasons for rejecting other approaches to emulating strapdown gyro and system behavior. The section closes with a description of that portion of the hybrid simulation which computes a measure of system attitude error from errors at the outputs of the individual gyros.

6.1 MOTIVATION FOR A SIMULATION

The analysis and results reported in Ref. 1 and 2 are based on several assumptions and simplifications. Before proceeding with further work based on those results, it would be prudent to establish some check on the validity of these approximations. While simulation is not a perfect substitute for the construction and testing of hardware it is considerably less expensive and far more versatile. As an intermediate step between analysis and prototype construction, simulation is ideally suited to the present stage of the investigation. The value of simulation has already been well demonstrated in this report--on the basis of the comparisons obtained in Sections 4 and 5, the response characteristics of pulse rebalanced gyros using delta modulation torquing can be determined analytically with a considerable amount of confidence.

Other topics which were treated in an approximate manner in the above references include crosscoupling errors and random vehicle angular motions. When crosscoupling errors were computed in the case of oscillatory angular motion, the gimbal output angle was obtained from a linearized model for the binary pulse torqued gyro. The linear sensor approximation does not take into account the pulsed nature of the rebalance torque or float angles generated by limit cycling. In addition, treatment of crosscoupling errors in the ternary pulse torqued gyro is very difficult even with the aid of describing function techniques. Because of the non-linear nature of pulse rebalanced gyros, no confidence can be placed in the analysis of crosscoupling effects unless the results are substantiated by simulation.

In the portion of Ref. 1 dealing with gyro parameter optimization, several approximations and simplifications were made to permit easy calculation of gyro errors caused by random vehicle angular motions. Essentially, these assumptions involved the use of sinusoid transfer characteristics predicted by the analysis of Section 4 and 5 to compute errors induced by random vibrations. A simulation which generates realistic analogs of random angular motion about all major sensor axes is needed to check the assumptions.

Several questions which arose and were left generally unanswered in the preceding work can also be treated easily by a well designed simulation. In the discussion of strapdown gyro error compensation, the possibility of using the three basic gyros to measure angular motion for their own compensation is mentioned. Stability and accuracy analyses of this approach are very difficult to perform analytically because many closed loops, often containing time-varying gains, are generated. However, the technique is so attractive in terms of cost, power, weight and reliability that it must not be ignored. A well designed simulation of three gyros and

the compensation calculation will permit an empirical determination of the feasibility of this approach. In addition, simulation provides an inexpensive way of checking other proposed gyro error compensation schemes, including their sensitivity to the accuracy of various motion sensors.

In the work reported in Refs. 1 and 2, a system level figure-of-merit was developed to indicate the effect of gyro errors on strapdown system accuracy. Equations were derived relating the time histories of gyro errors to system attitude error. These expressions were exercised in the case of certain easily described gyro output errors (bias, white noise, oscillations, etc.) to give simple analytic relations between sensor and system drift rates. Whenever examples were presented and parameter optimization was illustrated, the latter relations were used rather than the original, more complex equations. The approximations which resulted should be substantiated by simulation.

In addition to verifying results from prior analyses, a well designed flexible simulation will be invaluable in the continuing study of strapdown sensors. Compensation within the gyro loop is easily analyzed and the effects of various torque generator characteristics on system errors can be studied. Test procedures for determining basic sensor error parameters can be evaluated. Using the simulation, dynamic test inputs can be designed and simulated information will be available for use in comparing different test data reduction techniques. Finally, the versatility and flexibility of a simulation must be emphasized. While the ultimate verification still lies in construction and testing of actual hardware, when it is desirable to investigate many proposed changes in gyro parameters only simulation provides an inexpensive and expedient means.

Description of the Projected Simulation - The simulation planned and under construction is illustrated in Fig. 6.1-1. Investigation indicates that a purely digital approach will be too slow if numerical integration is used to simulate the complex, high frequency dynamics to be considered. On the other hand, system error is to be computed using the error growth difference equations described in Ref. 2. This requires a digital computer. The hybrid simulation shown permits simultaneous determination of high frequency variables and accurate calculation of system error growth. Three gyros, including pulse rebalance torquing electronics, will be simulated on the analog portion along with random and deterministic motion in three dimensions, gyro motion-induced error torques and error compensation schemes. The gyro models will include structural dynamics when desired. Sensor outputs and true angular motion will be provided to the digital portion for calculation of system attitude errors. The simulation planned is a flexible tool for analyzing additional aspects of strapdown sensor errors. Gyro models can be changed to accommodate studies of exotic sensors and accelerometers can also be simulated.

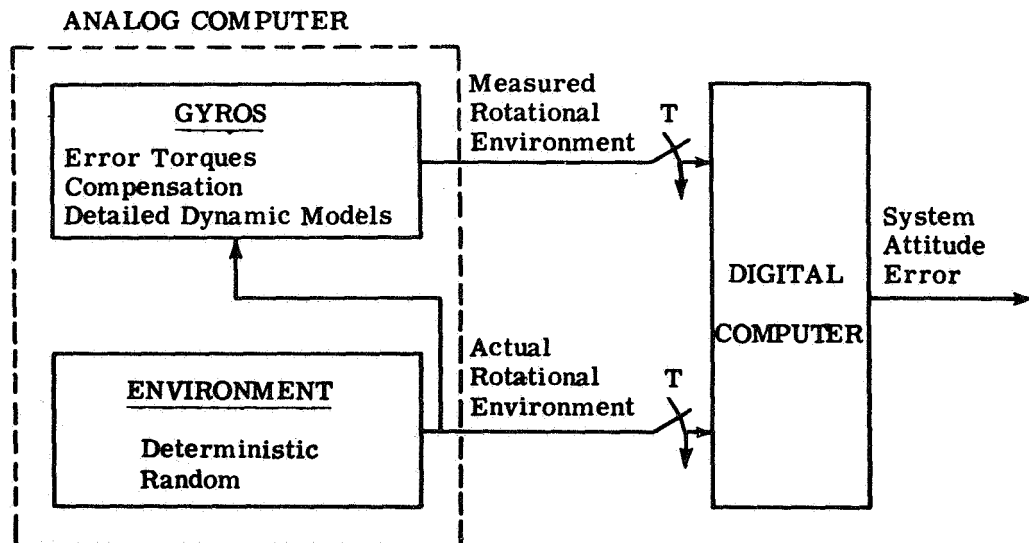


Figure 6.1-1 Hybrid Simulation of Gyros and Calculation of System Attitude Error

6.2 PROGRAM FOR THE DIGITAL PORTION

One function of an inertial navigation system is to provide an indication of vehicle orientation with respect to a reference coordinate frame. In strapdown systems this requirement is satisfied by computing a direction cosine matrix, C , relating vehicle and navigation reference frames. Given an initial C matrix, the direction cosines can be computed from the history of rotations about each body axis. If we compute C at discrete intervals T seconds apart, the direction cosines at the end of the $(n + 1)$ st interval can be expressed in terms of those at the end of the prior period and a matrix of incremental angles, $\Delta\theta$ (see Ref. 1). The matrix $\Delta\theta$ contains the angles through which the body axes have rotated since the last sample time. The equation relating the two direction cosine matrices is:

$$C_{n+1} = C_n e^{\Delta\theta_n} \quad (6.2-1)$$

when computer considerations such as quantization, word length and truncation are ignored. $\Delta\theta_n$ is defined by

$$\Delta\theta_n = \int_{nT}^{(n+1)T} \begin{bmatrix} 0 & -\omega_z & \omega_y \\ \omega_z & 0 & -\omega_x \\ -\omega_y & \omega_x & 0 \end{bmatrix} dt \quad (6.2-2)$$

where ω_x , ω_y and ω_z are the angular rates about the body axes. In practice the elements of $\Delta\theta_n$ are measured by the x, y and z-axis gyros.

Generally, there is a difference between the actual $\Delta\theta_n$ matrix and that obtained from gyro measurements. The difference between the actual $\Delta\theta_n$ matrix and that given by the gyros is a third matrix, E_n . The

presence of E_n results in an error, ΔC , in the C matrix computed from the gyro measurements. Given E_n for all values of n , we can compute ΔC at the end of each interval. A difference equation for ΔC which retains second order terms in small matrices is obtained from the series expansion of Eq. (6.2-1):

$$\Delta C_{n+1} \cong C_{n+1} \left(E_n + \frac{1}{2} (E_n)^2 \right) + \Delta C_n C_n^T C_{n+1} (I + E_n) \quad (6.2-3)$$

A figure-of-merit for gyro performance, p_n , can be computed from ΔC_n (see Ref. 1):

$$p_n = \frac{1}{2} \text{trace} (\Delta C_n^T \Delta C_n) \quad (6.2-4)$$

Description of the Program - At each sample time the digital computer portion of the simulation receives the simulated gyro outputs (pulse counts) and true body rotations (actual $\Delta \theta_n$ matrix) as inputs. The program then proceeds to compute E_n , C_{n+1} , ΔC_{n+1} and p_n . The matrices C_{n+1} and ΔC_{n+1} are stored for the next cycle and p_n is provided as an output. Figure 6.2-1 is a flowchart for the program. On this chart, C_0 and ΔC_0 are initial condition matrices for C and ΔC , respectively. The number n is the current number of compute cycles executed. This program has been run on a digital computer identical to the one to be used in the simulation. The compute cycle was found to be about 45 msec in duration. This constitutes a lower limit on the size of the sample period T if the digital computer is to process data when received and the analog simulation is not time scaled. The program was also checked out on an IBM QUIKTRAN time-sharing system. Simulated gyro error inputs in the form of ramps, sinusoids and coning motion were used. In every case the computer program output (p_n) agreed with the expected result. The program is considered ready for use.

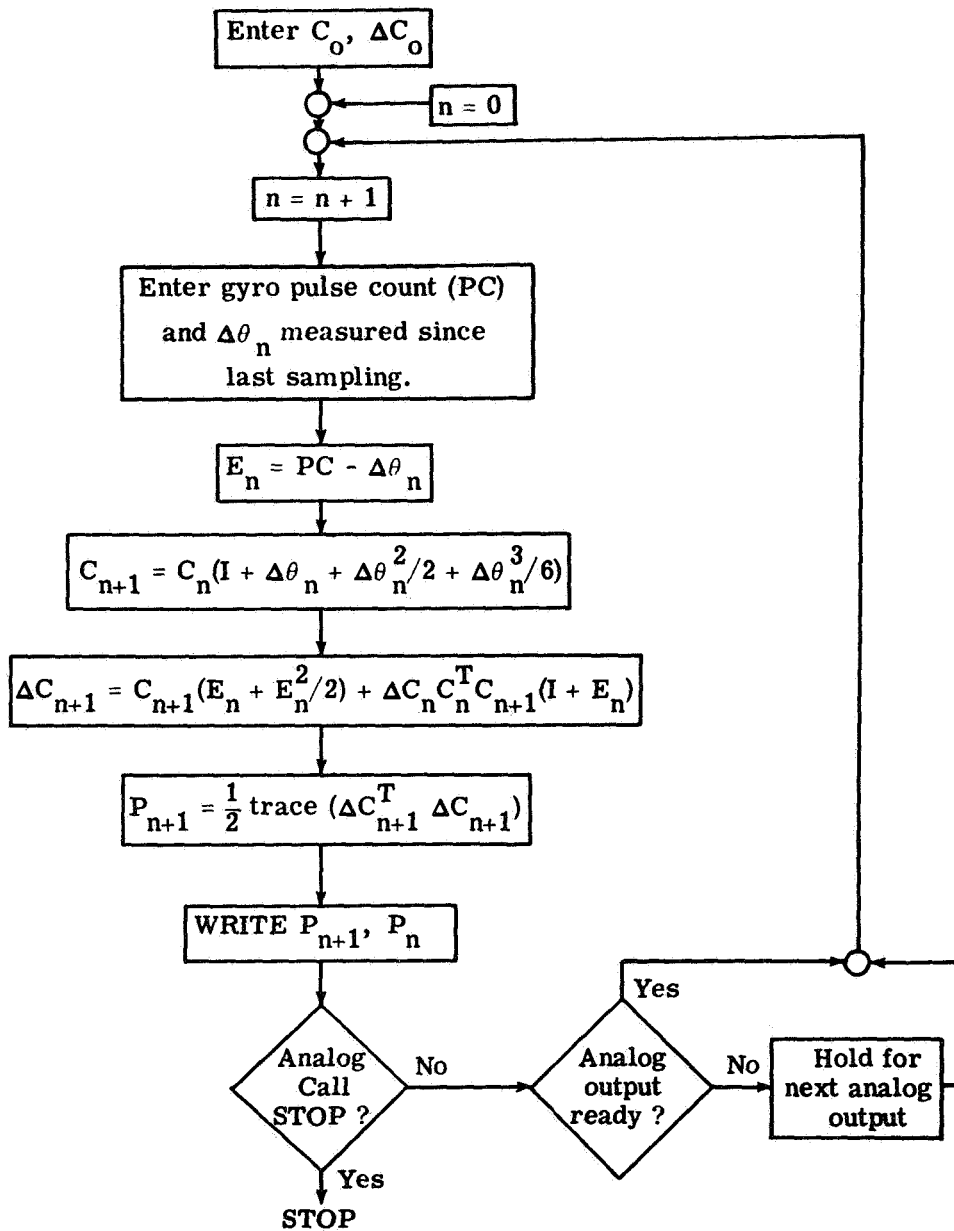


Figure 6.2-1 Flow Chart for the Digital Part of the Hybrid Simulation

7.1 CONCLUSIONS

Progress has been made in developing simple and accurate analytic descriptions of strapdown gyro behavior. A gyro employing binary delta modulation torquing was represented by a linear transfer function and the approximation was verified by simulation. The only time that a binary gyro is not well represented by a linear transfer function is when the limit cycle is extinguished by an input of sufficient frequency and amplitude. However, this situation is easily predicted by analysis and inputs required to quench the limit cycle are in any case unlikely. It was shown that gyros incorporating the time modulation rebalance scheme can also be represented by a linear transfer function.

Excellent agreement was found between the transfer characteristics predicted analytically for a ternary pulse rebalanced gyro and those experienced by simulation. The analysis in the case of the ternary gyro is more complex than for the other two sensors, reflecting in part the nonlinear nature of this gyro loop. The amplitude dependent nature of the ternary gyro response is well illustrated in Section 5.

The effects of complex dynamics within the gyro loop were accurately predicted analytically. The describing function techniques used throughout are capable of handling linear loop elements of any complexity. Consequently, including a linear model of rotor bearing compliance in the formulation of the analysis did not present any great difficulty. It was shown both analytically and by simulation that rotor bearing compliance

can alter gyro transfer characteristics significantly. However, it is still possible in the case of the binary gyro to represent the sensor response to sinusoidal inputs by a linear transfer function. Sampling within the gyro loop was also shown to reduce the instrument's bandwidth.

Most of the approximations regarding gyro loop behavior discussed in this report pertain to sinusoidal inputs only. To analyze the contribution of random vibrational motion to strapdown system errors it is necessary to describe the transmission characteristics of gyro loops when random inputs are applied. For gyros using binary delta modulated and time modulated torquing the answer seems to be a simple extension of the work reported above. Since the sinusoidal response of these two sensors is linear the same loop descriptions may suffice. The problem of developing a simple expression describing the propagation of random signals through a ternary gyro appears to be much more difficult; the effort required to investigate response to sinusoidal inputs is considerable and there is no reason to expect that random inputs will simplify the problem. The question of higher harmonics in the gyro output also remains; recall that the definition of frequency response involved only that component of gyro output which had the same frequency as the input. The problem of higher harmonics present in the square wave form of the gyro output must eventually be treated. In any case, the presence of these extra outputs does not in any way detract from the importance and validity of the excellent prediction of loop transfer characteristics demonstrated.

Finally, all of the results obtained this far relate to the gyro output. In order to compute crosscoupling errors the float angle response must be described. This will require additional, though probably not radically different, approximations to the behavior of nonlinear gyro loop.

7.2 CONTINUATION OF EFFORT

Development of the gyro error simulation will be the focus of future work. The time modulation gyro torquing scheme will be simulated and frequency response characteristics obtained will be compared with those predicted analytically. Consequently, it should be possible to verify the analytic description of this kind of gyro loop presented in Section 4 of this report. Analogs of motion-induced error torques will be applied to the gyro models to study the propagation of errors in the individual gyros and in a strapdown system. The sinusoidal-input transfer characteristics discussed in this report will be used to predict transmission of random signals through the gyros and simulation will be used to check the analysis. In this manner, it is expected that the linear approximations to the binary and time modulation torqued gyros will be certified for use in analysis of random vibration-induced errors.

The possibility of compensating environment-induced gyro errors by processing outputs from the basic sensor triad will be explored. Emphasis will be placed on compensation through corrective torquing but some effort will be devoted to the problem of compensating at the gyro output. It is anticipated that the accuracy potential of both these techniques will be determined by simulation in the near future. If certain aspects of gyro error compensation (for example, removing output axis angular acceleration errors) are shown to be unsatisfactory when only the gyro outputs are processed, the simulation study will be extended to cover the use of additional sensors.

Future analytic work will be directed toward describing the propagation of dynamic errors through a set of ternary pulse torqued gyros and into system misalignment. In particular, it is thought that crosscoupling errors in the ternary gyro may be treated by the

describing function approach. In brief, the future effort is expected to advance understanding of strapdown sensor errors and their reduction toward the point where it can be used as the basis for some hardware construction decisions.

APPENDIX A

GIMBAL MISALIGNMENTS CAUSED BY OUTPUT AXIS ANGULAR MOTION

A single-degree-of-freedom gyro experiences torques about its input axis which result from angular rates about the output axis. These torques misalign the float about the input axis, IA, to a degree which depends on the stiffness of the float suspension. Suspension stiffness together with the floatation fluid determine the time constant of the relative motion between case and float. In this section we analyze the time response of the float misalignment about IA to a step angular rate applied about the output axis, OA.

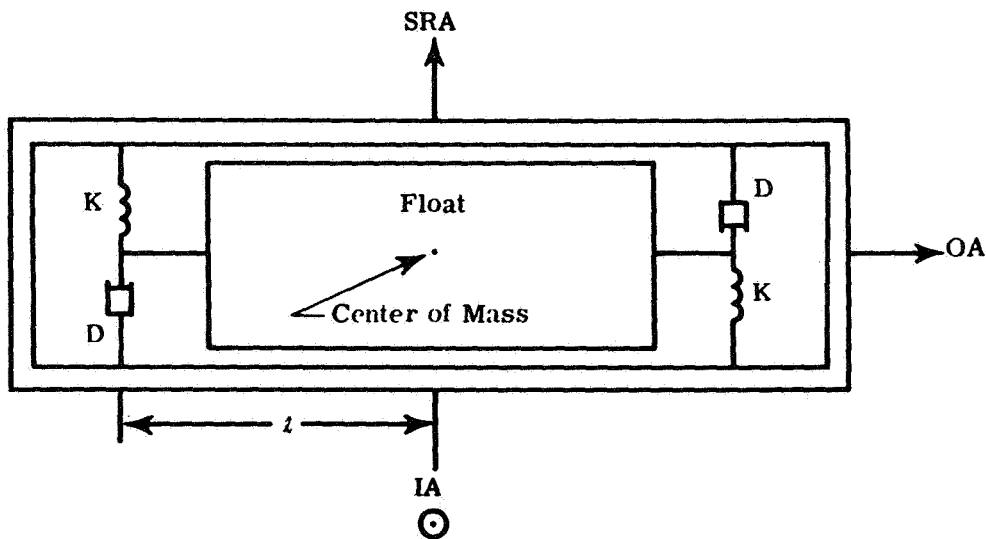


Figure A-1 Model for Gyro Case and Float Dynamics

Figure A-1 shows the model assumed for float dynamics about the input axis. The suspension stiffness is represented by linear springs and fluid damping by a pair of dashpots.

- α_i = Float-to-case angular misalignment about IA
- α_o = Float-to-case angular misalignment about OA
- ω_i = Case angular rate about IA
- ω_o = Case angular rate about OA
- I_{ii} = Float moment of inertia about IA
- H = Wheel angular momentum
- l = Distance between float center of mass and each float bearing in cm
- D = Equivalent linear damping constant in dyne-sec/cm
- C_i = Equivalent rotational damping constant in dyne-cm-sec
= Dl^2
- K = Equivalent linear spring constant in dyne/cm

The equation for angular motion of the float about IA is derived:

Torque on Float = Gyroscopic Torque - (Spring & Damper Reaction Torques)

$$= I_{ii} (\dot{\omega}_i + \ddot{\alpha}_i)$$

or

$$I_{ii} (\dot{\omega}_i + \ddot{\alpha}_i) = -H (\omega_o + \alpha_o) - 2Dl^2 \dot{\alpha}_i - 2Kl^2 \alpha_i \quad (A-1)$$

Simplifying, we have

$$-\frac{H}{I_{ii}} (\omega_o + \alpha_o) - \dot{\omega}_i = \ddot{\alpha}_i + 2\zeta\Omega_n \dot{\alpha}_i + \Omega^2 \alpha_i \quad (A-2)$$

where

$$\zeta = \frac{D \ell}{\sqrt{2 K I_{ii}}} \quad (\text{A-3})$$

$$= \frac{C_i}{\ell \sqrt{2 K I_{ii}}}$$

and

$$\Omega_n = \ell \sqrt{\frac{2K}{I_{ii}}} \quad (\text{A-4})$$

If we assume $\dot{\omega}_i$ and $\dot{\alpha}_0$ to be zero, Eq. (A-2) reduces to

$$\ddot{\alpha}_i + 2 \zeta \Omega_n \dot{\alpha}_i + \Omega_n^2 \alpha_i = - \frac{H}{I_{ii}} \omega_0. \quad (\text{A-5})$$

For most gyros the float motion is heavily damped and the response to a step of angular rate about OA can be accurately described by a single time constant, τ :

$$\alpha_i = - \frac{\omega_0}{\Omega_n^2} \left(\frac{H}{I_{ii}} \right) (1 - e^{-t/\tau}) \quad (\text{A-6})$$

$$\tau = \frac{1}{\Omega_n (\zeta - \sqrt{\zeta^2 - 1})} \cong \frac{C_i}{K \ell^2} \quad (\text{A-7})$$

Equations (A-3), (A-4), (A-6) and (A-7) are used to compute float misalignment behavior for different values of C_i and K . The fixed gyro parameters chosen are

$$\begin{aligned} H &= 2.5 \times 10^5 \text{ dyne-cm-sec} \\ l &= 3.6 \text{ cm} \\ I_{ij} &= 300 \text{ gm-cm}^2 \end{aligned}$$

Three plots are presented to assist the gyro designer in picking the appropriate suspension stiffness and damping coefficient to constrain misalignment about IA.

Figure A-2 shows the behavior of the float time constant, τ , as a function of K and C_i . Given τ we can enter Fig. A-3 and obtain a time history of the normalized float angle, $2l^2K\alpha_i/H\omega_0$. Note that any time constant obtained from Fig. A-2 implies $l=3.6$ cm. Figure A-4 allows us to obtain the misalignment angle as a function of time directly. The effect of suspension stiffness on the time response is readily observed.

If the suspension is not stiff enough for the range of expected output axis rates, the float pivots can strike the bearings. The resulting static friction between pivot and bearing surfaces provides a static break-out torque, τ_s , which masks small torques about the output axis caused by input angular rates. Accordingly, when the three-level torquer is used input rates smaller than τ_s/H are not seen at the sensor loop output, and the gyro has an effective rate deadzone. The force, F , pushing each pivot against its bearing results from the gyroscopic torque caused by an output axis angular rate and from forces applied by the gimbal suspension:

$$F = \frac{H\omega_0}{2l} - Kd$$

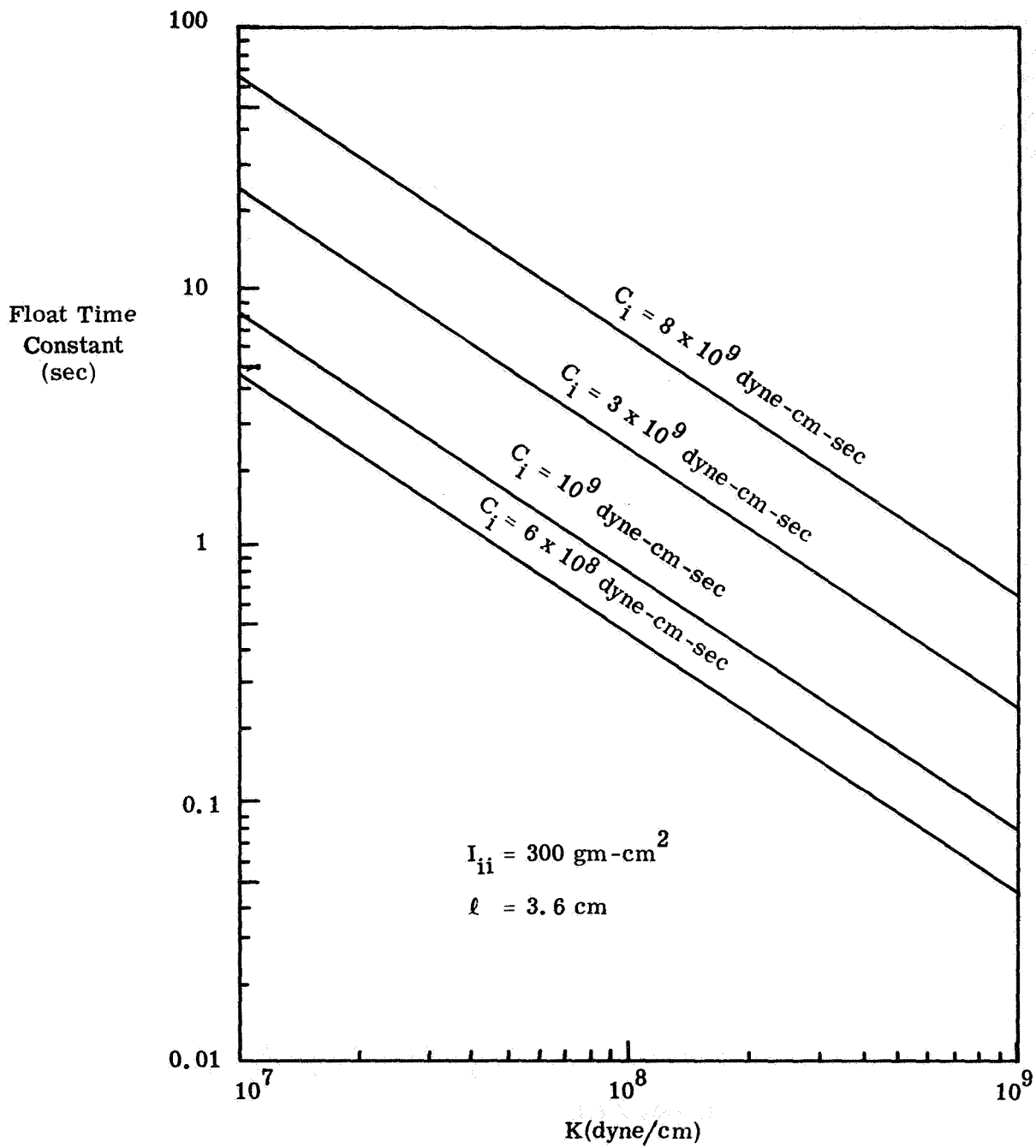


Figure A-2 Float Misalignment Time Constant as a Function of Suspension Stiffness K and Damping Constant C_i

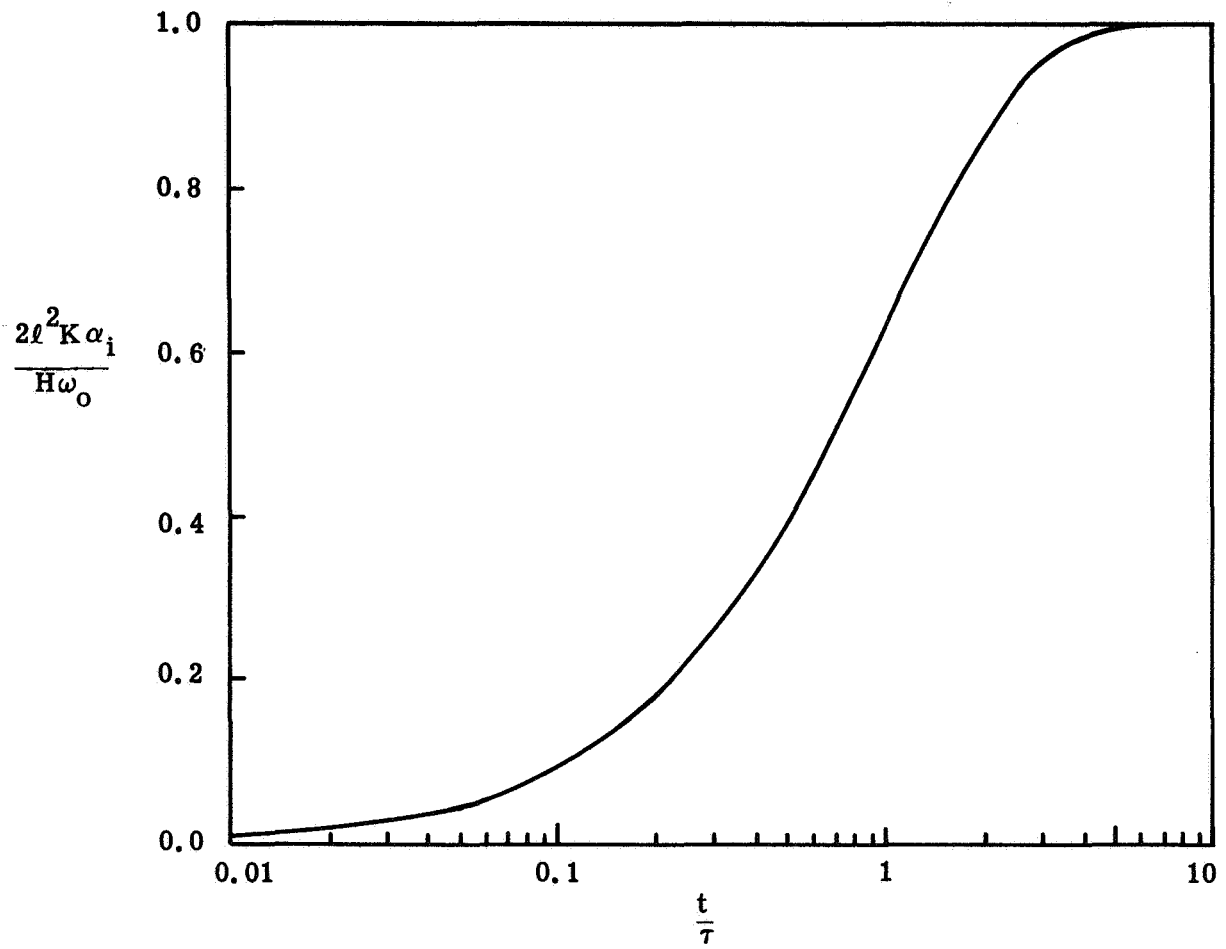


Figure A-3 Normalized Misalignment Angle Response to a Step Angular Rate About the Gyro Output Axis

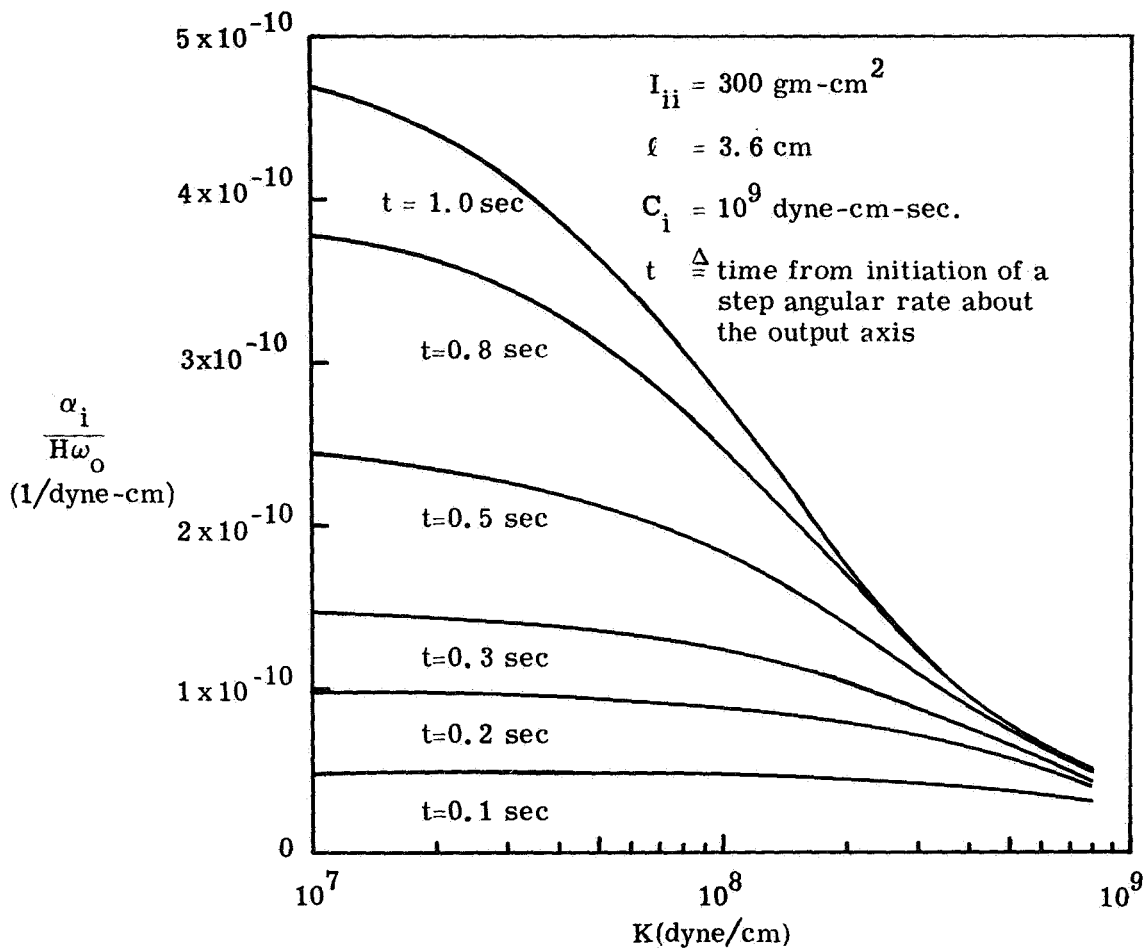


Figure A-4 Normalized Misalignment for Values of Suspension Stiffness

where d is the clearance between bearing and pivot. Knowing μ_{static} , an effective measure of static friction at the pivot-bearing interface, we can evaluate τ_s :

$$\begin{aligned}\tau_s &= 2\mu_{\text{static}}F \\ &= \mu_{\text{static}}\left(\frac{H\omega_0}{l} - 2Kd\right)\end{aligned}$$

The rate dead-zone corresponding to this break-out torque is

$$\pm \mu_{\text{static}}\left(\frac{\omega_0}{l} - \frac{2Kd}{H}\right)$$

In a binary gyro the constant application of torque by the torque generator prevents this dead-zone.

APPENDIX B

MOTION INDUCED ERRORS IN THE SINGLE-DEGREE-OF-FREEDOM PENDULOUS ACCELEROMETER

Errors introduced in the single-degree-of-freedom (SDF) pendulous accelerometer are discussed below. Whenever possible the error torque mechanisms are related to those given for the single-degree-of-freedom gyroscope in Ref. 1. Free use is made of both the derivations and discussions presented in the reference.

The SDF pendulous accelerometer is illustrated in Fig. B-1. Two major differences between this representation of the instrument and that presented for the SDF gyro are obvious. The direction perpendicular to the output and input directions is called the pendulum (p) axis rather than the spin (s) axis. Also, the instrument is assumed to consist of only two basic parts: a case and a combination gimbal and pendulum. The error torques induced in the SDF pendulous accelerometer by angular motion can be expressed by modifying the equations developed in Appendix A of Ref. 1. As a result of the instrument model shown in Fig. B-1, all terms in Eq. (A-19) of the reference which involve β_0 and β_i are dropped, and the subscript g is deleted because the gimbal and pendulum are considered as a single rigid body. The subscript p is substituted for s in the remaining terms. Also, since there is no spinning wheel involved in the accelerometer under consideration, all terms involving angular momentum, H, and the spin

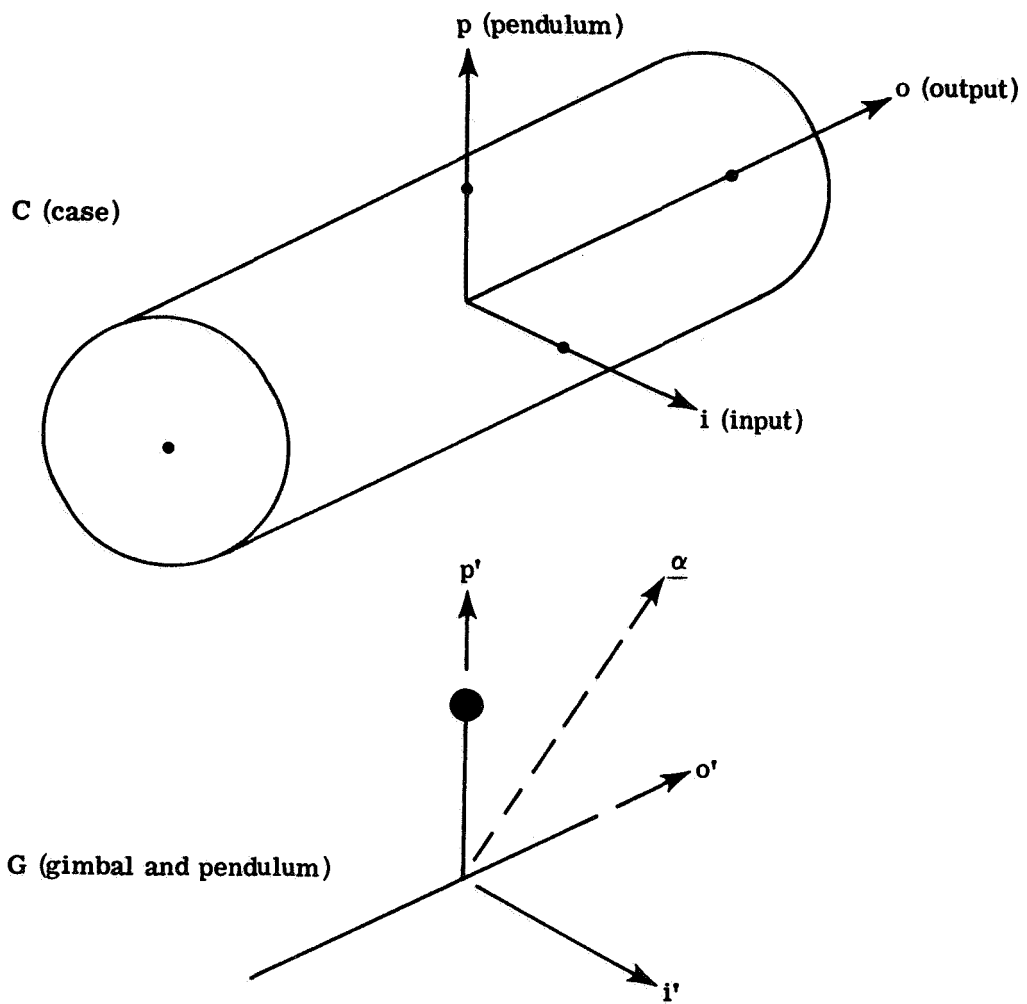


Figure B-1 Exploded View of Single-Degree-of-Freedom Pendulous Accelerometer Showing Small Misalignment Angle, α

rate of the rotor relative to the gimbal, Ω_s , are deleted. The resulting expression for output axis torques produced by angular motion is;

$$\begin{aligned}
 \left[M_f \right]_{o'} &= I_{oo} (\ddot{\alpha}_o + \dot{\omega}_o) + (I_{ii} - I_{pp}) \omega_p \omega_i + I_{op} (\dot{\omega}_p - \omega_o \omega_i) \\
 &+ I_{oi} (\dot{\omega}_i + \omega_o \omega_p) + I_{pi} (\omega_p^2 - \omega_i^2) \\
 &+ \alpha_o (I_{pp} - I_{ii}) (\omega_p^2 - \omega_i^2) \\
 &- \alpha_p \left[(I_{pp} - I_{ii}) \omega_o \omega_p + I_{oo} \dot{\omega}_i \right] \\
 &+ \alpha_i \left[(I_{pp} - I_{ii}) \omega_o \omega_i + I_{oo} \dot{\omega}_p \right] \tag{B-1}
 \end{aligned}$$

Since the ideal accelerometer is insensitive to angular motion, all of the terms in Eq. (B-1) must be considered as error torques in the SDF pendulous accelerometer. However, as in the case of the SDF gyro, the first term, $I_{oo} \ddot{\alpha}_o$, together with any damping torque about the instrument output axis, is usually considered as part of the unavoidable sensor dynamics and included in any "ideal" SDF pendulous accelerometer model. The remaining error terms can be divided into several broad categories similar to many exhibited by the gyro. Sensitivity to angular accelerations is present. The principal contribution, that caused by angular acceleration about the sensor output axis, is unavoidable because of the nature of the pendulous acceleration sensing instrument. Several anisoinertia terms also appear. Because the gimbal and pendulum of the accelerometer can be viewed as a rigid body, the opportunity exists to design an instrument which experiences no error torques from this cause. Finally, product of inertia terms appear in Eq. (B-1). The first of these terms can be larger than that experienced by a SDF gyro if the pendulum shown in Fig. B-1 deviates from the p' direction in the $o'-p'$ plane.

Linear Motion – Error torques generated by linear motion (acceleration) of the SDF pendulous accelerometer can be established using the error torque equation:

$$[\underline{M}_f]_{o'} = m(\underline{\delta} \times [\underline{a}]_G) \cdot o' \quad (B-2)$$

where m is the mass of the gimbal and pendulum combination, $\underline{\delta}$ is the vector of displacement between the gimbal-pendulum center of mass and the output axis expressed in gimbal coordinates, and $[\underline{a}]_G$ is the linear acceleration vector, similarly expressed. Notation will be as near to that of Section 2 and Appendix A of Ref.1 as possible. Acceleration expressed in the gimbal frame is related to that experienced in the case frame by:

$$[\underline{a}]_G = [\underline{a}]_C - \underline{\alpha} \times [\underline{a}]_C \quad (B-3)$$

Substituting Eq. (B-3) into Eq. (B-2), the output axis torque caused by the linear acceleration of a pendulous accelerometer is:

$$[\underline{M}_f]_{o'} = m\delta_p(a_i + \alpha_o a_p - \alpha_p a_o) - m\delta_i(a_p + \alpha_i a_o - \alpha_o a_i) \quad (B-4)$$

The effect of linear compliance on accelerometer errors can be illustrated by describing the center of mass displacement as a function of linear acceleration:

$$\begin{aligned} \delta_p &= m(K_{pi} a_i + K_{po} a_o + K_{pp} a_p) + \delta_{p0} \\ \delta_i &= m(K_{ii} a_i + K_{io} a_o + K_{ip} a_p) + \delta_{i0} \end{aligned} \quad (B-5)$$

Substituting Eq. (B-5) into Eq. (B-4), a more detailed torque equation results:

$$\begin{aligned}
 \left[\underline{M}_f \right]_{i_0} &= m \delta_{p_0} (a_i + \alpha_o a_p - \alpha_p a_o) \\
 &- m \delta_{i_0} (a_p + \alpha_i a_o - \alpha_o a_i) \\
 &+ m^2 \left[K_{pi} a_i^2 + K_{po} a_i a_o + (K_{pp} - K_{ii}) a_i a_p - K_{io} a_o a_p - K_{ip} a_p^2 \right]
 \end{aligned}
 \tag{B-6}$$

The first term of Eq. (B-6), $m \delta_{p_0} a_i$, measures linear acceleration along the input axis. This is the only output axis torque in the ideal pendulous accelerometer. The pendulosity $m \delta_{p_0}$ is designed into the instrument with care. All the remaining terms in this equation contribute errors to the accelerometer. The term $m \delta_{p_0} \alpha_o a_p$ is basically a cross-coupling error arising from rotation about the single axis of freedom and $m \delta_{p_0} \alpha_p a_o$ results from gimbal-to-case misalignment. Since accelerations along the input axis will cause considerable excursions of the gimbal angle, α_o , from null, sizeable rectification errors can be produced in this instrument by properly phased linear vibrations with components along the input and pendulum axes. The second line of Eq. (B-6) illustrates error torque contributions from unwanted mass unbalance and the last line expresses compliance error terms. It can be seen that linear compliance effects can produce constant error torques. The accelerometer is also subject to random error torques similar to those in an SDF gyro. The error in indicating linear accelerations along the case fixed input axis of an SDF pendulous accelerometer is simply the sum of all error torques, divided by the pendulosity, $m \delta_{p_0}$.

Rebalance Loop Errors - Errors in the single-degree-of-freedom pendulous accelerometer which result from the rebalance torquing mechanism are identical with those described for the SDF gyro in Section 2.4 of Ref. 1. The rebalance loop configurations commonly used are similar to those for the gyro and the input to the rebalance loop of either instrument can be viewed as a torque instead of an angular rate or a linear acceleration.

APPENDIX C

ACCURACY OF THE SMALL SIGNAL APPROXIMATION TO THE TWO-SINUSOID-INPUT DESCRIBING FUNCTION FOR THE BINARY NONLINEARITY

In Section 4.1 the Two-Sinusoid-Input Describing Function (TSIDF) gain of the binary nonlinearity is used. The describing function gain for a small signal sinusoid in the presence of a large limit cycle sinusoid is expressed there by the approximation:

$$N_B \cong \frac{2D}{\pi A} \quad (C-1)$$

where A is the limit cycle amplitude at the nonlinearity input and D is the relay drive (output) level. The describing function gain for the limit cycle in the presence of the small signal is given by

$$N_A \cong \frac{4D}{\pi A} \cdot \quad (C-2)$$

It is desirable to evaluate the accuracy of each approximation.

The required TSIDF's are given in Appendix D of Ref. 3. Denoting the amplitude of the small signal as B, where $B/A \triangleq \rho$, $\rho < 1$:

$$N_B(A, B) = \frac{8D}{\pi^2 B \rho} \left[E(\rho) - (1 - \rho^2)K(\rho) \right] \quad (C-3)$$

and

$$N_A(A, B) = \frac{8D}{\pi^2 A} E(\rho) \quad (C-4)$$

where

$$K(\rho) = \int_0^{\pi/2} \frac{d\psi}{\sqrt{1 - \rho^2 \sin^2 \psi}} \quad (\text{Elliptic Integral of the First Kind})$$

$$E(\rho) = \int_0^{\pi/2} \sqrt{1 - \rho^2 \sin^2 \psi} \, d\psi \quad (\text{Elliptic Integral of the Second Kind})$$

The percentage errors in TSIDF estimates caused by using the appropriate approximations are:

$$\begin{aligned} \% \text{ Error in } N_B &= \left| \frac{\text{Approximate Value of } N_B}{\text{Exact Value of } N_B} - 1 \right| \times 100 \\ &= 25 \left| \frac{\pi \rho^2 - 4 [E(\rho) - (1 - \rho^2)K(\rho)]}{E(\rho) - (1 - \rho^2)K(\rho)} \right| \end{aligned} \quad (C-5)$$

and

$$\begin{aligned} \% \text{ Error in } N_A &= \left| \frac{\text{Approximate Value of } N_A}{\text{Exact Value of } N_A} - 1 \right| \times 100 \\ &= 50 \left| \frac{\pi - 2E(\rho)}{E(\rho)} \right|. \end{aligned} \quad (C-6)$$

Note that these errors are function of ρ only. Figure C-1 shows the errors plotted as a function of ρ . As expected, the errors in the approximations vanish as the amplitude ratio ρ goes to zero.

$\rho = \frac{B}{A}$ where: B = Signal Amplitude Entering the Nonlinearity
A = Limit Cycle Amplitude Entering the Nonlinearity

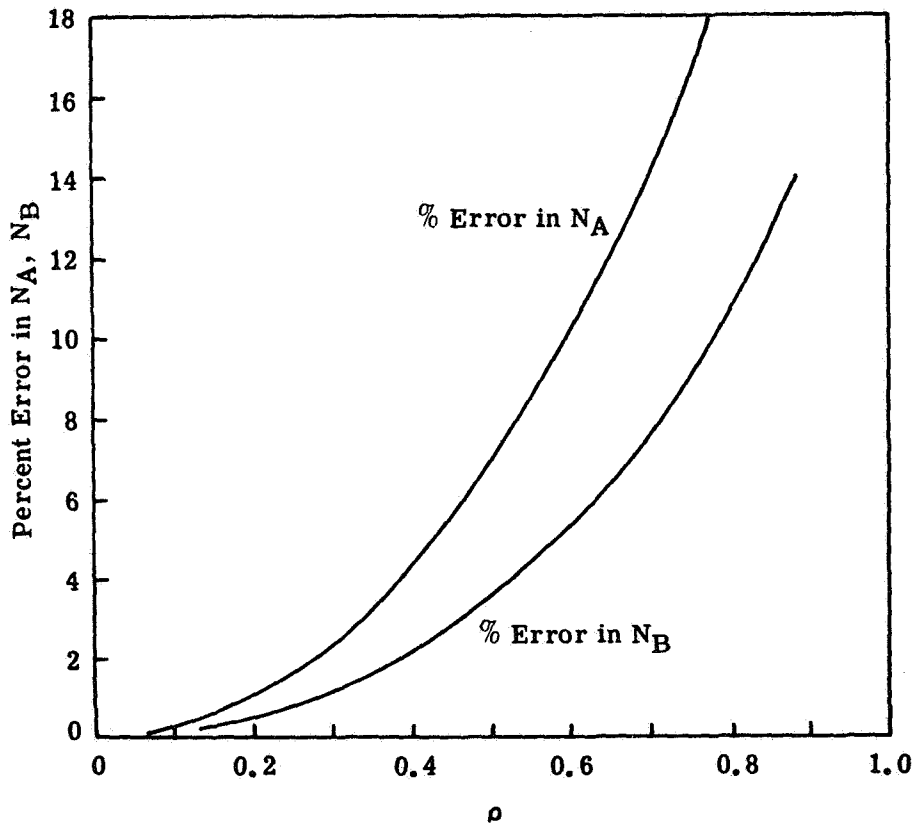


Figure C-1 Error in the Approximation to the TSIDF

APPENDIX D
LIMIT CYCLE QUENCHING
IN THE BINARY GYRO LOOP

When determining the limit cycle of a binary pulse rebalanced gyro, the nonlinearity can be replaced by an equivalent describing function gain, N_A . If both a signal, $B \sin \nu t$, and the limit cycle oscillation, $A \sin \omega_\ell t$, are present at the input to the nonlinearity, N_A remains essentially independent of the signal as long as $B \ll A$ (see Appendix C). In this appendix the influence of a large signal on the describing function gain to the limit cycle is considered. The material presented follows Ref. 3, Example 5.3-2.

If a limit cycle is to exist in a binary gyro, the following amplitude condition must be satisfied:

$$N_A |H(j\omega_\ell)| = 1 \quad (D-1)$$

where $H(s)$ is the open loop transfer function of the linear part of the gyro loop. The limit cycle frequency ω_ℓ is determined from the phase condition:

$$\angle H(j\omega_\ell) = -180^\circ \quad (D-2)$$

Several possible values for ω_ℓ may exist, but they are fixed for any given gyro. Consequently a limit cycle cannot exist if

$$N_A \leq \frac{1}{|H(j\omega_\ell)|} \quad (D-3)$$

for all possible values of ω_ℓ .

The describing function gain, N_A , of the binary nonlinearity is in general dependent on A and B. From the theory of Two-Sinusoid-Input Describing Functions (TSIDF's),

$$N_A(A, B) = \frac{8D}{\pi^2 A} E\left(\frac{B}{A}\right) \quad (D-4)$$

where D is the nonlinearity drive level, $A/B > 1$ and $E(B/A)$ is the complete elliptic integral of the first kind (see Ref. 3). Maximizing N_A over all values of A yields $N_{A_{\max}}$ as a function of B:

$$N_{A_{\max}} = \frac{0.855D}{B} \quad ; \quad \frac{B}{A} = 0.909 \quad (D-5)$$

Combining Eqs. (D-1) and (D-5), the value of the signal amplitude which causes the limit cycle to be "quenched," B_q , is found:

$$B_q = 0.855D \left| H(j\omega_\ell) \right| \quad (D-6)$$

The nonlinearity describing function gain to the signal when the limit cycle is quenched is found by substituting $B/A = 0.909$ into the relation for $N_B(A, B)$ given in Appendix C and employing Eq. (D-6):

$$\begin{aligned} N_B(A, B) \Big|_{B = B_q} &= \frac{2.089D}{\pi B_q} \\ &= \frac{0.778}{\left| H(j\omega_\ell) \right|} \end{aligned} \quad (D-7)$$

The binary torqued gyro loop can now be viewed as the system shown in Fig. D-1.

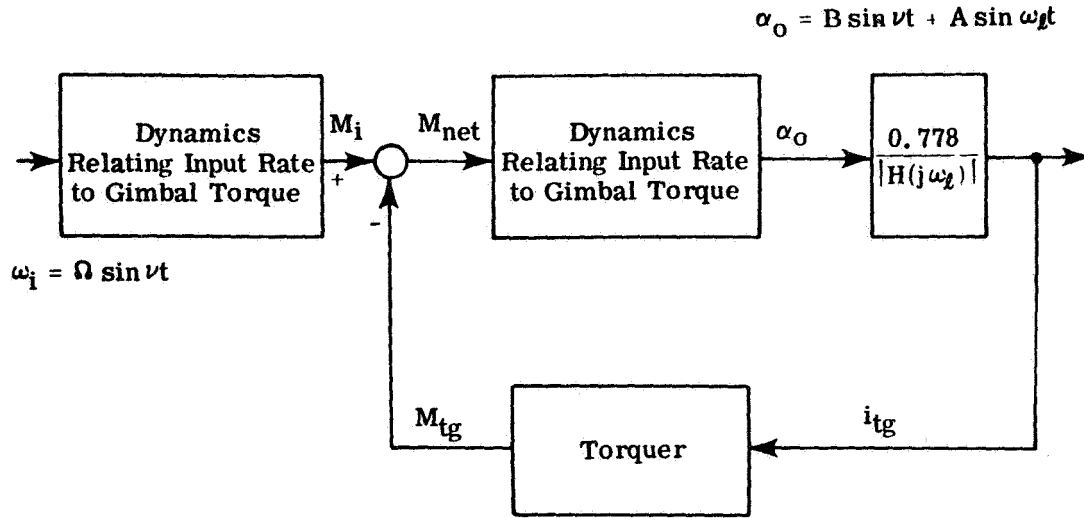


Figure D-1 Binary Loop Viewed at the Point where the Signal Quenches the Limit Cycle

In order to determine the values of input frequency and amplitude which cause the limit cycle to be quenched, the transfer function between input angular rate ω_i and float angle α_o is written in terms of the transfer function for the various blocks in Fig. D-1.

$$\frac{\alpha_o}{\omega_i}(s) = \frac{\frac{M_i}{\omega_i}(s) \frac{\alpha_o}{M_{net}}(s)}{1 + \frac{\alpha_o}{M_{net}}(s) \frac{M_{tg}}{i_{tg}}(s) N_B} \quad (D-8)$$

From Eqs. (D-6), (D-7) and (D-8), the solution for the input amplitude required to quench the limit cycle can be written:

$$\Omega_{\text{quench}} = \left. \left| \frac{\omega_i}{\alpha_o}(s) \right| B_q \right|_{s = j\nu} \quad (D-9)$$

$$= \left. \left| \frac{1 + \frac{\alpha_o}{M_{\text{net}}}(s) \frac{M_{\text{tg}}}{i_{\text{tg}}}(s) \frac{0.778}{|H(j\omega_\ell)|}}{\frac{M_i}{\omega_i}(s) \frac{\alpha_o}{M_{\text{net}}}(s)}} \right| 0.855D |H(j\omega_\ell)| \right|_{s = j\nu}$$

The most convenient way to display Eq. (D-9) is a plot of Ω_{quench} as a function of ν . For a particular set of parameters, a single-valued curve results, delineating the boundary between the regions where quenching does and does not occur. Figure D-2 indicates how limit cycle quenching helps determine the theoretical frequency response curve seen in Fig. 4.2-4 for the binary loop with simple gyro dynamics. The top half indicates the quenching curve for this system, showing the frequency where quenching occurs when a 0.1 rad/sec oscillatory input rate is applied. The resulting frequency response with the effects of quenching shown in the lower half of the figure. When the limit cycle is quenched, the loop output is a square wave at the signal frequency with an amplitude equal to the nonlinearity drive level. Torquer current is equivalent to 1 rad/sec. The fundamental component of the output has an amplitude of $4/\pi = 1.276$ rads/sec and the gain of the loop is $(1.276/0.1) = 12.76$. The effect of quenching is illustrated in Fig. D-3 for the loop with compliance dynamics discussed in Section 4.3.2.

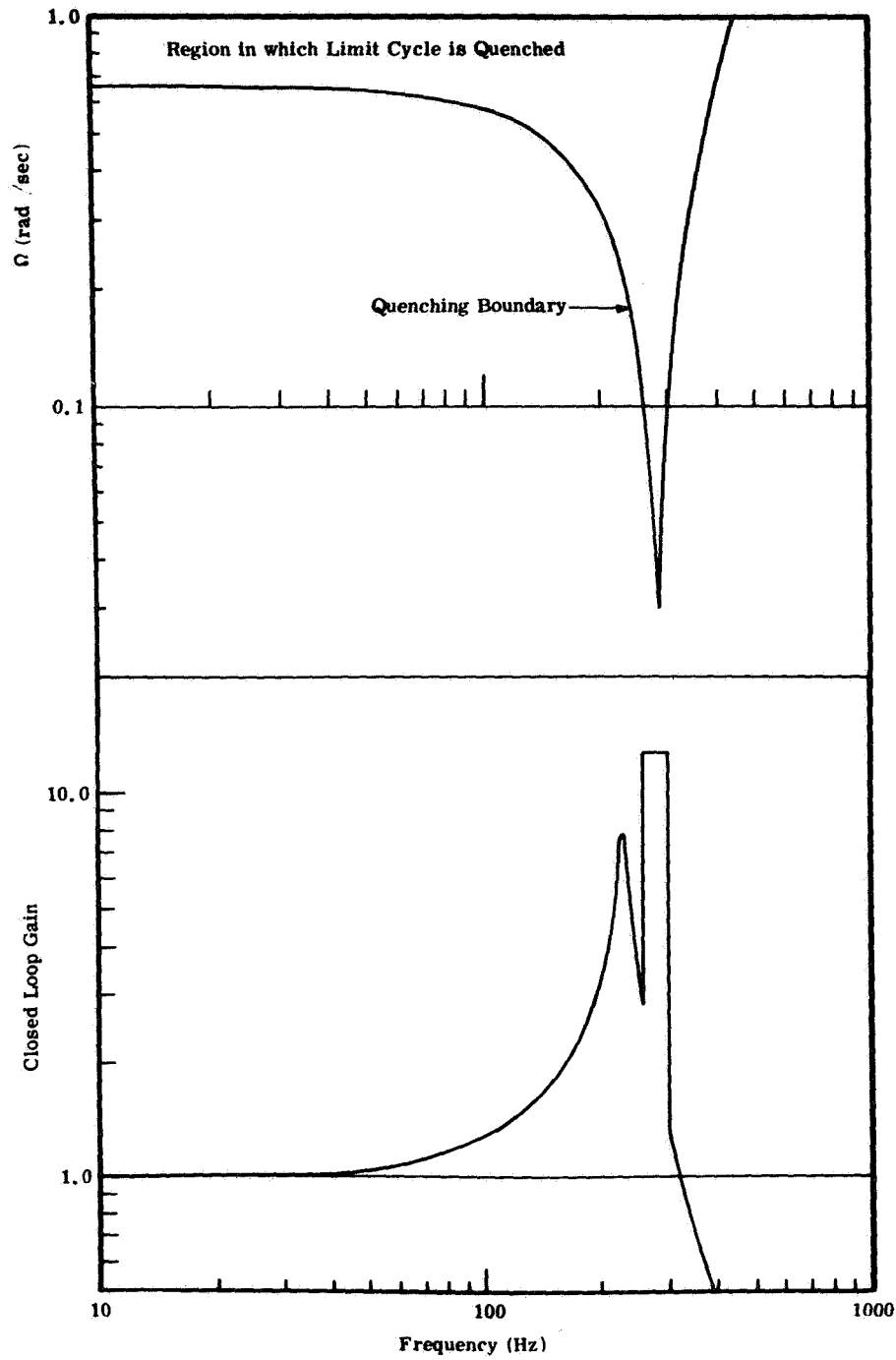


Figure D-2 **Limit Cycle Quenching and Its Effect on Frequency Response (Second Order Gyro Dynamics)**

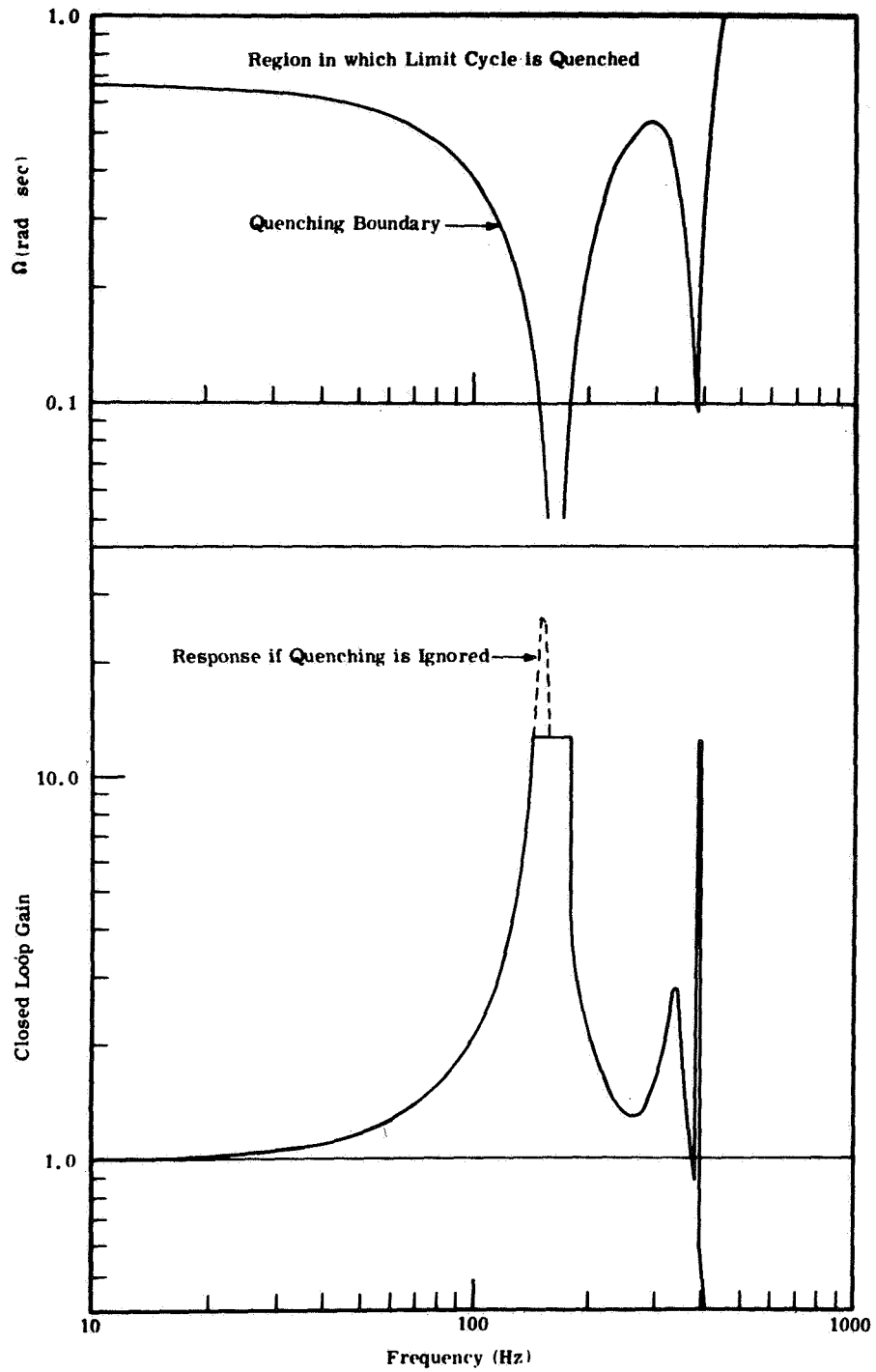
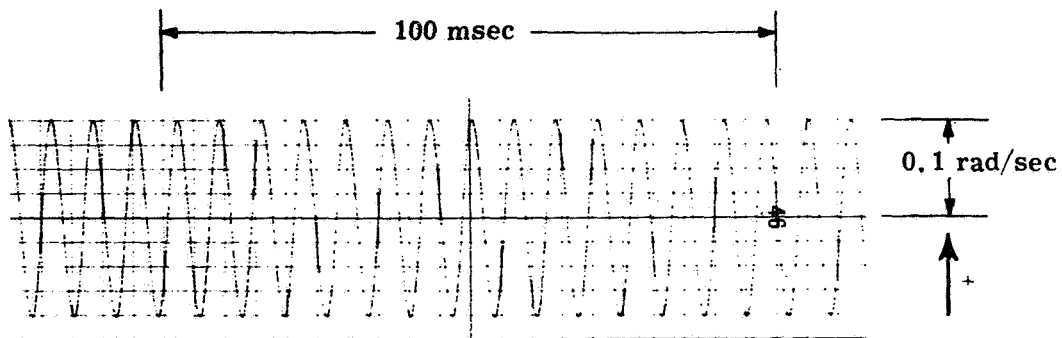


Figure D-3 **Limit Cycle Quenching and Its Effect on Frequency Response (Rotor Bearing Compliance Considered)**

Figure D-4 presents simulation records illustrating limit cycle quenching. The situation shown corresponds to suppression of the limit cycle as input frequency is increased to about 140 Hz, indicated in Fig. D-3. The frequency of ω_i was increased slowly but the change is not perceptible in the figure. Limit cycle quenching is seen as an abrupt change in loop behavior as reflected in the float angle.



(a) Input Angular Rate, ω_i



(b) Float Angle, α_o

Figure D-4 Binary Gyro Simulation Record Showing Limit Cycle Quenching

APPENDIX E

DERIVATION OF THE ELLIPSES USED IN DETERMINING THE FREQUENCY RESPONSE OF THE TERNARY GYRO LOOP

In analysis of the ternary pulse rebalanced gyro loop (see Sect. 5), a graphical solution is used. This is done by using two separate descriptions for the amplitude ratio between sinusoids on either side of the nonlinear element. One description, developed from linear analysis techniques, generates a family of ellipses. The equation for these ellipses is derived below.

Figure E-1 shows a generalized loop containing a single nonlinearity. N is an equivalent sinusoidal gain (describing function gain) for the nonlinearity and is assumed to involve no phase shift. The loop is driven by a sinusoid of constant amplitude, M , and frequency, ω . The amplitude of the transfer function between the signals $A \sin(\omega t + \phi)$ and $M \sin \omega t$ is:

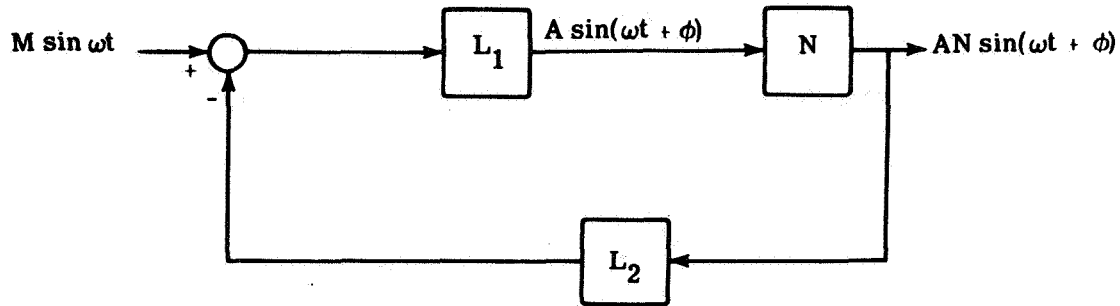
$$\frac{A}{M} = \left| \frac{\rho_1 e^{j\theta_1}}{1 + N\rho_1\rho_2 e^{j(\theta_1+\theta_2)}} \right| \quad (\text{E-1})$$

Using the identity

$$e^{j\theta} = \cos\theta + j\sin\theta \quad (\text{E-2})$$

Eq. (E-1) may be written as:

$$\frac{A}{M} = \frac{\rho_1}{\sqrt{(1+N\rho_1\rho_2\cos(\theta_1+\theta_2))^2 + N^2\rho_1\rho_2\sin^2(\theta_1+\theta_2)}} \quad (\text{E-3})$$



$$L_1 \triangleq \rho_1 e^{j\theta_1}$$

$$L_2 \triangleq \rho_2 e^{j\theta_2}$$

N = equivalent sinusoidal gain
of the nonlinearity

Figure E-1 A Loop Containing One Nonlinear Element

Squaring and cross-multiplying gives:

$$A^2(1+N\rho_1\rho_2\cos(\theta_1+\theta_2))^2 + A^2N^2\rho_1^2\rho_2^2\sin^2(\theta_1+\theta_2) = M^2\rho_1^2, \quad (\text{E-4})$$

Solving for the loop output amplitude, AN, we obtain

$$AN = \frac{-A\cos(\theta_1+\theta_2)}{\rho_1\rho_2} \pm \frac{1}{\rho_1\rho_2} \sqrt{M^2\rho_1^2 - A^2\sin^2(\theta_1+\theta_2)} \quad (\text{E-5})$$

In this expression M is given and $\theta_1, \rho_1, \theta_2, \rho_2$ are determined from the frequency ω . Thus, for fixed input amplitude and frequency we have a relation giving the amplitude of the nonlinearity output as a function of A, the amplitude

of its input. Note that AN is independent of the value of N . Plotting AN for values of A yields the ellipse shown in Fig. E-2. Critical points in the construction are illustrated.

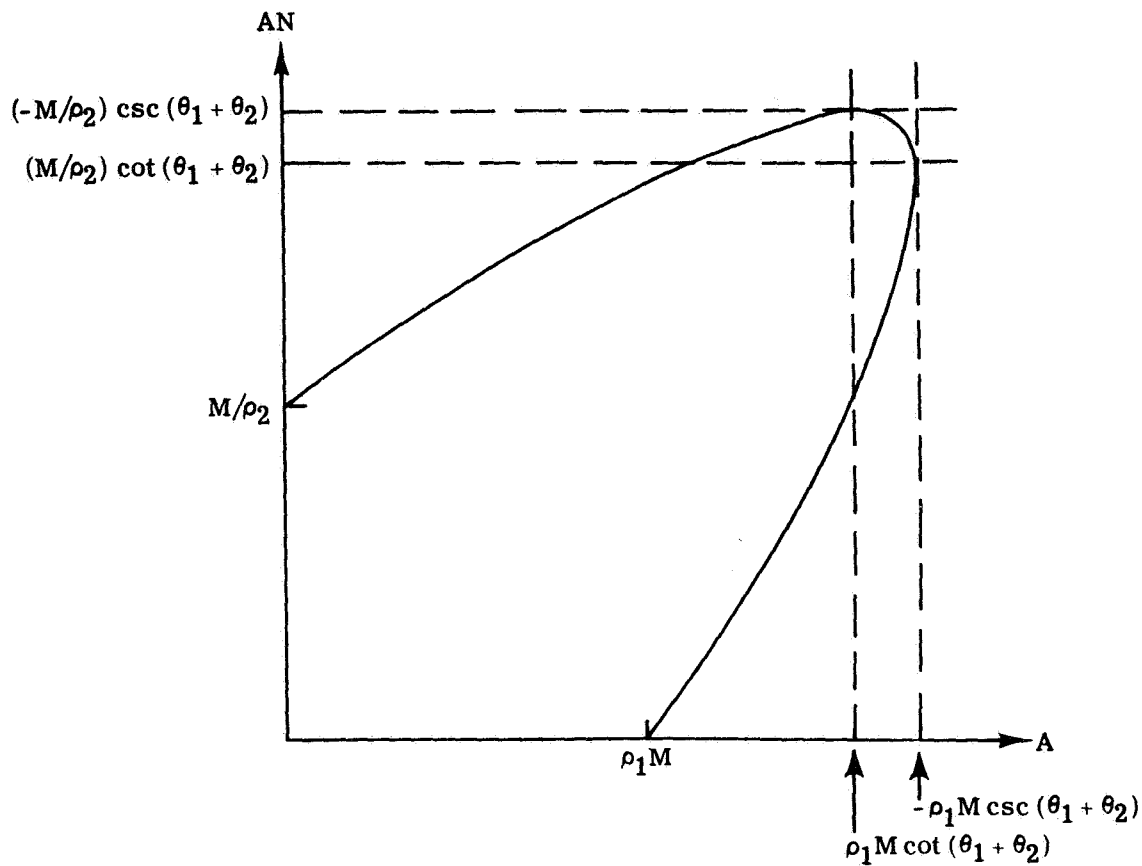


Figure E-2 Nonlinearity Input-Output Relation
 Derived from Analysis of the Linear
 Portion of the Loop Shown in Fig. E-1

APPENDIX F

SIMULATION OF GYROS WITH A SIMPLE REPRESENTATION OF DYNAMICS

This appendix describes simulation of binary and ternary pulse-torqued gyro loops where the single-degree-of-freedom gyros involved are characterized by second-order linear dynamic equations. All simulations were scaled to run at 1/100 real time. The basic signal flow diagram describing the gyros is given in Fig.F. 1-1. The simulations differ only in the form of the nonlinearity assumed. Appendix G describes the simulation of gyros with more complex dynamics.

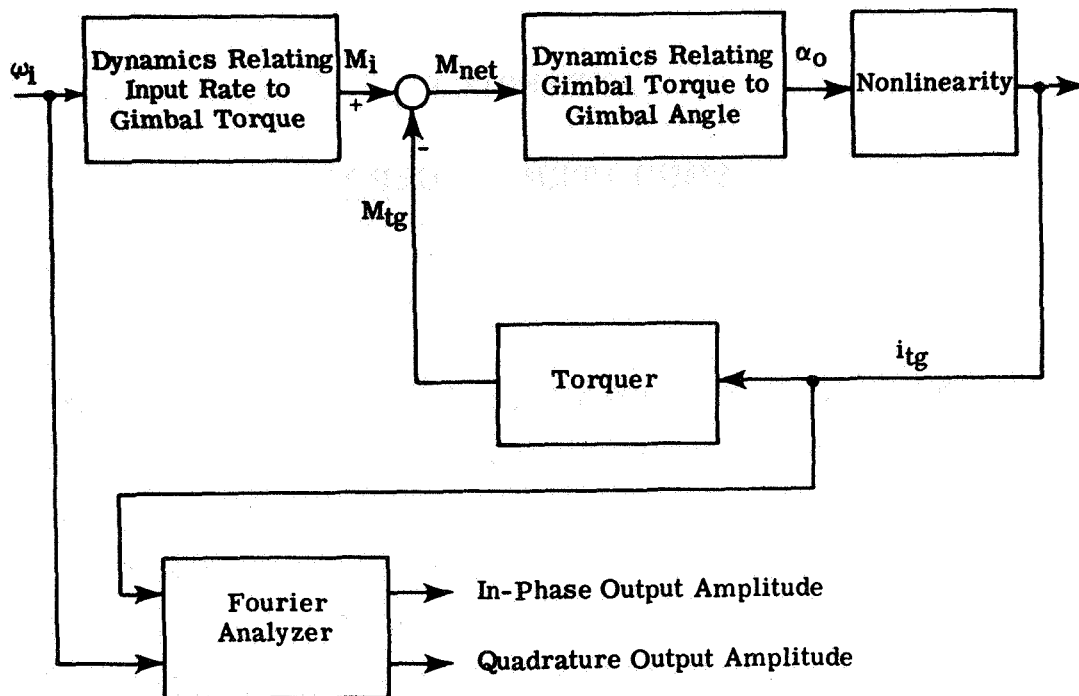
F.1 BINARY GYRO SIMULATION

When simulating the binary torqued loop with simple dynamics, certain blocks shown in Fig. 1.1-1 are represented by the following linear transfer functions:

$$M_i/\omega_i = H \quad \text{dyne-cm-sec/rad}$$

$$\alpha_o/M_{\text{net}} = \frac{k_{sg}}{sC(s\tau_f + 1)} \quad \text{mv/dyne-cm}$$

$$M_{tg}/i_{tg} = \frac{k_{tg}}{s\tau_{tg} + 1} \quad \text{dyne-cm/ma}$$



Definitions:

- ω_i = Input angular rate, in rad/sec
- M_{net} = Net torque about the gimbal output axis, in dyne-cm
- α_o = Signal generator output, in mV
- i_{tg} = Torquer current input, in mA
- M_{tg} = Torquer output, in dyne-cm
- M_i = Gyroscopic torque, in dyne-cm

Figure F. 1-1 Signal Flow Representation of Gyro Loop Simulation

nearly sinusoidal and has a large amplitude. The output amplitude, as indicated by the Fourier Detector, rises to $4D/\pi$ rads/sec, a value determined only by loop parameters, and is insensitive to further frequency changes.

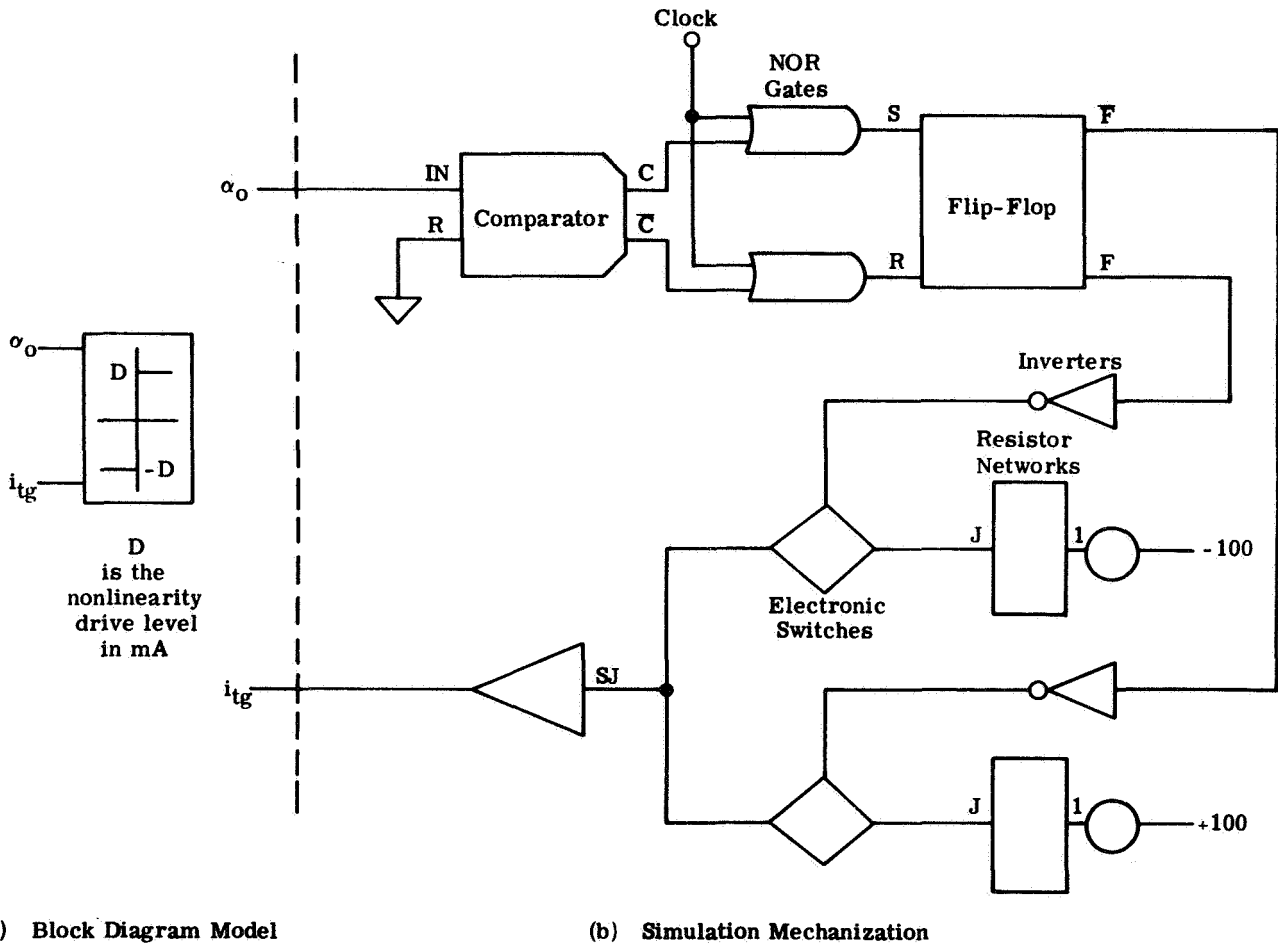


Figure F.1-3 Binary Nonlinearity Mechanization

For any given amplitude, critical points in the region of limit cycle quenching are given by four numbers. These are the frequencies at which the limit cycle is observed to be quenched and to reappear as the

input frequency is raised, and the corresponding points which occur when the frequency is lowered. The four points determine a region of jump resonance on the frequency response curves. When the input frequency is well above that of the limit cycle, the output of the Fourier Detector is quite noisy and difficult to read.

F.2 TERNARY GYRO SIMULATION

The basic difference between the binary and ternary rebalance loops is in the nonlinearity used; the linear transfer functions and the placement of elements within the loop are the same regardless of which torquing scheme is used. Accordingly, Fig. F.1-2 also describes the linear part of the ternary loop. Mechanization of the ternary nonlinearity is shown in Fig. F.2-1.

Before measuring the ternary loop frequency response, the discriminator level δ is lowered until limit cycling starts. The maximum value of δ causing oscillation and the oscillation frequency itself are compared with those obtained from describing function analysis. During the frequency response measurement, jump resonance appears as a sudden increase in float angle and Fourier Detector output for a small frequency change. As with the quenched binary loop, the gain changes associated with ternary jump resonance occur at frequencies which depend on the direction of approach. However, in the ternary gyro there is no region in which the gain is insensitive to frequency changes such as can occur during limit cycle quenching in the binary gyro. There is a frequency above which loop output ceases because the peak value of the float angle no longer exceeds δ . Once this frequency is exceeded, the loop output remains at zero unless the input frequency is lowered to a certain value where the output becomes non-zero again. The frequency of this second point is known

analytically but can be difficult to check by simulation because computer noise causes the float angle to drift. To remove this source of error, the input frequency was increased until the gyro output disappeared. The observed float drift rate was then corrected. When this procedure is followed, the loop output behavior is very close to that predicted by analysis.

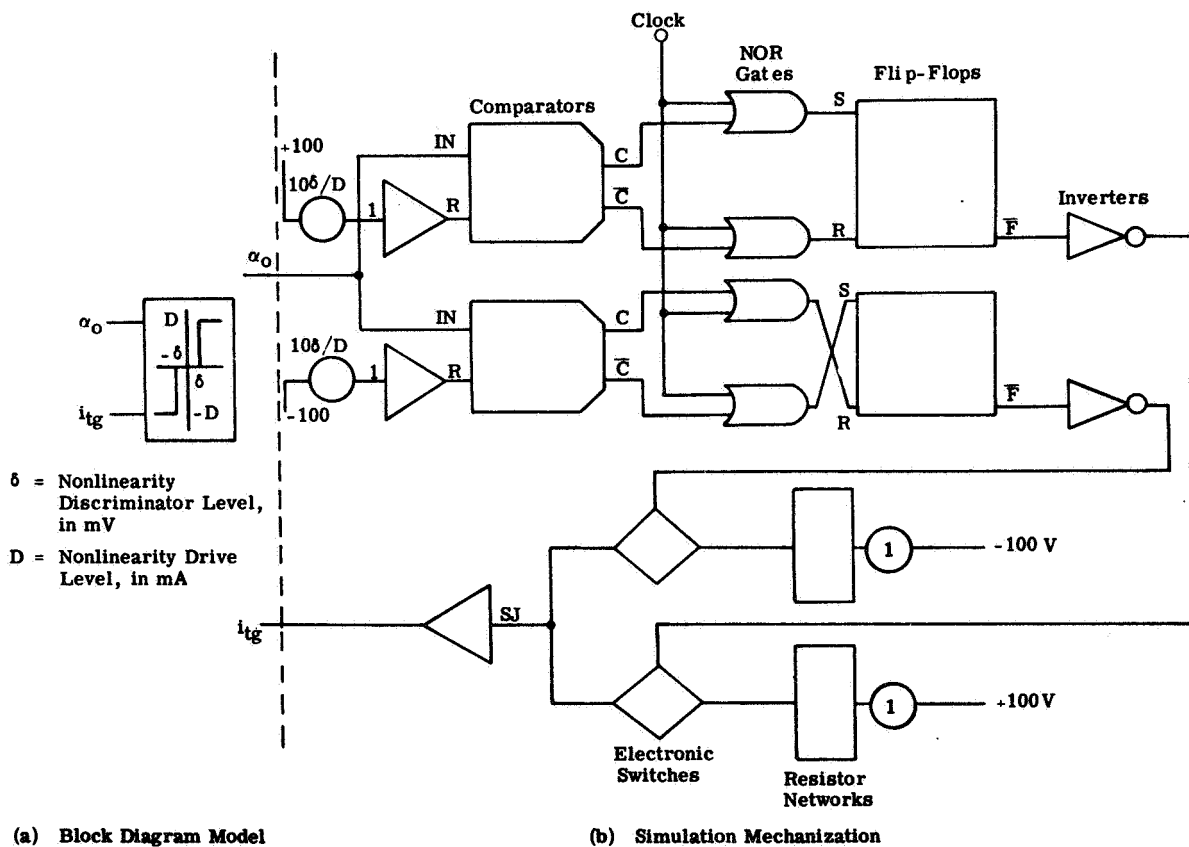


Figure F.2-1 Ternary Nonlinearity Mechanization

APPENDIX G

SIMULATION OF GYROS WITH ROTOR-TO-GIMBAL COMPLIANCE

The gyro simulations which take into account rotor-to-gimbal compliance are illustrated by the flow diagram of Fig. F.1-1. The torquer, nonlinearity and Fourier Analyzer portions of the simulations are identical with those described for simulating simpler models of pulse torqued gyros (see Figs. F.1-2, F.1-3 and F.2-1). Only the dynamic relations between M_i and ω_i and between α_o and M_{net} are treated in detail below. Practical considerations in obtaining frequency response curves are also discussed.

G.1 SIMULATION MODEL INCLUDING ROTOR-TO-GIMBAL COMPLIANCE

The transfer functions relating input angular rate, gimbal torque and gimbal angle, derived in Appendix I, are:

$$\frac{M_i}{\omega_i}(s) = \frac{-H(4\rho^2\nu_n^2s^2 + 4\rho\nu_n^3s + \nu_n^4)}{s^4 + 4\rho\nu_n s^3 + (2\nu_n^2 + 4\rho^2\nu_n^2 + \omega_g^2)s^2 + 4\rho\nu_n^3 + \nu_n^4} \quad (G.1-1)$$

$$\frac{\alpha_o}{M_{net}}(s) = \frac{1}{sI_{logg}} \frac{(s^4 + 4\rho\nu_n s^3 + [2\nu_n^2(2\rho^2 + 1) + \omega_g^2]s^2 + 4\rho\nu_n^3 + \nu_n^4)}{(s^5 + C_4s^4 + C_3s^3 + C_2s^2 + C_1s + C_0)} \quad (G.1-2)$$

where

$$C_4 \triangleq 4\rho\nu_n + \frac{d}{I_{00g}} + \frac{1}{\tau_f}$$

$$C_3 \triangleq 2\nu_n^2(2\rho^2 + 1) + \omega_g^2 + \frac{4\rho\nu_n}{\tau_f} + \frac{k}{I_{00g}} + \frac{2\rho\nu_nd}{I_{00g}}$$

$$C_2 \triangleq 4\rho\nu_n^3 + \frac{\omega_g^2}{\tau_f} + \frac{2\nu_n^2(2\rho^2 + 1)}{\tau_f} + \frac{2\rho\nu_nk}{I_{00g}} + \frac{d}{I_{00g}}(\nu_n^2 + \omega_g^2)$$

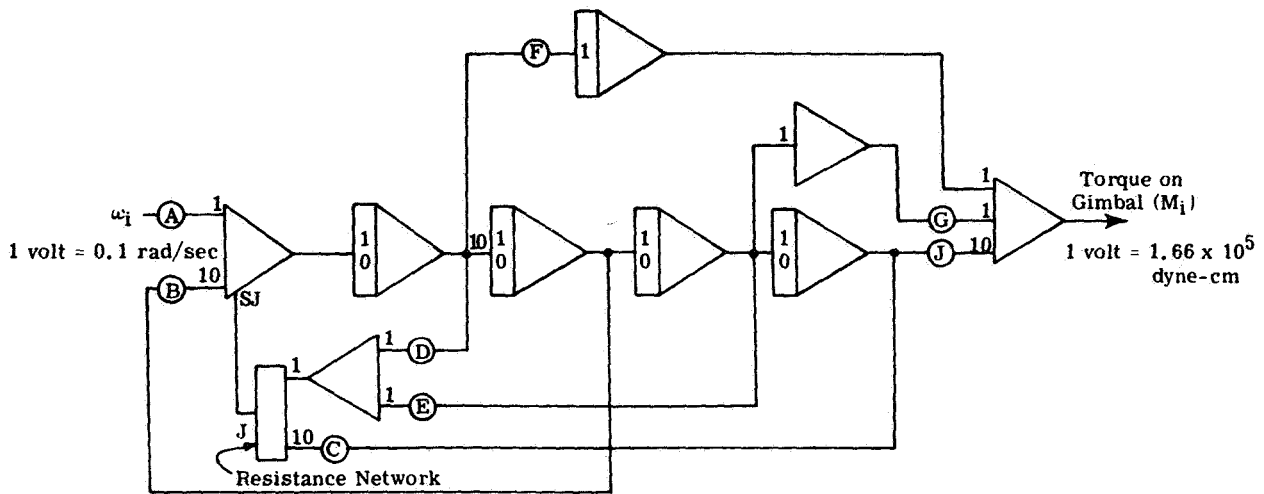
$$C_1 \triangleq \nu_n^4 \left(\frac{4\rho\nu_n^3}{\tau_f} + \frac{k}{I_{00g}}(\nu_n^2 + \omega_g^2) \right)$$

$$C_0 \triangleq \frac{\nu_n^4}{\tau_f}$$

The analog computer mechanization diagram for Eq. (G.1-1) appears in Fig. G.1-1. Appropriate potentiometer settings are given as algebraic quantities. Figure G.1-2 shows the mechanization diagram for Eq. (G.1-2). Figure G.1-3 is included to illustrate analog computer scaling of important signals in the simulation.

G.2 BINARY GYRO SIMULATION

The binary loop with simple dynamics characteristically limits cycles at a single frequency because there is only one point at which the open loop phase shift is -180° . When rotor-to-gimbal compliance is considered, there can be more modes, usually three, each one characterized by a different frequency and amplitude. It is shown in Section 4.1 that the limit cycle frequency determines the gain of the nonlinearity to the signal.



Potentiometer Values:

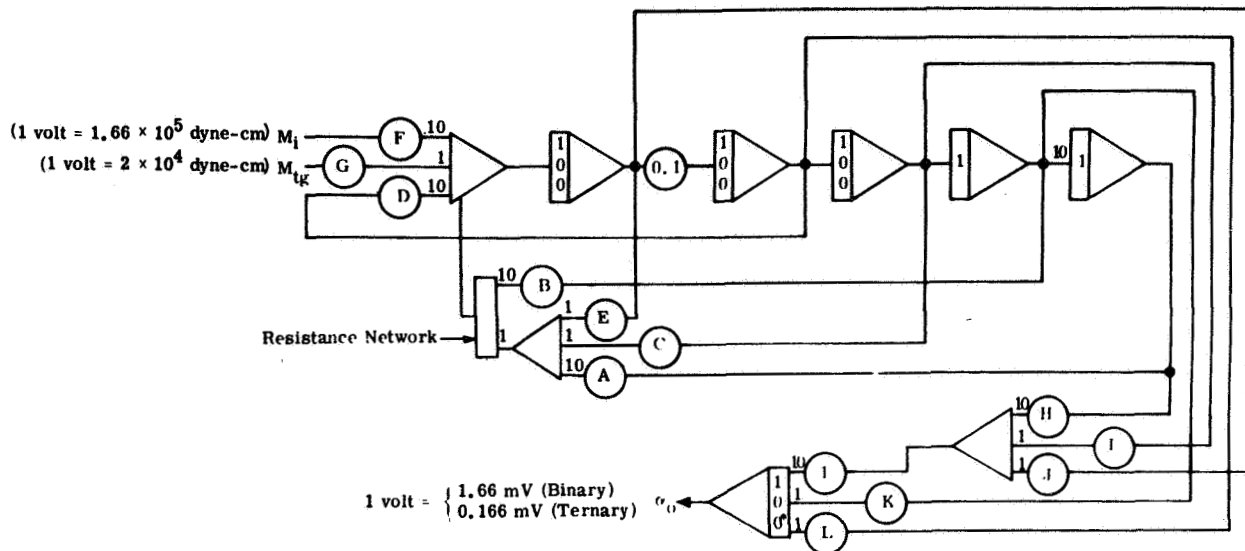
$$A = \frac{H}{166 \times 10^4} \qquad E = \frac{4\rho\nu_n^3}{10^{10}}$$

$$B = \frac{2\nu_n^2(2\rho^2 - 1) + \omega_{zg}^2}{10^8} \qquad F = \frac{4\rho^2\nu_n^2}{10^5}$$

$$C = \frac{\nu_n^4}{10^{14}} \qquad G = \frac{4\rho\nu_n^3}{10^{10}}$$

$$D = \frac{4\rho\nu_n}{10^3} \qquad J = \frac{\nu_n^4}{10^{14}}$$

Figure G. 1-1 Mechanization Diagram for Eq. (G. 1-1)



Potentiometer Values:

$$A = (\nu_n^4 / r_f) \times 10^{-17}$$

$$B = (\nu_n^4 \cdot \frac{4\rho\nu_n^3}{r_f} \cdot \frac{k}{I_{00g}} (\omega_g^2 \cdot \nu_n^2)) \cdot 10^{-14}$$

$$C = (4\rho\nu_n^3 \cdot \frac{\omega_g^2}{r_f} \cdot \frac{2\nu_n^2 (2\rho^2 + 1)}{r_f} \cdot \frac{2\rho\nu_n k}{I_{00g}} \cdot \frac{d}{I_{00g}} (\nu_n^2 \cdot \omega_g^2)) \times 10^{-11}$$

$$D = (2\nu_n^2 (2\rho^2 + 1) + \nu_n^2 \cdot \frac{4\rho\nu_n}{r_f} \cdot \frac{k}{I_{00g}} + \frac{2\rho\nu_n d}{I_{00g}}) \times 10^{-8}$$

$$E = (4\rho\nu_n \cdot \frac{d}{I_{00g}} \cdot \frac{1}{r_f}) \times 10^{-4}$$

$$F = K_{Sg} \times 10^{-5}$$

$$G = K_{Sg} K_{I_g} \cdot 10^{-8}$$

$$H = (\nu_n^4 I_{00g}) \cdot 10^{-12}$$

$$I = ((2\nu_n^2 (2\rho^2 + 1) \cdot \omega_g^2) \cdot I_{00g}) \cdot 10^{-6}$$

$$J = 10 I_{00g}$$

$$K = (4\rho\nu_n^3 / I_{00g}) \cdot 10^{-7}$$

$$L = (4\rho\nu_n / I_{00g}) \cdot 10^{-1}$$

* Gain = 10 for binary simulation.

Figure G. 1-2 Mechanization of Eq. (G. 1-2)

Consequently, if the limit cycle switches to a new mode, the loop characteristics as seen by the input signal can be radically altered. The loop has a different closed loop frequency response for each limit cycle mode encountered.

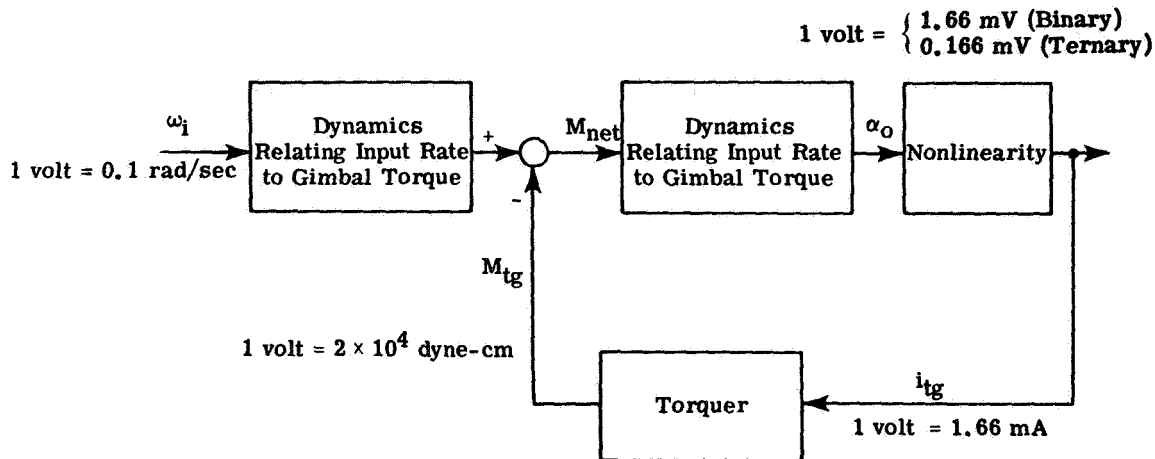


Figure G. 1-3 Computer Scaling Used in Simulation of Gyros with Rotor-to-Gimbal Compliance

Before a frequency response simulation is made, all possible limit cycle modes are determined analytically. One check of the simulation is to verify the existence of the calculated limit cycle modes. In this manner information is obtained on how the loop must be stimulated in order to make the various modes appear. After the simulation has been verified as a true representation of the loop dynamics, a particular limit cycle mode is obtained and the frequency response for this mode is measured. During the measurement care must be exercised to avoid those frequency regions where different modes may be excited. This procedure is repeated until all modes have been considered.

An additional characteristic appears, caused by the lightly damped complex poles of Eq. (G. 1-1), when rotor-to-gimbal compliance is considered. As the input frequency nears the lower of the two pole frequencies, the input torque applied to the gyro loop increases until it reaches a level sufficient to quench the limit cycle. A peak in the frequency response occurs when this condition is reached. For the system dynamics considered to date, this response peak occurs at a lower frequency than any resonance attributable to the dynamics of the gyro torque loop. Since the usable frequency range of most gyro loops consists of the region below the first gain peak, there is little need, given the present dynamics, to examine the region above the first pole frequency. Thus, in the present case the important part of the closed loop frequency response is determined by rotor-to-gimbal compliance characteristics and not by the float and torquer time constants.

G. 3 TERNARY SIMULATION CONSIDERING COMPLIANCE

Most of the discussion in Appendix F concerning the ternary simulation applies when rotor-to-gimbal dynamics are considered. The discriminator level δ is lowered in the simulation until the loop starts to limit cycle. The limit cycle mode(s) thus obtained are checked against those predicted by analysis. If the modes are as predicted the simulation represents the desired dynamics. As with the binary loop (Section G. 2), a pole of Eq. (G. 1-1) causes a peak which dominates the closed loop frequency response of the ternary loop. The only difference is that the peak is characterized by jump resonance rather than by quenching.

APPENDIX H

THE FOURIER ANALYZER

One problem encountered in measuring the sinusoid frequency response of the pulse rebalanced gyro loop is that the loop output is not a sinusoid. The loop output is taken at the output of the nonlinearity; it consists of a series of rectangular pulses. When an input of the form $A \sin \omega t$ is applied to the loop, the loop output y is of the form

$$y = B_1^s \sin \omega t + B_1^c \cos \omega t + \sum_{n=2}^{\infty} (B_n^s \sin n\omega t + B_n^c \cos n\omega t). \quad (\text{H-1})$$

There is no constant term at the output because the input is assumed to be an unbiased sinusoid and no rectification takes place within the loop. The loop transfer function evaluated at the frequency ω is defined by the equation:

$$\text{Loop Transfer Function} = \frac{\text{Phasor Rep. of the Output Component at Freq. } \omega}{\text{Phasor Representation of the Input (Freq. } \omega)}$$

$$= \frac{\sqrt{(B_1^s)^2 + (B_1^c)^2}}{A} \angle \tan^{-1} \left(\frac{B_1^c}{B_1^s} \right). \quad (\text{H-2})$$

It is necessary to measure the amplitudes B_1^S and B_1^C of the in-phase and the quadrature components at frequency ω in order to calculate the closed loop transfer function at that point.

H.1 ANALYZER OPERATING PRINCIPLES

The Fourier analyzer operating concept is based in part on the following two identities:

$$\sin^2 \theta = \frac{1}{2} (1 - \cos 2\theta) \quad (\text{H-3})$$

$$\cos^2 \theta = \frac{1}{2} (1 + \cos 2\theta) \quad (\text{H-4})$$

If the gyro output is multiplied by $A \sin \omega t$, the result is as follows:

$$\begin{aligned} y A \sin \omega t &= \sum_{n=1}^{\infty} \left(B_n^S A \sin \omega t \sin n\omega t + B_n^C A \sin \omega t \cos n\omega t \right) \\ &= B_1^S A \sin^2 \omega t + B_1^C A \cos \omega t \sin \omega t + \dots \\ &= \frac{B_1^S A}{2} + \text{oscillatory terms} \end{aligned} \quad (\text{H-5})$$

All terms except the constant term have zero average values. Accordingly, if the product is time averaged over an integer number of cycles at frequency ω , the result is:

$$\overline{y A \sin \omega t} = \frac{B_1^S A}{2} \quad (\text{H-6})$$

where the bar denotes time averaging. Solving for B_1^S gives

$$B_1^S = \frac{2}{A} \overline{y A \sin \omega t} \quad (\text{H-7})$$

If the output y is multiplied by $A \cos \omega t$ (the input phase shifted 90°) and time averaged, a similar argument can be used to show that

$$B_1^C = \frac{2}{A} \overline{y A \sin \omega t} \quad (\text{H-8})$$

The conceptual operation of the Fourier Analyzer is shown in block diagram form in Fig. H.1-1. Since the required 90° phase shift is achieved using an integrator, the output of the quadrature component multiplier is the desired quantity divided by ω .

H.2 FOURIER ANALYZER MECHANIZATION

The analog computer mechanization diagram for the Fourier Analyzer is shown in Fig. H.2-1. The analyzer is scaled in such a way that if $A = 1$ volt, the in-phase output component is one volt when the gyro loop is producing unity closed loop gain with no phase lag. Since the input scaling is 1 volt = 0.1 rad/sec, the amplitude of the in-phase component B_1^S in rad /sec can be computed:

$$(B_1^S)_{\text{rad/sec}} = \frac{1}{10} \left(\frac{\text{In-Phase Output Component}}{A} \right)_{\text{volts}} \quad (\text{H-9})$$

The Quadrature Correction Divisor is used to compensate for the $1/\omega$ factor introduced when the input signal is phase shifted. Given the Quadrature Output Component and the Quadrature Correction Divisor, the true quadrature component, B_1^c , is computed.

$$(B_1^c)_{\text{rad/sec}} = \frac{1}{10A} \frac{\text{Quadrature Output Component}}{\text{Quadrature Correction Divisor}} \quad (\text{H-10})$$

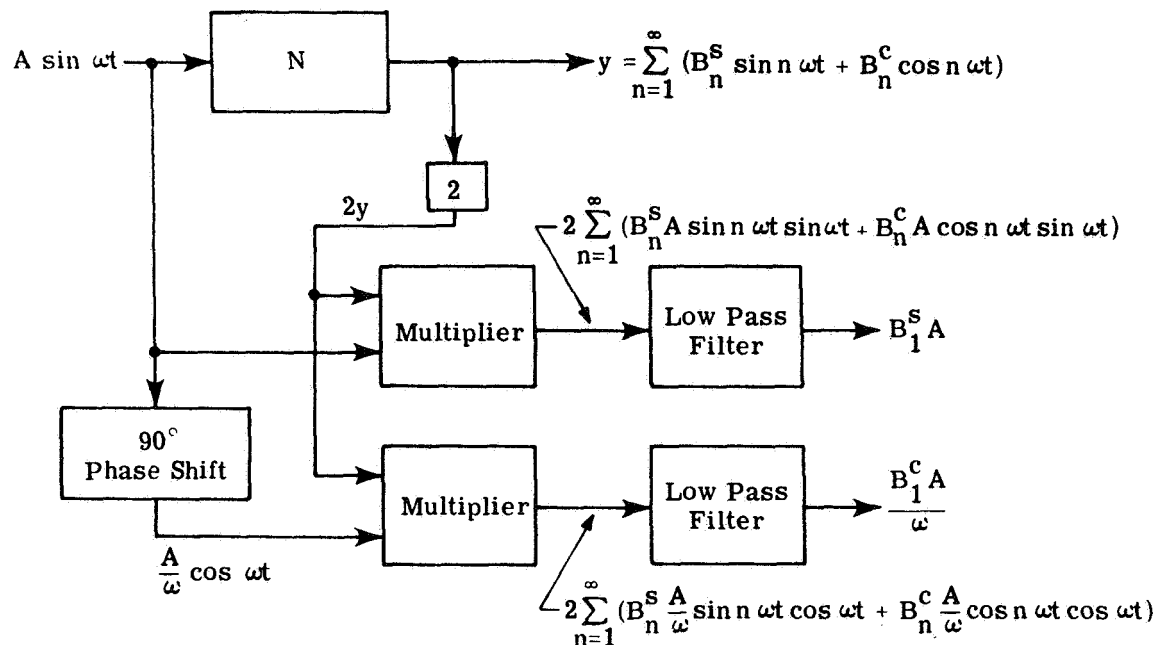


Figure H. 1-1 Conceptual Operation of the Fourier Analyzer

The mechanization is designed to prevent a constant input to the gyro from causing a ramp into the Quadrature multiplier.

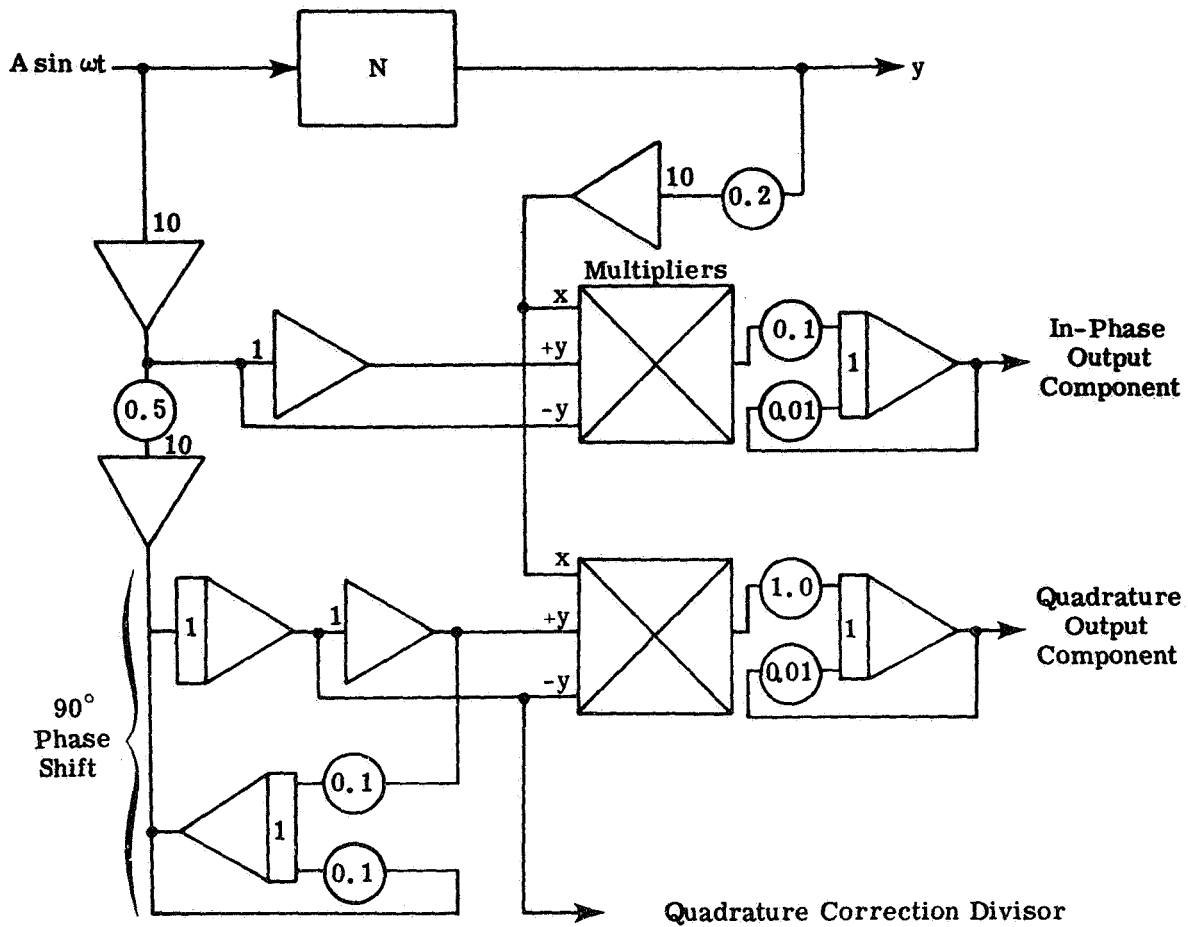


Figure H. 2-1 Analog Computer Mechanization of the Fourier Analyzer

The low pass filters used to attenuate high frequency terms from the two multiplier outputs have a bandwidth of 0.01 rad/sec. Consequently, the rise time of the filters in response to constant inputs is five minutes (three time constants). Care must be exercised to wait the required time period before observing the In-Phase and Quadrature Output Components.

APPENDIX I

DERIVATION OF TRANSFER FUNCTIONS REPRESENTING ROTOR-TO-GIMBAL COMPLIANCE EFFECTS

The use of a second order differential equation to describe the dynamic relation between float angle and applied torque in a single-degree-of-freedom gyro permits simple calculation of limit cycle and frequency response characteristics. The effects considered in such a dynamic model of the gyro float are only those of lumped rotor and gimbal inertia and linear fluid damping. It is now desired to investigate the effects of angular compliance between the rotor and gimbal. Angular flexure can generate sizable error torques about the float output axis by coupling with the spin angular momentum. Consequently, the potential exists for significant modification of the transfer functions used in determining gyro limit cycles and closed loop frequency response.

Figure I-1 illustrates the effects essential for considering rotor-to-gimbal compliance. The rotor is connected to the gimbal along the gyro input (IA) and output (OA) axes by structural members with stiffness k_1 and k_2 respectively. Structural damping is also assumed for motion about the axes. Angular rotations of the rotor and gimbal with respect to an inertially fixed reference frame are represented as A_r and A_g with the appropriate subscript to show axis of rotation.

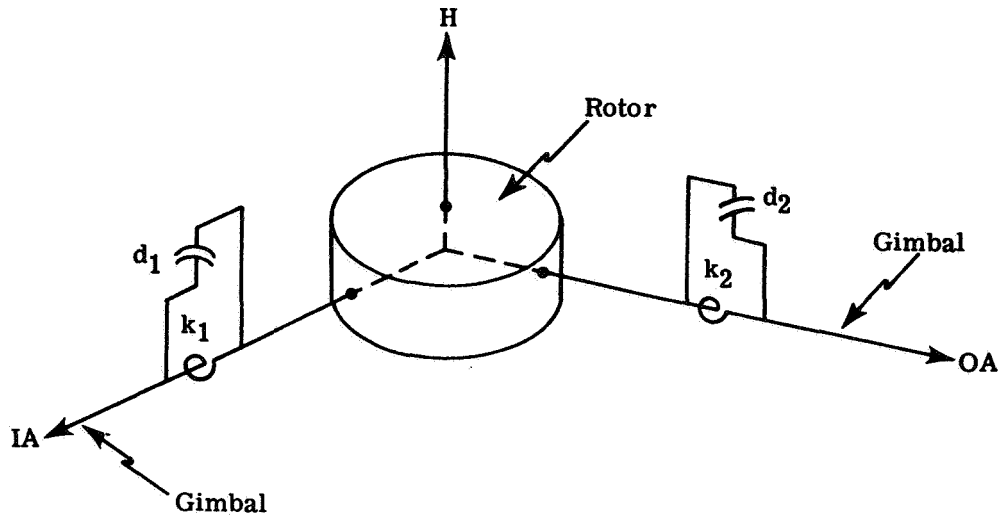


Figure I-1 Rotor-to-Gimbal Compliance

Summing moments on the rotor about the gyro input axis:

$$I_{ii_r} \ddot{A}_{r_i} = -k_1 (A_{r_i} - A_{g_i}) + H \dot{A}_{r_o} - d_1 (\dot{A}_{r_i} - \dot{A}_{g_i}) \quad (I-1)$$

Summing moments about the gyro output axis:

$$I_{oo_r} \ddot{A}_{r_o} = -k_2 (A_{r_o} - A_{g_o}) - H \dot{A}_{r_i} - d_2 (\dot{A}_{r_o} - \dot{A}_{g_o}) \quad (I-2)$$

Assuming that the gyro case and gimbal form an essentially rigid structure about the gyro input axis, A_{g_i} can be represented in Laplace Transform notation as the integral of the angular rate of the gyro about its input axis,

ω_i :

$$A_{g_i} = \frac{\omega_i}{s} \quad (I-3)$$

Similarly, A_{g_0} can be represented in terms of the angular rate about the output axis and the angle between the gyro case and gimbal, α_0 :

$$A_{g_0} = \frac{\omega_0}{s} + \alpha_0 \quad (I-4)$$

Assuming equal rotor inertias and stiffness and damping coefficients about the input and output axes, Eqs. (I-1) and (I-2) can be written in terms of the Laplace Transform operator, s , as a vector-matrix equation:

$$\begin{bmatrix} I_r s^2 + ds + k & -Hs \\ Hs & I_r s^2 + ds + k \end{bmatrix} \begin{bmatrix} A_{r_i} \\ A_{r_o} \end{bmatrix} = \begin{bmatrix} \omega_i \left(\frac{k}{s} + d \right) \\ A_{g_0} (k + ds) \end{bmatrix} \quad (I-5)$$

The rotor exerts a moment on the gimbal about the latter's output axis according to

$$\text{Rotor moment on gimbal} = k(A_{r_o} - A_{g_0}) + d(\dot{A}_{r_o} - \dot{A}_{g_0})$$

Using Eq. (I-5):

$$\begin{aligned} \text{Rotor moment on gimbal} &= \frac{-H(k^2 + 2kds + d^2 s^2)}{(s^2 I_r + ds + k)^2 + H^2 s^2} \omega_i \\ &+ \frac{s^2 (k + ds)(s^2 I_r^2 + sdI_r + kI_r + H^2)}{(s^2 I_r + ds + k)^2 + H^2 s^2} A_{g_0} \end{aligned} \quad (I-6)$$

For limit cycle and closed loop response analyses the variable A_{g_0} is represented by its component α_0 . A signal flow diagram showing the compliance effects as expressed by Eq. (I-6) is given in Fig. I-2. The block marked "Float Dynamics" is the transfer function between the net torque impressed on the gimbal and the gimbal angle, α_0 .

$$\text{Float Dynamics} = \frac{1/C}{s(s\tau_f + 1)}$$

where $\tau_f = I_{00g}/C$. It should be noted that this differs from the definition of τ_f usually used. When the gyro is modeled by simple dynamics, the rotor and gimbal are considered to be rigidly attached and the time constant is computed using the combined moment of inertia of the two components. When compliance is considered, the gimbal and rotor are treated separately and the gimbal dynamics depend only on I_{00g} , the output axis inertia of the gimbal alone.

Define:

$$\begin{aligned} \omega_g &\triangleq \frac{H}{I_r} \\ \nu_n^2 &\triangleq \frac{k}{I_r} \\ \rho &\triangleq \frac{d}{2\sqrt{kI_r}} \end{aligned} \quad (\text{I-7})$$

where ν_n and ρ are the natural frequency and damping ratio, respectively, of the damped second order system assumed about each axis in Fig. I-1. The block diagram of Fig. I-2 can now be reduced to a more compact form, shown in Fig. I-3. The transfer function of the float dynamics, α_0/M_{net} , is given by:

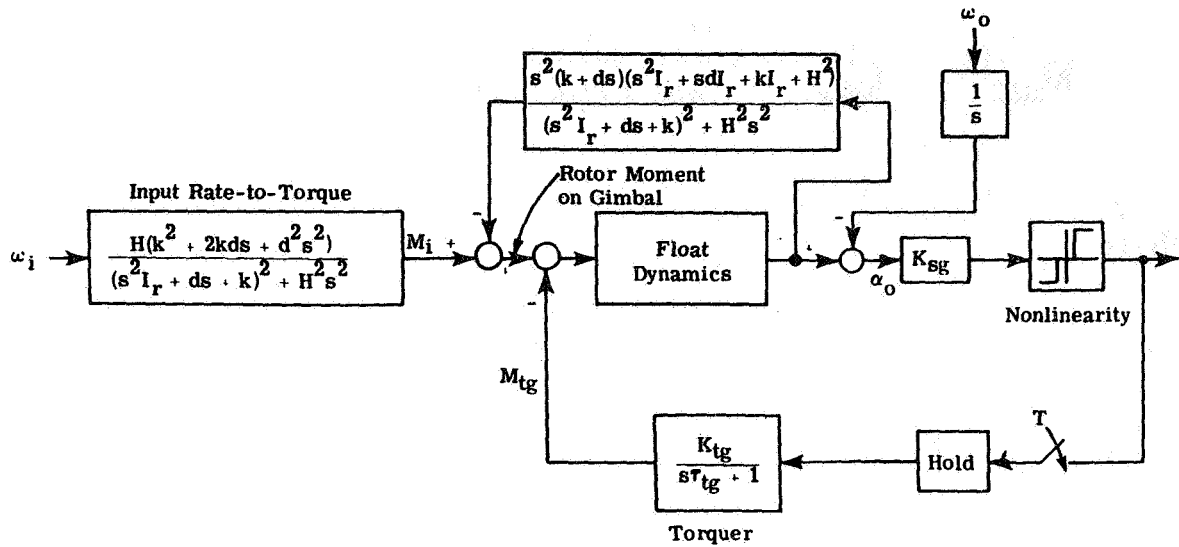


Figure I-2 Signal Flow Diagram of Gyro Loop Including Compliance Effects

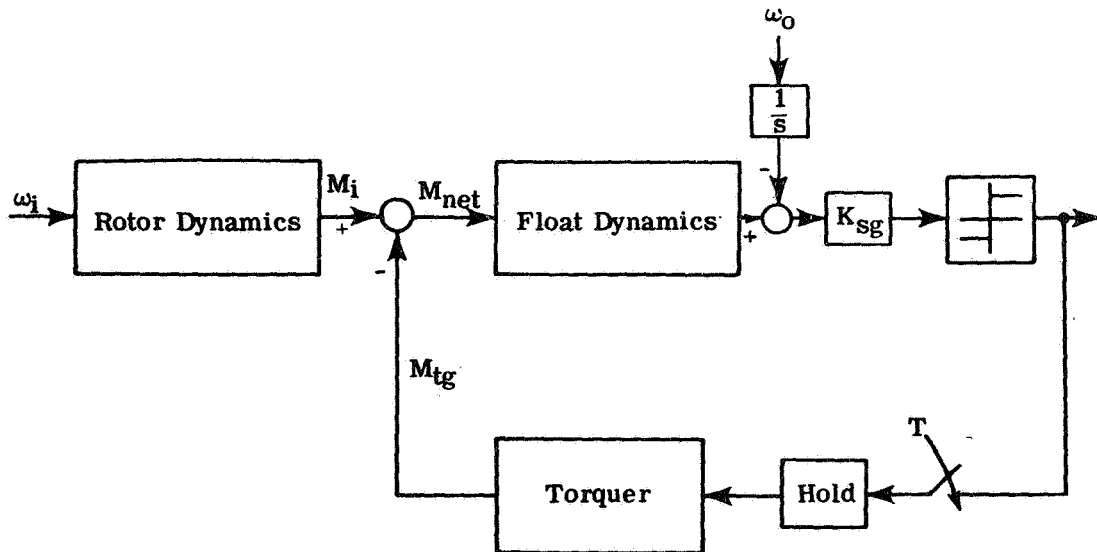


Figure I-3 Signal Flow Diagram Including Compliance Effects (Compact Form)

$$\frac{\alpha_o}{M_{\text{net}}}(s) = \frac{1}{I_{oo_g}} \frac{s^4 + 4\rho\nu_n s^3 + [2\nu_n^2(2\rho^2 + 1) + \omega_g^2]s^2 + 4\rho\nu_n^3 s + \nu_n^4}{s(s^5 + C_4 s^4 + C_3 s^3 + C_2 s^2 + C_1 + C_0)} \quad (\text{I-8})$$

where

$$C_4 \triangleq 4\rho\nu_n + (d/I_{oo_g}) + (1/\tau_f)$$

$$C_3 \triangleq 2\nu_n^2(2\rho^2 + 1) + \omega_g^2 + (4\rho\nu_n/\tau_f) + (k/I_{oo_g}) + (2\rho\nu_n d/I_{oo_g})$$

$$C_2 \triangleq 4\rho\nu_n^3 + (\omega_g^2/\tau_f) + 2\nu_n^2(2\rho^2 + 1)/\tau_f + (2\rho\nu_n k/I_{oo_g}) + (d/I_{oo_g})(\nu_n^2 + \omega_g^2)$$

$$C_1 \triangleq \nu_n^4 + (4\rho\nu_n^3/\tau_f) + (k/I_{oo_g})(\omega_g^2 + \nu_n^2)$$

$$C_0 \triangleq (\nu_n^4/\tau_f)$$

The transfer function which relates the input angular rate, ω_i , to the moment exerted on the gimbal by the rotor, M_i , is

$$\frac{M_i}{\omega_i}(s) = \frac{-H(4\rho^2\nu_n^2 s^2 + 4\rho\nu_n^3 s + \nu_n^4)}{s^4 + 4\rho\nu_n s^3 + [2\nu_n^2(1 + 2\rho^2) + \omega_g^2]s^2 + 4\rho\nu_n^3 s + \nu_n^4} \quad (\text{I-9})$$

APPENDIX J

RECOVERING ANGULAR RATE INFORMATION FROM THE OUTPUTS OF PULSE TORQUED GYROS

The presence of a strapdown inertial navigator in a vehicle suggests that the same body-fixed instruments be used to provide motion indications for an autopilot.* Of particular interest is the vehicle angular rate resolved into body axes. Unfortunately, accurate strapdown gyros usually provide information in the form of incremental angular rotation about the sensor input axis and some data processing is necessary to recover an indication of angular rates. This Appendix outlines several such techniques.

J.1 ASSUMPTION OF PIECEWISE CONSTANT ANGULAR RATES

If the body axis angular rates are varying slowly compared to the output frequency of the gyros, a simple scheme for recovering angular rate information may suffice. This involves collecting gyro output pulses over a given time period and dividing the net indicated angular rotation of the sensor by the interval during which the pulses are collected. The estimate of angular rate about the gyro input axis, $\hat{\omega}_i$, is given by

*In addition to the desire for body axis angular rate information for use in a vehicle autopilot, some accuracy advantage may be gained if angular rate information is available for direction cosine matrix calculations. However, this consideration is beyond the scope of the present report.

$$\hat{\omega}_i = \frac{r\Delta\theta}{sT} \quad (\text{J.1-1})$$

where $\Delta\theta$ and T are the gyro output pulse weight and clock frequency and r and s are integer numbers. The product $r\Delta\theta$ is the angular increment measured during the period sT . In choosing the interval for calculating $\hat{\omega}_i$, the product sT should be small enough to permit the approximation of the input angular rate as a constant.

Errors in the estimate of $\hat{\omega}_i$ of Eq. (J.1-1) arise from time-varying input angular rates and from quantization of the gyro output. The quantization error in the angular increment $r\Delta\theta$ can be viewed as a random variable uniformly distributed over the range $(-\Delta\theta/2, \Delta\theta/2)$ with a mean square value of $\Delta\theta^2/12$. The mean square error in $\hat{\omega}_i$ is:

$$\text{Mean Square Error in } \hat{\omega}_i = \frac{1}{12} \left(\frac{\Delta\theta}{\tau}\right)^2 ; \quad \tau \triangleq sT \quad (\text{J.1-2})$$

Equation (J.1-2) illustrates some factors in the accurate estimation of angular rate from the output of pulse torqued gyros. Consistent with the assumption that ω_i is constant, the interval sT should be made as large as possible. Also, finer gyro quantization gives smaller errors in $\hat{\omega}_i$. Depending on the particular vehicle environment and autopilot this scheme may be perfectly acceptable.

Gain and phase relations for this rate recovery technique based on a linear gyro model and the assumption that $s \gg 1$, are derived in Ref. 8. The gain relation, expressed as a function of normalized frequency is illustrated in Fig. J.1-1. The phase lag is simply $-2\pi \omega/\omega_s$, where ω_s is the frequency at which new values of angular rate are computed: $\omega_s = 2\pi/sT$. From Fig. J.1-1 it can be seen that this approach to angular rate recovery is satisfactory when new angular rate estimates are calculated

at a frequency which is an order of magnitude higher than that of the signal being recovered. If a limit cycle of known frequency, ω_l , is present in the gyro output, proper adjustment of the frequency ω_s will remove this unwanted oscillation from the angular rate estimate. For example, if $\omega_s = \omega_l$ no angular rate will be indicated as a consequence of the gyro limit cycle after the first calculation is performed. If it is necessary to compute angular rate information at a higher frequency to measure troublesome vehicle oscillations, some of the limit cycle will be evident and further filtering of the angular rate signal may be required.

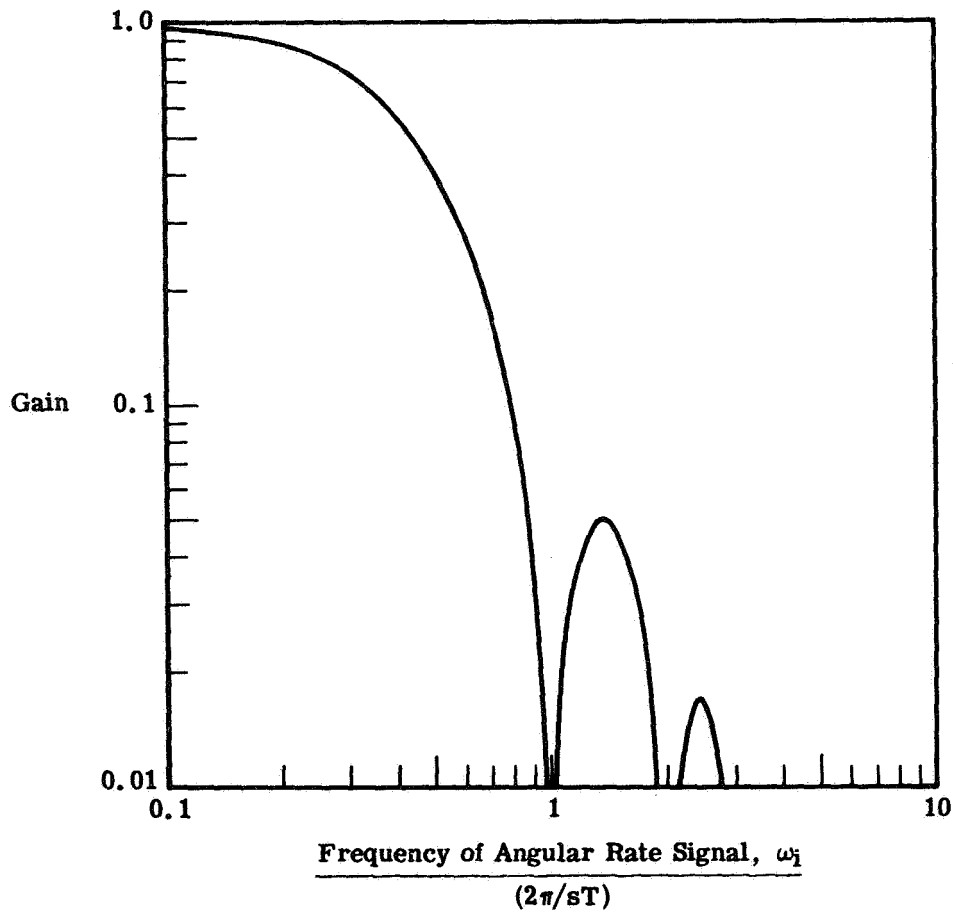


Figure J. 1-1

Gain Characteristics for Integrating Gyro and Rate Recovery Techniques Expressed in Eq. (J.1-1). Source: Ref. 8.

J.2 ASSUMPTION OF PIECEWISE CONSTANT ANGULAR ACCELERATION

If the errors produced in the technique discussed in Section J. 1 are unsatisfactory, angular rate information can be made more sophisticated by including the possibility of angular acceleration. In this case the derivative of ω_1 is assumed to be piecewise constant. Over any interval τ the gyro output, $r\Delta\theta$ is assumed to describe an angular rotation generated according to:

$$r\Delta\theta(t) = \int_0^t \omega_1(t) dt = a_1 t + a_2 t^2 \quad (\text{J.2-1})$$

and the coefficients a_1 and a_2 are to be recovered from the gyro outputs. Two consecutive measurements of angular rotation, $r_{n-1}\Delta\theta$ and $r_n\Delta\theta$, are required to estimate angular rate at $t = n\tau$. The coefficients a_1 and a_2 are assumed constant over the time interval of length 2τ . Using the equations:

$$r_{n-1}\Delta\theta = \int_{(n-2)\tau}^{(n-1)\tau} \omega_1(t) dt = \tau \hat{a}_1 + \tau^2 \hat{a}_2 \quad (\text{J.2-2})$$

$$(r_{n-1} + r_n)\Delta\theta = \int_{(n-2)\tau}^{n\tau} \omega_1(t) dt = 2\tau \hat{a}_1 + 4\tau^2 \hat{a}_2$$

estimates of a_1 and a_2 at $t = (n-2)\tau$ are found:

$$\hat{a}_1 = \frac{\Delta\theta}{2\tau} (3r_{n-1} - r_n) \quad (\text{J.2-3})$$

$$\hat{a}_2 = \frac{\Delta\theta}{2\tau^2} (r_n - r_{n-1})$$

The estimate of body angular rate about the gyro input axis at time $n\tau$ is the derivative of the right side of Eq. (J.2-1) evaluated at $t = 2\tau$:

$$\begin{aligned}\hat{\omega}_i(n\tau) &= \hat{a}_1 + 4\tau \hat{a}_2 \\ &= \frac{\Delta\theta}{2\tau} (3r_n - r_{n-1})\end{aligned}\quad (\text{J.2-4})$$

Using arguments similar to those applied in Section J.1 and assuming that errors in the gyro output angles indicated for consecutive periods of duration τ are not correlated, the error in the estimate of ω_i caused by gyro output quantization has a mean square value given by

$$\begin{array}{l} \text{Mean Square Error in } \hat{\omega}_i \\ \text{Caused by Quantization} \end{array} = \frac{5}{2} \frac{1}{12} \left(\frac{\Delta\theta}{\tau}\right)^2 \quad (\text{J.2-5})$$

Comparison of Eq. (J.2-5) with Eq. (J.1-2) indicates that for both approaches, the errors in $\hat{\omega}_i$ have similar relative dependence on the output observation interval τ and the gyro output quantum $\Delta\theta$. The absolute sensitivity of the more complex scheme under discussion here is larger but this fact should be balanced against the anticipation of smaller errors from incomplete description of the angular rate history.

The accuracy involved in assuming the angular rate model implied by Eq. (J.2-1) can be determined by expressing ω_i as a polynomial with any desired number of terms. For example:

$$\omega_i(t) \triangleq b_0 + b_1t + b_2t^2 \quad \dots \quad (\text{J.2-6})$$

The output of a perfect gyro over an interval τ would then be

$$\begin{aligned}
\Psi_{n-1} &= \int_{(n-2)\tau}^{(n-1)\tau} \omega_i(t) dt \\
&= b_0\tau + \frac{b_1}{2}\tau^2 + \frac{b_2}{3}\tau^3 + \dots
\end{aligned}
\tag{J.2-7}$$

$$\begin{aligned}
\Psi_n &= \int_{(n-2)\tau}^{n\tau} \omega_i(t) dt \\
&= 2b_0\tau + 2b_1\tau^2 + \frac{8}{3}b_2\tau^3 + \dots
\end{aligned}$$

Substituting Ψ_{n-1} for $r_{n-1} \Delta\theta$ and Ψ_n for $(r_{n-1} + r_n) \Delta\theta$ in Eq. (J.2-4) yields the estimate

$$\hat{\omega}_i(n\tau) = b_0 + 2b_1\tau + \frac{10}{3}b_2\tau^2 + \dots
\tag{J.2-8}$$

The error in $\hat{\omega}_i$ using the technique discussed in this section is the difference between Eqs. (J.2-8) and (J.2-6):

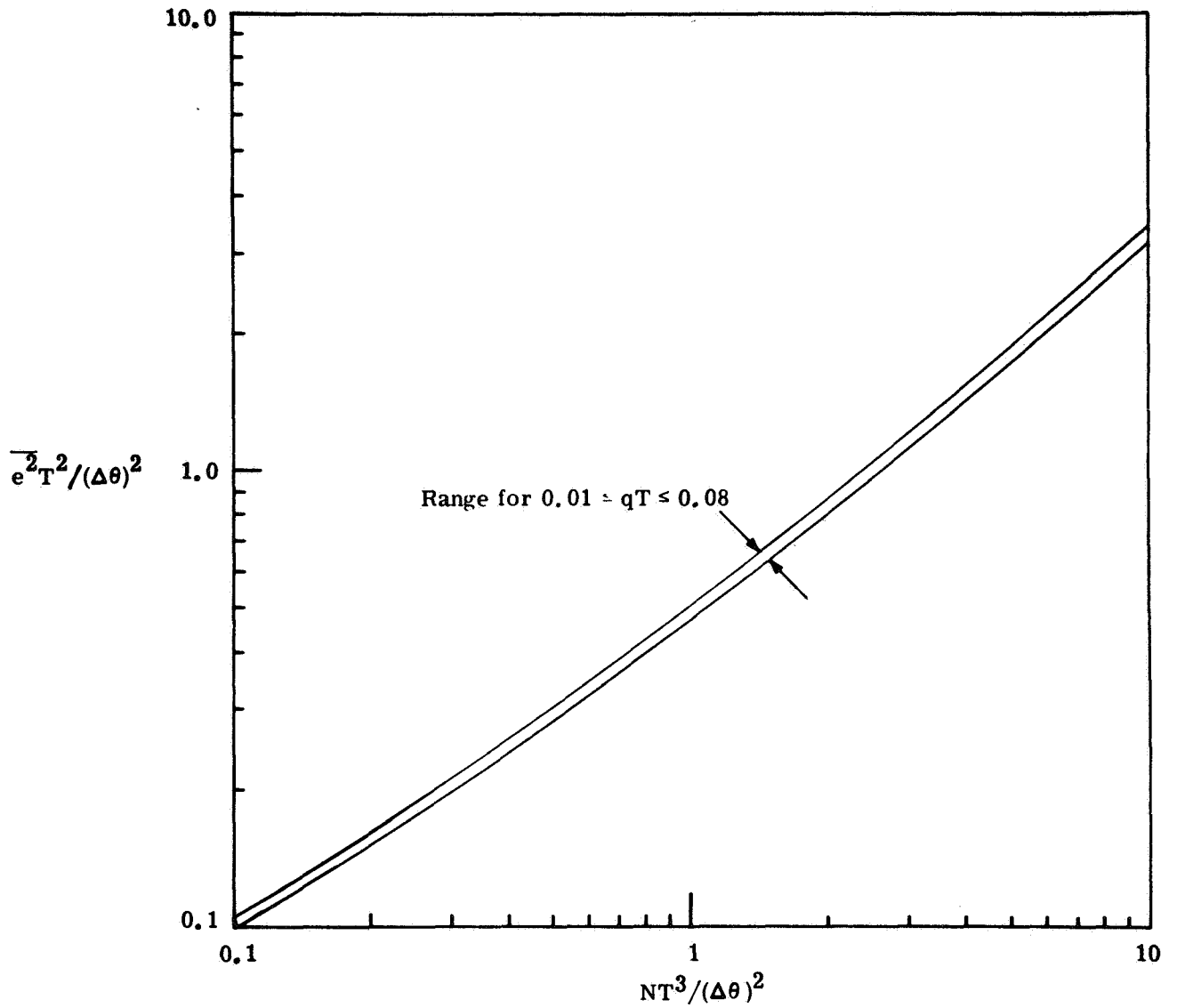
$$\begin{aligned}
e &= \hat{\omega}_i(n\tau) - \omega_i(n\tau) \\
&= b_0 + 2b_1\tau + \frac{10}{3}b_2\tau^2 + \dots \\
&\quad - [b_0 + 2b_1\tau + 4b_2\tau^2 + \dots] \\
&= -\frac{2}{3}b_2\tau^2 + \text{higher order terms in } \tau
\end{aligned}
\tag{J.2-9}$$

The errors caused by incomplete specification of the nature of ω_i are proportional to the second and higher power of τ , as would be expected from the fact that second and higher derivatives of input angular rate are ignored in this formulation. Of course, higher order polynomial representations of ω_i can be used or the polynomial can be fitted to more data points. For example, see Ref. 5.

J.3 OPTIMAL FILTERING

Optimal linear filtering can be used to recover angular rate information from the outputs of pulse rebalanced integrating gyros. Some work has been performed at TASC in this area but has not been documented. The discussion below summarizes that effort and presents some indications of the accuracy which can be obtained.

In order to apply linear filter theory to the problem of recovering angular rates, motion about the gyro input axes is described as a random variable. In particular, angular rate is modeled as an exponentially correlated quantity. The gyro is assumed to provide a quantized representation of the integral of the random angular rate. Since the measurement to be processed by the filter is quantized, recent developments in the design of optimal linear filters (Ref. 6) are employed to account for this aspect of the problem. Based on the analytic determination of steady-state errors in the estimate of angular rate, the normalized relations illustrated in Fig. J.3-1 were obtained. Caution should be exercised in using these curves. The relations illustrated are based on the assumption that process noise acts on the system in a way that causes the conditional errors in estimates of the state variables to have a Gaussian distribution immediately prior to each measurement. This requirement depends on the magnitude of the process noise, the angular rate correlation period and the time between new inputs to the filter.



- $\overline{e^2}$ = Steady state mean square error in $\hat{\omega}_i$
- N = Covariance of the process noise driving the linear first order system whose output represents vehicle angular rate
- q = Correlation time of vehicle angular rate

Figure J.3-1 Angular Rate Estimation Errors: Optimal Linear Filter for Quantized Measurements

REFERENCES

1. Gelb, Arthur, and Sutherland, Arthur A., Jr., Design of Strapdown Gyroscopes for a Dynamic Environment, Interim Scientific Report, The Analytic Sciences Corp., TR-101-2, 15 January 1968.
2. Gelb, Arthur, and Sutherland, Arthur A., Jr., Design of Strapdown Gyroscopes for a Dynamic Environment, Semi-Annual Report, The Analytic Sciences Corp., TR-101-1, 7 July 1967.
3. Gelb, Arthur, and VanderVelde, Wallace E., Multiple-Input Describing Functions and Nonlinear System Design, McGraw-Hill Book Co., Inc., August 1968.
4. Farrell, James L., Performance of Strapdown Inertial Attitude Reference Systems, AIAA Journal of Spacecraft, Vol. 3, No. 9, September 1966, pp. 1340-1347.
5. Koenke, E.J., and Downing, D.R., Evaluating Strapdown Algorithms: A Unified Approach, MDC TR 68-76, Vol. I, Proceedings of the Fourth Inertial Guidance Test Symposium, Holloman Air Force Base, 6-8 November 1968.
6. Curry, Renwicke E., Jr., Estimation and Control with Quantized Measurements, Ph.D. Thesis, M.I.T. Department of Aeronautics and Astronautics, May 1968.
7. Weinstock, H., Effects of Linear Vibration on Gyroscope Instruments, M.I.T. Department of Aeronautics and Astronautics, Notes from Summer 1963, Program 16.39S.
8. Granley, G.B., and Paulson, D.C., Rate Derivation from a Pulse Rebalanced Gyro, Honeywell, Inc., Memo dated 1 November 1967.

NATIONAL AERONAUTICS AND SPACE ADMINISTRATION
WASHINGTON, D. C. 20546
OFFICIAL BUSINESS

FIRST CLASS MAIL



POSTAGE AND FEES PAID
NATIONAL AERONAUTICS AND
SPACE ADMINISTRATION

POSTMASTER: If Undeliverable (Section 158
Postal Manual) Do Not Return

"The aeronautical and space activities of the United States shall be conducted so as to contribute . . . to the expansion of human knowledge of phenomena in the atmosphere and space. The Administration shall provide for the widest practicable and appropriate dissemination of information concerning its activities and the results thereof."

— NATIONAL AERONAUTICS AND SPACE ACT OF 1958

NASA SCIENTIFIC AND TECHNICAL PUBLICATIONS

TECHNICAL REPORTS: Scientific and technical information considered important, complete, and a lasting contribution to existing knowledge.

TECHNICAL NOTES: Information less broad in scope but nevertheless of importance as a contribution to existing knowledge.

TECHNICAL MEMORANDUMS: Information receiving limited distribution because of preliminary data, security classification, or other reasons.

CONTRACTOR REPORTS: Scientific and technical information generated under a NASA contract or grant and considered an important contribution to existing knowledge.

TECHNICAL TRANSLATIONS: Information published in a foreign language considered to merit NASA distribution in English.

SPECIAL PUBLICATIONS: Information derived from or of value to NASA activities. Publications include conference proceedings, monographs, data compilations, handbooks, sourcebooks, and special bibliographies.

TECHNOLOGY UTILIZATION PUBLICATIONS: Information on technology used by NASA that may be of particular interest in commercial and other non-aerospace applications. Publications include Tech Briefs, Technology Utilization Reports and Notes, and Technology Surveys.

Details on the availability of these publications may be obtained from:

SCIENTIFIC AND TECHNICAL INFORMATION DIVISION
NATIONAL AERONAUTICS AND SPACE ADMINISTRATION
Washington, D.C. 20546